2019

Convergence in a Disk Stacking Model on the Cylinder

Christophe Golé
Smith College, cgole@smith.edu

Stéphane Douady
Laboratoire Matière et Systèmes Complexes

Convergence in a disk stacking model on the cylinder*

Christophe Golé† and Stéphane Douady ‡

February 5, 2020

Contents

*Published in Physica D, https://doi.org/10.1016/j.physd.2019.132278 ©2019.

†Corresponding author. cgole@smith.edu, Mathematics and Statistics Department, Smith College, Northampton, MA 01063, USA - Partially supported by NSF grant # 0540740

‡Laboratoire Matière et Systèmes Complexes, CNRS, France

Abstract

We study an iterative process modelling growth of phyllotactic patterns, wherein disks are added one by one on the surface of a cylinder, on top of an existing set of disks, as low as possible and without overlap. Numerical simulations show that the steady states of the system are spatially periodic, lattices-like structures called *rhombic tilings*. We present a rigorous analysis of the dynamics of all configurations starting with closed chains of 3 tangent, non-overlapping disks encircling the cylinder. We show that all these configurations indeed converge to rhombic tilings. Surprisingly, we show that convergence can occur in either finitely or infinitely many iterations. The infinite-time convergence is explained by a conserved quantity.

Keywords: Disk packing, phyllotaxis, rhombic tiling, attractor, dynamical system.
Declaration of interest: None.

1 Introduction

The study of packing of identical elements on the surface of a cylinder originated almost two hundred years ago in phyllotaxis, where packing processes model the morphogenesis of arrangements of plant organs around the stem. The most commonly described arrangements are cylindrical lattices made of two intersecting families of helical rows of elements (called parastichies). The numbers of rows in these families are most often successive Fibonacci numbers [3, 10, 11, 16, 22, 27, 33].

More recently, the lattice arrangements introduced in phyllotaxis have seen applications beyond plant biology. Levitov [17] showed that, theoretically, repulsive vortexes in a type II superconductor lead to minimal energy lattices with Fibonacci phyllotaxis. The spirals of phyllotaxis were reproduced in an experiment using repulsive drops of ferrofluid [37] or with "magnetic cactii" [4].

Regular arrangements that do not necessarily follow the Fibonacci sequence have been studied by Erickson [9], who pointed out examples in microbiology. Carbon nanotubes are non-biological examples of regular tubular lattices [24]. Models of sphere packing have been used for these structures [1, 21], although again they were introduced in 1872 to give an evolutionary explanation to phyllotaxis [13].

In most of the literature cited above, the structures of reference are cylindrical lattices. They appear either as descriptive models [16], minimum of a certain energy [17], minimum of packing density [10], or as stable fixed points of a dynamical system with more or less "soft" interactions between stacked elements [18, 23, 30]. Interesting exceptions to this focus on lattices occur, among others, in [5] where transitions between lattices due to physical deformation of the cylinder are studied in terms of dislocations. Line slip structures, where a part of a cylindrical lattice is translated along a parastichy, appear in the densest packings of spheres for certain parameter values [21]. Structures with line slips, do occur in our setting (see Figure 28) but are just examples of a larger set of lattice-like structures, called *rhombic tilings* [22, 28], which are central to the present paper. When the vertices of a cylindrical lattice are ordered by height, the angle between a vertex and the next one - the angle of divergence in phyllotaxis - is constant and close to the Golden Angle ($\approx 137.51^o$) in Fibonacci phyllotaxis [16, 23, 27]. On the other hand, in rhombic tilings the divergence angle, as well as the vertical displacement, are periodic, but usually not constant. Some data suggests that these patterns may better describe phyllotactic structures [22, 28].

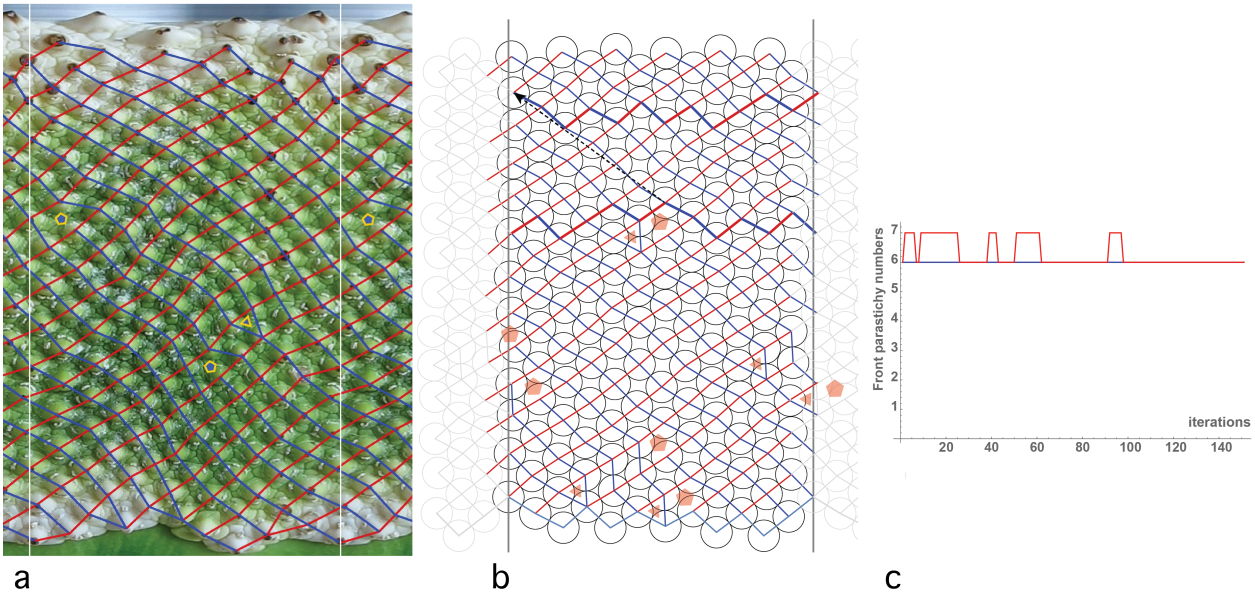

Figure 1: **a.** Digitally unrolled spadix of peace lily (*Spathyphyllum*), showing a phyllotactic structure obtained by joining the center of each organ to those of its contact neighbors. The (broken) blue and red lines that trace these contacts are called parastichies, that form helices around the spadix. The two white lines in the picture correspond to the same line on the spadix. The pattern is transitioning from 7 up (blue) and 6 down (red) parastichies, to (6, 6). This can be monitored locally via the zigzagging fronts: each pentagon decreases a parastichy number by 1, each triangle increases one by 1. This pattern appears to converge in finite time to a rhombic tiling, where no triangles or pentagon appears any more. Note that this is not a Fibonacci pattern but what we called Quasi-Symmetric in [12]. **b.** A similar pattern, starting as (6,6) and ending as (6, 6), simulated, with more complicated transitions, by stacking 150 disks over the original bottom (6, 6) front. This pattern ends up, after a last pentagon, back in a (6, 6) rhombic tiling, with fronts repeating with periodicity vector shown by the black dashed arrow. **c.** The graph showing the fronts parastichy numbers and their convergence to (6, 6).

In 1868, Schwendener [33] introduced the first dynamical model of phyllotaxis morphogenesis. It is based on Hofmeister's observation that a plant organ forms at the edge of the meristem (microscopic tip of a plant stem) at a place where the existing organs have left enough space [34]. Schwendener modeled nascent organs as disks, placed iteratively on the surface of a cylinder, on top of an existing set of disks, as low as possible and without overlap. (Note that the threshold condition subsumed in the expression "enough space" is translated to the geometric condition of "as low as possible".) While this model produces, as steady states, the cylindrical lattice structures described in the classical phyllotaxis literature, it also exhibits the aforementioned rhombic tilings, which are periodic steady states that look like crooked cylindrical lattices (see Figures 1c and 2. For more on rhombic tilings, see [22, 28]).

We conjecture that a subset of the rhombic tilings forms the attractor for this model. In other words, the stacking model *always* converges toward periodic rhombic tilings, a surprising fact given the apparent geometric rigidity of the model. As a first, significant step, we prove here this conjecture for patterns whose initial conditions consists of chains of 3 tangent disks: *any* configuration produced by the system on such chains converges to some rhombic tiling. We achieve this by providing a complete analysis of the dynamics of the system with these initial conditions. Note that chain of 3 tangent disks give rise most immediately to patterns of parastichy numbers (1, 2) or (2, 1), which are the first non symmetric state in Fibonacci phyllotaxis stemming from monocot plants.

We also show, by examples and numerical simulations that the same geometric mechanism that yields convergence in our simple case also occurs in patterns with more complicated initial conditions.

Striking to us was the fact that the disk stacking model exhibits *two kinds of convergence* to rhombic tilings: the patterns may be pre-periodic and become rhombic tilings in finite time, or they can do so asymptotically, in infinite time.

Our rigorous dynamical analysis on the set of 3-chains shows that this is indeed the case even with simple initial conditions. And it unveils a mechanisms of convergence that seems to apply to the general case. Connecting the centers of the tangent disks in a configuration, one obtains a graph (the ontogenetic graph, see [32] and Figure 2). The process of convergence on the space of 3-chains always involve recurring pairs of pentagons and triangles in the faces of the graph (see Figures 1b and 2B). Moreover, in the case of infinite convergence, these configurations of triangles and pentagons give rise to a geometric quantity that is conserved along the orbit, as the shape of the successive pentagons flattens to a pair of rhombus and triangle (Figure 3 A, A', A". See also Figure 9 for evidence in a case of larger initial chains).

Understanding the nature of the attractor for the disk stacking model has practical implications in phyllotaxis. Rhombic tilings, while regular enough looking, can be a better descriptor for botanical patterns than lattices, and account for permutations of the vertical order of elements, as was shown on a Birch catkin in [22, 28]. Careful measurements in *Arabidopsis thaliana* have also shown that the divergence angle may switch from the Golden Angle to multiples of it. This can also be simply explained by permutations of the vertical order of the elements [31,38]. The last authors have proposed a stochastic model to account for this phenomenon [26]. But the stacking models, which are deterministic, also generates these permutations [12, 22, 31].

Moreover, when the disk size is allowed to diminish slowly, the stacking model provides a concise and intuitive geometric explanation for the overwhelming occurrence of Fibonacci phyllotaxis. [12][1] Maybe more surprisingly, for faster decrease rates of the disks' size, the system most often generates what we've called *quasi-symmetric* phyllotaxis, where the number of parastichies are close together *i.e.* of the form $(m, m+k), k \ll m$ (see Fig. 1). This type of pattern, exhibited by a number of plants (e.g. corn, strawberries, or peace lily) has somehow never been mentioned explicitly in the three-century-old literature on phyllotaxis [12, 28]. In the language of dynamical systems, these phenomena can be interpreted in terms of orbits falling into basins of attraction of different components of the attractor. This is the tack taken in [18, 23] in a simpler system, where the attractor, composed of rhombic *lattices* is part of the so-called van Iterson diagram. In this viewpoint, identifying the attractor and its topology as it varies with disk size is a central question, one that we start addressing here. And while this work sets the stage for this big topological picture, it also provides dynamical and geometric tools that work on the local level, spelling out the conditions for different pattern transitions to occur. Both should be useful in a rigorous study of the Fibonacci transitions in the disk stacking model.

While phyllotaxis has fascinated scientists of all kinds since the 18^{th} century, it was not until the turn of the 21^{st} century that, thanks to the use of fluorescent markers and microscopy, the biological mechanism of phyllotaxis pattern formation started to be understood. In the prevalent biological model [6, 14], the main actors are the plant hormone auxin and the auxin efflux transporter PIN, both of which interact in a process called polarized auxin transport. Primordia (nascent organs) form where there is sufficient auxin concentration. In a positive feedback loop, the PIN protein facilitates auxin's transport toward cells with greater auxin concentration and in turn, auxin concentration attracts PIN to these cells' walls. This mechanism leads to increase auxin concentration at the site of a nascent primordium, but also to a depletion of auxin in its neighborhood. In other words the next primordium will not be located near this new one. Geometrically, the new primordium is "taking space", that can't be occupied by the next primordia. And by the uniformity of the process, that space is of roughly uniform size. Hence this biological mechanism, with short range activation and longer range inhibition can be seen as a validation of Hofmeister's hypothesis.

This mechanism is also consistent with Turing's model of Phyllotaxis [20] who, long before this biological mechanisms was uncovered, had hypothesized an abstract chemical system of reaction-diffusion

[1] This explanation has roots in van Iterson [11].

with a kind of coupled short-range activation and long-range inhibition, where the uniform distribution of some (hypothetical) morphogen is an unstable equilibrium. This principle, and the type of PDE's that he used to model it became the basis for his and later models of morphogenesis in general [2, 20].

Many of the computer era models of phyllotaxis are more or less explicitly based on Hofmeister's hypothesis [18, 23, 29–32]. Other, PDE-based models, are in a more direct lineage with Turing's, and display the short range activation and long range inhibition conferring instability of constant solutions [15]. A recent paper in that vein takes a mechanistic approach, incorporating the known biochemical and mechanical factors known to biologists [19] in its choice of equations. Other, large ODE models seek to reproduce the transport mechanisms at the cellular level [7, 14, 25].

While each of these model brings new insight, they all display short-range activation and longer-range inhibition, and thus express in one way or another Hofmeister's hypothesis. The disk stacking model has the advantage of simplicity and of directly addressing the geometric constraints implied by Hofmeister. Moreover its simulation is by orders of magnitude faster than the ODE or PDE models: we have run loops involving thousands of simulations, each involving hundreds of iterations within minutes. This allows an effective exploration of the entire phase space in some cases (see e.g. Figure 3) that helped structure the rigorous classification of the dynamics. In [12], a sweep of 2500 simulations through a parameter plane uncovered the duality of Fibonacci vs Quasi-symmetric phyllotaxis.

Goal and plan of this article Again, the main goal of this paper is to provide a complete mathematical analysis of the disk stacking process on cylindrical chains of 3 disks. This provides in particular a first rigorous step (see Theorem 1) towards proving that all (admissible) configurations yield rhombic tilings in finite or infinite time under the stacking process.

After this introduction, we start by the self-contained Section 2 that summarizes our findings as well as the main ideas behind our analysis, in a language that we hope strikes a balance between intuition and sufficient precision. As a motivation, we start by presenting outputs of our numerical simulations, with an overview of the space of initial conditions and the different types of dynamics it supports. The section ends with a presentation of numerical evidence of a similar convergence mechanism to rhombic tilings for more general initial conditions, leading more credence to our conjecture.

Section 3 goes through geometric definitions used in our analysis of the dynamics. Section 4 zooms in on properties of notches, the elementary segments of chains of tangent disks whose geometry determines the types of transitions that patterns go through (rhombic, triangle or pentagon). Section 5 gives a parametrization of the phase space C_3 of 3-chains. In Section 6, we begin the classification of the dynamics of configurations starting on C_3, concentrating on periodic or pre-periodic regions, while Section 7 deals with the non periodic dynamics of asymptotic convergence. Section 8 contains concluding remarks and it is followed by appendices where some of the more technical results are proven.

Acknowledgements. The authors would like to thank Pau Atela, Jacques Dumais and Christophe Godin for useful conversations. Scott Hotton started the study of the topology and symmetries of disk chains, and we have borrowed some of his terminology, descriptions, and illustrations of the space C_3 of 3-chains, for which we are grateful. Finally, we are grateful to Rebecca Benhardt who, while a Smith College student, came across the special kind of rhombic tilings that we named after her.

2 Convergence: simulations and results

In this section we introduce the phenomenology of convergence of the disk stacking process. We also sketch the proofs involved in the classification of its dynamics.

2.1 Informal introduction to the geometric concepts.

A rigorous approach to the concepts and their properties are presented in Section 3.1.

Geometry of disk stacking The disk stacking process consists in placing disks one by one on the surface of the cylinder, in the lowest place possible without overlap with previously placed disks. Assuming that the initial configuration, not necessarily a result of the dynamical process itself, is dense enough so that disks can't "fall through the cracks", each new disk must then rest tangentially on two lower disks. We will make this density condition precise and call it admissibility. The disk stacking process can be seen as a map $\mathcal{S}$ (sometimes multivalued) from an admissible configuration to another one.

We say that the new disk is the *child* of the disks that it is tangent to, one on the left and one on the right, which we call its *parents*. Occasionally a disk has 3 parents. As the stacking proceeds, the pattern forms a graph, called *ontogenetic graph* [32] whose vertices are the centers of the disks, and the edges connect parents and children (see Figure 1b & c). Orienting the edges from left to right, they become vectors that either point up or down, and we call them accordingly *up* or *down* vectors of the chain (see Figures 2 A).

Chains and their parastichy numbers After a few iterations (*e.g.* 5 iterations in Figures 2 A and B), the top of the pattern becomes a *prone*, *cylindrical chain* of disks enclosing the cylinder. A chain of disks is just a finite sequences of disks, each one tangent to the previous one. The chain is prone if it's oriented so that the vector connecting the centers of a disk to the next one is pointing to the right, *i.e.* is an up or down vector. The chain is cylindrical if goes once around the cylinder before closing back on its initial disk. In Figure 2A, the sequence of disks 10:7:9:16:14 is not a chain since 16 is not tangent to 9. The sequence 10:7:4:6:9:11:8:10, while a cylindrical chain, is not prone. The sequences 10:7:4:6:8:10 and 10:7:9:6:8:10 form prone cylindrical chains. The latter has the distinction of being a *front*, *i.e.* a prone cylindrical chain of disks such that the next disk piled on it, (11 here) is higher than any disk of the front. In the first example, the next disk to be piled on it, 9, is lower than 10, so that chain is not a front.

The number of down vectors, and number of up vectors of a prone cylindrical chain of disks are called its *parastichy numbers* [12, 22, 32].

In Figure 2A, *all* the prone cylindrical chains have the same parastichy numbers (number of downs, number of ups) = (2, 3) as the original chain 5:2:4:1:3:5. This is due to the fact that faces formed by the ontogenetic graph are all rhombic: the addition of a new disk only transposes a pair of up and down vectors, with no net change in their numbers. Note also that, *with a swap of colors*, these numbers correspond to the numbers of (undulating) parastichies of the pattern. Indeed there are 2 green parastichies (1:3:7:9… and 2:4:6:8…) and 3 red ones (1:4:7…, 2:5:8… and 3:6:9…). This correspondence arises from the fact that a red parastichy contains the tip of exactly one green vector of the (prone, cylindrical) chain. This innocuous property contains the power of the concept of chain or front parastichy numbers: it generalizes the classical concept of parastichy numbers, in that it coincides with it when parastichies are clear in a disk piling pattern but it is also defined when the pattern does not have clear parastichies. It is more local and computable than the classical concept, and thus eminently suited for transition analysis.

To start seeing the usefulness of chain parastichy numbers, consider the front 11.9.10.7.8.11 in Figure 2 B. The child Disk 12 of the front and its parents 7 and 8, which are themselves tangent, form a triangle, yielding a net increase of one down vector (namely $\overrightarrow{(12)8}$) in the new front 11.9.10.7.12.8.11. Likewise, the pentagon 7:12:14:13:10:7 decreases the number of down vectors by one.[2] In [12, 28] we show, as the radius of the disks is progressively decreased, how fronts, with orderly triangle transitions, act as "Fibonacci-adding machines" explaining the widespread occurrence of Fibonacci parastichy numbers in plants. Likewise, orderly pentagon transitions can explain the transitions of decreasing Fibonacci parastichy numbers in sunflower or artichoke heads.

In Figure 2A, the chain 5:2:4:1:3:5 is also a *front*: the new disk stacked at the lowest place, *i.e.* 6 in this case, is higher than all the disks in the front. This remains true of the successive chains formed after that by adding the new disk, and removing the disk(s) between its parents. And this also holds for Figure 2B. In plants, one should think of a front as the chain of primordia which, at a given time, form

[2] Crystallographers call these " +1 or -1 dislocations".

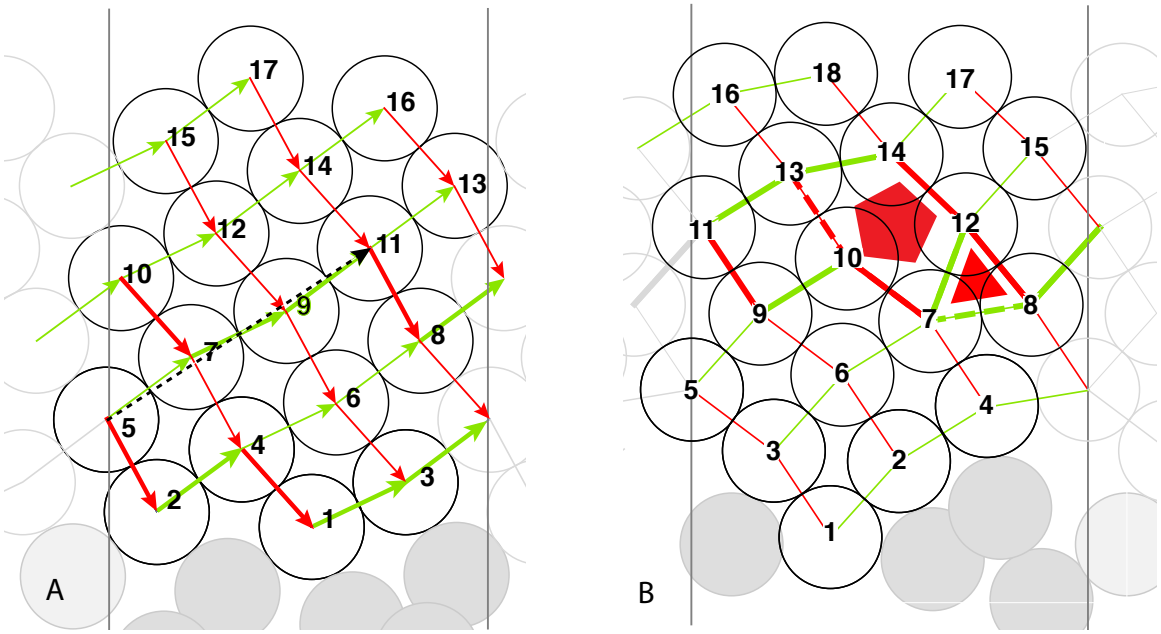

Figure 2: **Disk stacking process.** **A.** The cylinder is shown unrolled, with a configuration of disks obtained by stacking on the original configuration of gray disks. The two vertical lines represent the same "meridian" line on the cylinder. Disks are stacked in the lowest place available, resulting in the order shown by the numbers. In this case. The edges connecting tangent disks form the ontogenetic graph, with green up vectors and red down-vectors (we only show their orientation in this picture). The faces of the graph are all rhombi, and thus the stacking is a rhombic tiling. As shown by the black arrow, Front 11.8.10.7.9 is just a translation of Front 5.2.4.1.3. All fronts have parastichy numbers (3, 2). **B.** The tiling produced by the ontogenetic graph includes not only rhombi but a triangle and a pentagon, which break the translation symmetry. The triangle transition adds a red (down) vector, and the pentagon removes one. As a result the front parastichy numbers switch from (3, 2) to (3, 3) (at Disk 12) and back to (3, 2) (at Disk 14).

the boundary of the morphogenetic region at the growing tip of the plant.

We sometime denote a front or a chain by its highest element, which indicates the time at which it was the highest chain. For instance 5.2.4.1.3.5 is the *front at 5*.

Rhombic tilings and the convergence conjecture. The configuration in Figure 2A is periodic: the front at 10:7:9:11:8:10 is a translation of the front 5:2:4:1:3:5 by the vector (black, dashed arrow) joining the centers of Disks 5 and 11. It is not a coincidence that 6, the period, is the product 3×2 of the parastichy numbers common to all fronts in this configuration: the pattern returns to the same exact front shape when all the transpositions in the 6 possible pairs of the 3 up and 2 down vectors in rhombic transitions have occurred. Since its ontogenetic graph will forever have rhombic faces, we call this pattern a *rhombic tiling* [12, 22]. Similarly to the example, all the fronts in a general rhombic tiling have the same parastichy numbers, and any rhombic tiling of parastichy numbers $(Ndown, Nup)$ is a periodic orbit of period $Ndown \cdot Nup$ for the stacking process. Sometime, when some of the down (or up) vectors are equal, the period will *divide* $Ndown \cdot Nup$. The classical example is the case of a rhombic *lattice*, where all up vectors are equal, and all the down vectors are equal: such a configuration, if obtained by stacking, is a fixed point of the system. This is proven in [22], Proposition 6.4.

In our many numerical experiments, we have observed that, for random admissible initial conditions, the configuration converges toward a rhombic tilling. This can happen in finite time (*i.e.* within a finite number of iterations the pattern becomes periodic), as in Figure 2A, or in infinite time, with the distance to a rhombic tilling decreasing asymptotically to zero (Figure 3A). This observation leads to the

conjecture:

Conjecture 1. *Under the disk stacking process $\mathcal{S}$, any admissible configurations yields chains of rhombic tilings after finitely many iterations or tends to one in infinitely many iterations.*

In other words, this conjecture says that the global attractor of the system is a subset of the set of rhombic tilings.[3] The bulk of this paper is devoted to a complete analysis of the dynamics of the stacking process on the space C_3 of initial configurations that are fronts of parastichy numbers (1, 2) or (2, 1). That analysis will show that Conjecture 1 indeed holds in this case:

Theorem 1. *When starting with cylindrical chains of parastichy numbers (1, 2) or (2, 1), all chains obtained in the stacking process either become chains of rhombic tilings after a finite number of iterations, or tend to such chains in infinitely many iterations.*

In the rest of this section, we present numerical simulations that provide a schematic picture of all the different types of dynamics and convergence, and where they occur in C_3. We then sketch the proof of Theorem 1. We also present observations and heuristic arguments (Section 2.4) that show that this mechanism is at play for configurations with chains of arbitrary parastichy numbers, evidence that Conjecture 1 should also hold for longer initial chains, or arbitrary (admissible) initial conditions.

2.2 Dynamics on the chains of length 3: computer simulations

As mentioned above, our proof of Theorem 1, which occupies Sections 3-7, consists of an entire classification of the dynamics of $\mathcal{S}$ on the space C_3 of chains of length 3. We present here this classification via numerical simulations, illustrating in particular the different modes of convergence.

Chains of length 3, *i.e.* chains of parastichy numbers either (1, 2) or (2, 1) can be parametrized by the angles $\beta_1, \beta_2, \beta_3$ their successive vectors make with the horizontal. Since the chain starts and ends at the same point, we must have $\sin(\beta_1) + \sin(\beta_2) + \sin(\beta_3) = 0$. This is the equation of a surface in 3-space. Non-overlap conditions further constrain 3-chains to a subset of this surface, that constitutes the space C_3. We will show that the projection of C_3 onto its tangent space at $(0, 0, 0)$, *i.e.* the plane $\beta_1 + \beta_2 + \beta_3 = 0$, is a hexagon (Section 5). The inverse of the projection on this hexagon provides a parametrization of C_3.

Numerically, we detected exactly four types of dynamics for patterns starting in C_3. These four types partition the hexagonal parameter space into a "Star of David" with a rosace inside (see Figure 3R). Outside the star, all the patterns propagate immediately as rhombic tilings (deep blue); in the red petals of the rosace, patterns seem to converge asymptotically to rhombic tilings, via an infinite sequence of triangles and pentagons, with the pentagons progressively closing up; In the region outside the petals, in lighter red on up to blue, the patterns become rhombic tiling in finite time, with only finitely many triangles and pentagons. Finally, the six triangular rays of the "Star of David" are colored in purple because, due to triple tangencies (where a child disk has three parents), they afford two possible interpretations: either as (2, 2) - rhombic tilings (blue) or patterns with infinite time convergence, oscillating periodically between chains of parastichy numbers (2, 1) and (2, 2) . We call these patterns Benhart tilings after Rebecca Benhart, the Smith College student who first discovered them. It was surprising (to us) that Benhart tilings form a full 2-dimensional subset of the parameter space: at first sight, the condition of triple tangency that characterizes them seems non-generic, and intuitively should reduce the dimension of this subset to 0 or 1.

Of course, the existence of the infinite convergence case can only be ascertained by a proof, which was the initial motivation behind this paper.

[3] The attractor does not include *all* rhombic tilings: it is possible to find rhombic tilings that can't be obtained by stacking, *e.g.* rhombic lattices whose two sets of parastichies wind up the cylinder in the same direction.

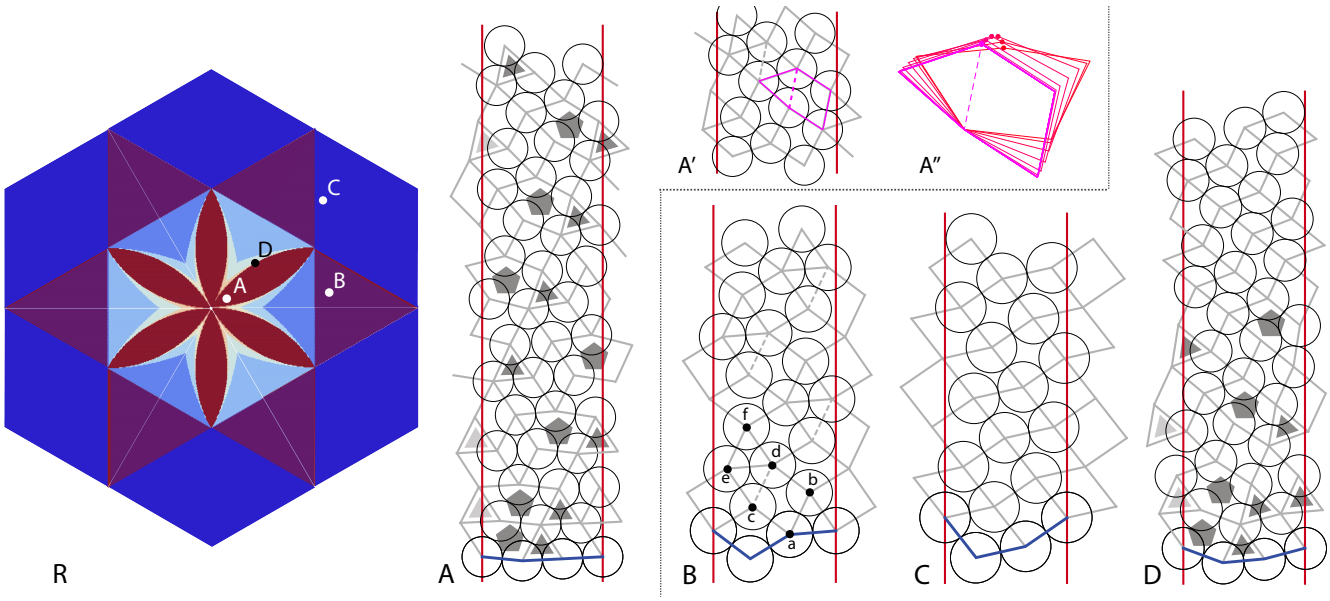

Figure 3: **The different dynamics of fronts of C_3. R.** Fronts of C_3 are parametrized by a hexagonal region H_3 of the plane $\beta_1+\beta_2+\beta_3=0$, where β_k is the angle that the k^{th} vector of the chain makes with the horizontal. Fronts were iterated 200 times, the top index of the last pentagon was recorded, and used to color the corresponding points with index 0 (in darker blue), 100 and above (in darker red) and the spectrum (orange and lighter blue) in between. We marked 4 points corresponding to fronts whose dynamics appears in the figures of same labels. **A (Infinite convergence)**: Pairs of pentagons and triangles seem to occur indefinitely. However, the pentagons, after opening up, tend toward closed pentagons, as seen in **A"**, where we translated the pentagons to the same base point, and indicated the dynamics from red (early iterations) to pink (late). Because of pentagons closing up, the limiting pattern (see **A'**, after 287 iterates) can be interpreted as a (2, 3)-rhombic tiling. See Theorem 2 and Figure 28. **B. (Benhart Tiling).** Because of their recurrent triple tangencies, these periodic patterns can either be interpreted as (2, 2)-rhombic tilings or as patterns with closed pentagons, taking infinite time to converge (hence the purple color of the 6 triangular regions they occupy). Since the disks at d and c are tangent, the 6 points marked can either be grouped into the pentagon $\{a,b,c,d,e\}$ and triangle $\{d,e,f\}$ or as the two rhombi $\{a,b,c,d\}$ and $\{c,d,e,f\}$ **C (Rhombic tiling).** All points outside the Star of David (deep blue in Figure R) correspond to either (1, 2) or (2, 1) rhombic tilings. **D (Finite convergence).** Pentagons and triangles disappear after 21 iterations of $\mathcal{S}$ in this example, at which point the pattern turns into a (2, 2)-rhombic tiling.

Packing density along orbits To connect our work to the extensive literature on packing density - and the question as to whether Fibonacci phyllotaxis optimizes packing, and thus could be prefered by evolution, we did some numerical experiment on how packing changes along the orbits of the stacking process. The packing density of a configuration of disks is the proportion of the area occupied by the disks in a given area of the cylinder. Lagrange (regular case, 1773) and Thue (general case, 1890) proved that the densest possible packing of disks of equal radius in the plane (and hence in the cylinder, when possible) is the triangular packing, where each disk has 6 tangent neighbors. This tiling has density $(\pi\sqrt{3})/6 \approx 0.9069$ ([35]). Work by Bergeron and Reutenauer [10] shows that, in some very precise sense[4], the density of cylindrical lattices is asymptotically maximized when the divergence angle of the lattice is the Golden angle or any angle with same asymptotic continued fraction expansion (noble angles). The minimal density for a regular lattice is obtained for a square lattice, of density $\pi/4 \approx 0.7854$.

Since the packing varies along an orbit in our case, we computed the density in bands of height 1 on the cylinder, repeating this at each point of the orbit. We also calculated the average of these densities over the asymptotic period of each orbit, again at each point of the orbit.

Clearly, because each orbit converges to a rhombic tiling, the average density becomes constant, asymptotically (Figure 4 A) or in finite time (B, C, D). Interestingly, even though the dynamical process of disk accretion is, at each iteration, optimizing the packing density, the density may increase and

[4]They work with the notion of "growth capacity" which is $\pi/4$ times the packing density.

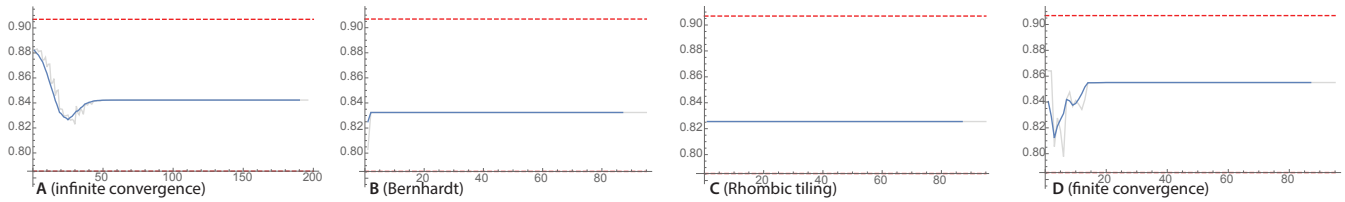

Figure 4: **Density plots along orbits.** The density plots over bands of height 1 (gray), averaged over the asymptotic period (blue) of the orbits of the chains A, B, C, and D of Figure 3. The red dotted lines indicate the minimum and maximum disk packing density of $\pi/4$ and $\pi\sqrt{3}/6$. All configurations reach a plateau: the density of Configuration A does so asymptotically, the others in finite time. And all end up increasing to the plateau, in the last phase of convergence - unless they already are on the plateau, when the starting chain is already that of a rhombic tiling, as for Chain C.

decrease along an orbit. This is most notable for some orbits that converge in infinite time such as for chain A, where the packing density may first dip down, as the pentagons open up, before going back up again, as the pentagons close up. What seems to be true however is that the closing of the pentagons always yields an increase of density. Hence, before stabilizing on a constant period-averaged density, that density increases.

The rest of the paper, starting on Section 3.1 will concentrate on proving that the dynamics are indeed as described above. This will prove in particular that all patterns starting with chains in C_3 do converge in either finite or infinite time to a rhombic tiling.

2.3 Sketch of the proofs involved in the classification

We now present the broad outline of the proofs behind the classification of the dynamics of the stacking process. These proofs occur in Sections 4-7, after Section 3, where we give rigorous definitions and establish basic properties of the stacking process. As we said earlier, we conceptualize the stacking process as a map $\mathcal{S}$ on the space of configurations of disks on the cylinder and, for now, we use chains of C_3 as initial conditions.

To determine the offspring of a chain, *i.e.* the new disk determined by $\mathcal{S}$ applied to that chain, we first analyze the possible offsprings of *notches*. An i, j notch is a sub-chain made of i down vectors followed by j up vectors. In all the cases that we encounter in this paper, the offsprings of a chain is also the offspring of one of it notches. The type of transition the chain undergoes is thus a function of the shape of the notch, as parametrized by its hinge angles, as well as the general orientation of the notch (See Figure 5).

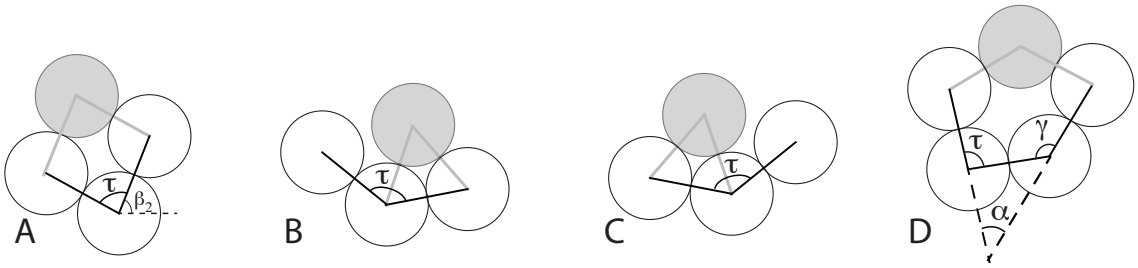

Figure 5: **Notches and their offsprings.** The first 3 examples shown are 1,1-notches. **A.** The hinge angle $\tau < 2\pi/3$: the offspring yields a quadrilateral transition. **B.** The hinge angle $\tau > 2\pi/3$: the offspring undergoes a triangular transition, resting on the up vector since it is less steep than the up vector. **C.** The hinge angle τ is identical to the one in B. But the general orientation of the notch (as given by the angle β_2) now makes the down vector less steep, and the triangle rests on it. **D.** A 1,2-notch with a pentagon transition. The fact that $\alpha \leq \pi/3$ or equivalently $\gamma + \tau \leq 4\pi/3$ is a necessary and sufficient condition for the existence of this transition (Proposition 4.3).

On the 1,1 notches, there is a rhombus transition if the hinge angle τ is in the interval $[\pi/3, 2\pi/3]$,

and a triangle transition if τ is in $[2\pi/3, \pi]$. In the latter case, the triangle rests on the least steep of the two vectors of the notch, insuring the lowest position possible for the offspring. The boundary cases $\tau = \pi/3$ or $2\pi/3$ afford both interpretations as triangle and rhombus transitions. The 1,2 or 2,1 notches present more possibilities: not only do they yield triangle and rhombus transitions, but they can also generate pentagon transitions, see Figure 5D. Section 4 entirely classifies the possible offsprings of 1,2 or 2,1 notches, depending on conditions on the two hinge angles τ, γ of the notch, as well as on the bearing angle β_2, which gives the angular orientation of the notch. Even though the chains we'll encounter in our proofs may have notches of length greater than 3, this classification is enough to examine all the situations that arise in orbits of $\mathcal{S}$ starting in C_3.

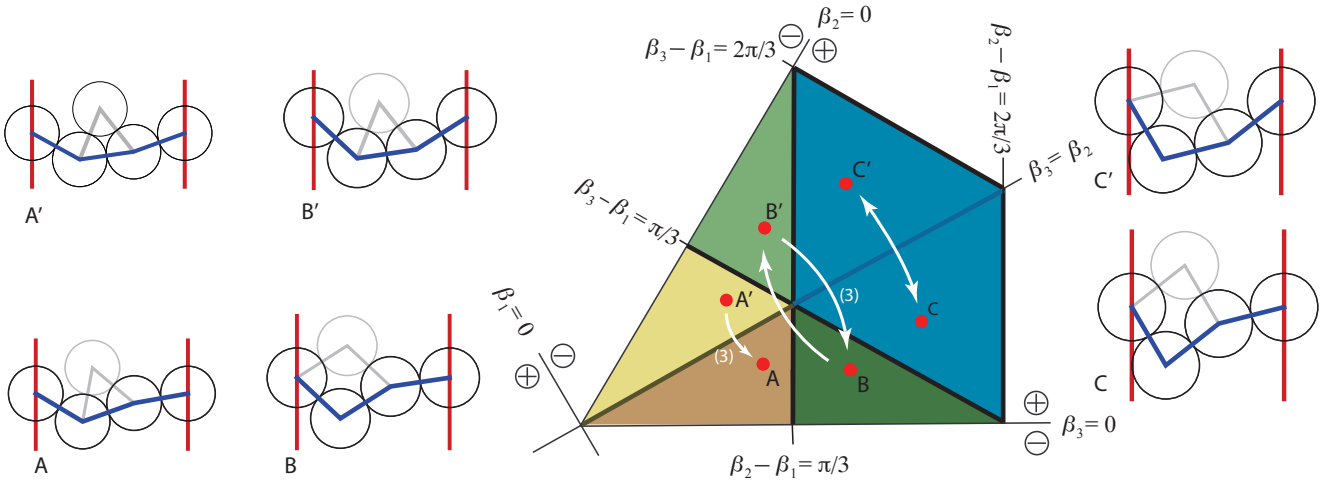

Figure 6: **First iterations on chains in C_3.** The set of all admissible 3-chains, reduced by symmetry to a kite shape parameter region in the plane $\beta_1 + \beta_2 + \beta_3 = 0$. Representative chains from that region (black disks joined by blue segments) are shown with their first iterates (in grey)

We use symmetry to reduce our study to a kite-shaped slice of the parameter space H_3 of C_3, between the planes $\beta_2 = 0$ and $\beta_3 = 0$. The symmetries, *i.e.* geometric transformations that commute with $\mathcal{S}$, consist of the permutations $(\beta_1, \beta_2, \beta_3) \to (\beta_2, \beta_3, \beta_1) \to (\beta_3, \beta_1, \beta_2)$, which can be seen as just choosing a different starting point for the same chain. Another symmetry consists of reflecting the chain about a vertical axis, yielding $(\beta_1, \beta_2, \beta_3) \to (-\beta_3, -\beta_2, -\beta_1)$. Combinations of these two types of symmetry give rise to 6 distinct symmetries, and hence the hexagonal symmetry of the parameter space. (Section 6). Hence studying the stacking process starting on 1/6 of the parameter space - a Kite shape sector - is enough to understand the outcomes of the process on *all* 3-chains in C_3.

Using our knowledge of notch offsprings, we determine the outcome of the first four iterations of $\mathcal{S}$. For this we partition the kite along the lines $\beta_2 = \beta_3$ (long diagonal), $\beta_2 - \beta_1 = \pi/3$ (vertical bisector) and $\beta_3 - \beta_1 = \pi/3$ (diagonal bisector). These lines separate chains according to whether they or their iterates never have triangle offsprings (Region $C \cup C'$), or they have one within the first (Region $A \cup A' \cup B'$) or second iteration (Region B). Chains in Region $C \cup C'$ are chains of 2, 1-rhombic tilings, and $\mathcal{S}$ has the effect, via rhombic transitions, of flipping β_2 and β_3 at each iteration, yielding period 2 orbits. Region $B \cup B'$ is made of Benhart tilings, of period 4. Finally, all the chains from Region A' go to Region A in 3 iterations.

The most complex and surprising dynamics is concentrated in Region A, characterized by the equations $\beta_2 - \beta_1 < \pi/3$, $\beta_3 < \beta_2$ (Section 7).

It turns out that, to establish the dynamics in that region, it is necessary to entirely understand the effect of the 8 first iterations on the initial chain 1:2:3:1 . We do this step by step, showing that the combinatorics of the transitions is the same for all chains in that region, up to Disk 10 (Figure 7): 2 triangles, one pentagon, 3 rhombii, then either a triangle or repeated rhombii. Moreover, we trace the

parents of each new disk. We prove for instance that Disk 7 is always R_{45}, meaning that it undergoes a rhombic transition with parents 4 and 5.

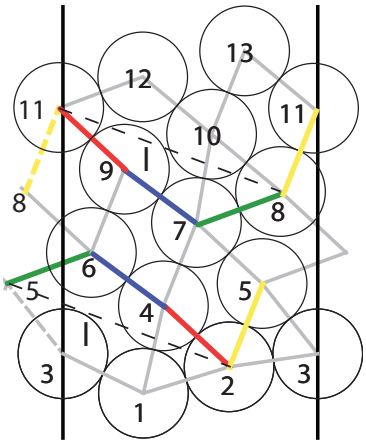

Figure 7: Dynamics in Region A. The conserved quantity I is the length of the dotted segments.

The universality is broken at Disk 10, which can either be R_{98} or, as in Figure 7, the triangular T_{78}. In the latter case, we can show that the geometric conditions on Chain 11.9.7.10.8.11 are similar to those that permitted our analysis starting on Chain 5.3.1.4.2.5, six iterations before. The same combinatorial dynamics thus applies, and repeats every 6 iterations, or until the analog of the angle $\angle 8.7.9$, $6k$ iterations away, becomes small enough to stop giving rise to a triangular transition. We show that, in some cases this occurs for a finite k, in others one needs to let k go to infinity for this angle to go below the threshold $2\pi/3$. The question is then: how to distinguish between these two cases? The key to this answer is represented by the colored vectors in Figure 7.

The vectors of like colors shown in this figure are identical because of rhombic transitions. For instance the green vectors $\overrightarrow{56}$ and $\overrightarrow{78}$ are equal. Because of this, the composite vectors $\overrightarrow{8(11)}$ and $\overrightarrow{25}$ are equal and their norm constitutes *a conserved quantity I* under the sixth iteration $\mathcal{S}^6$ of $\mathcal{S}$, as long as triangles occur.

Because of the colored vectors identities, a rotation by π and a translation of Chain 5.6.4.2 gives Chain 8.7.9.11, with corresponding vectors in reverse order. The shapes of these chains are determined by their hinge angles $\tau = \angle 1.3.5, \gamma = \angle 2.1.3$ and $\tau' = \angle 7.9.11 = \angle 2.4.6, \gamma' = \angle 8.7.9 = \angle 5.6.4$ and they in turn determine the shapes of the chains 5.3.1.4.2.5 and $\mathcal{S}^6(5.3.1.4.2.5) = 11.9.7.10.8$ (see Figure 8a). We show that, in general, on the chains $\{\mathcal{S}^{6k}(5.3.1.4.2.5) : k \in \mathbb{N}\}$, $\mathcal{S}^6$ can be expressed as $\mathcal{S}^6(\tau, \gamma, \alpha) = (\tau', \gamma', \alpha)$, where α, constant along an orbit, is the angle that the yellow vector make with the horizontal. To understand the asymptotic behavior of $\mathcal{S}$, it is therefore enough to understand the map defined by $\phi(\tau, \gamma) = (\tau', \gamma')$.

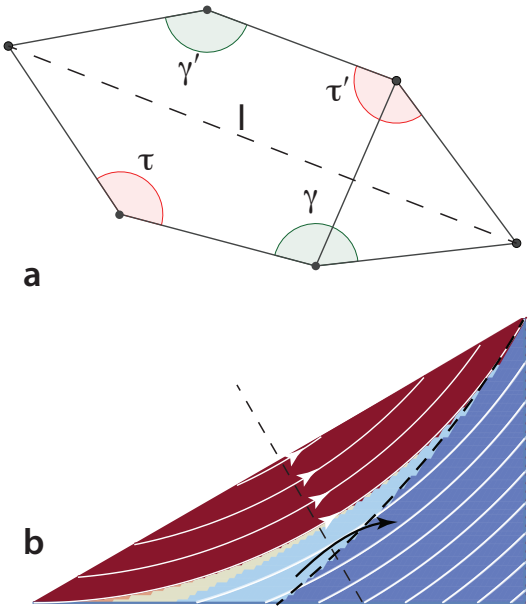

Figure 8: Conserved quantity I and dynamics in A. **a.** Hexagon formed by a pair of triangle-pentagon, with the original hinges angles τ and γ and the transformed angles τ' and γ'. **b.** Isolines of I in Region A, with the resulting dynamics color-coded as in Fig. 3. The lighter blue region is mapped in one iteration of ϕ into the darker blue region, *e.g.* , while preserving the isolines.

With the rotation symmetry pointed to above, the angles that define ϕ appear within the hexagon formed by the triangle and pentagon pairs of the configuration (Figure 8a). Simple geometry shows that $\tau' \geq \tau$ and $\gamma' \leq \gamma$, which explains the change of shape of the pentagon in Figure 3A', as well as the arrows in Figure 8b. Indeed, this and other properties translate into properties of the conserved quantity I, whose isolines can be traced in coordinates of the Region A of C_3 (in white on Fig. 8b).

In this representation, points in the upper boundary (hypotenuse) correspond to $\gamma' = \gamma, \tau' = \tau$, *i.e.* fixed points of ϕ. They also correspond to rhombic tilings: the hexagon of Figure 8a has parallel opposite sides in this case, and thus the middle quadrilateral (joining the vertices with marked angles $\gamma, \gamma', \tau, \tau'$) is a rhombus (see Figure 28 for an example). Isolines of I join the fixed points on the hypotenuse by pairs. A point on such an isoline converges asymptotically, under *infinitely many iterations* of ϕ, to the right hand fixed point of the pair, and to the left hand fixed points under iterations of ϕ^{-1}: its orbit is heteroclinic.

One isoline of I connects the endpoints of the hypotenuse. This curve, and all the isolines above it, correspond to heteroclinic orbits. This region corresponds exactly to the red petal-shaped region of our simulation, confirming that it is indeed the region of infinite convergence to rhombic tilings.

Below that red region, the isolines end up on the vertical right side of region A touching the region B of the Benhart tilings. Points there end up, in a *finite* number of iterations of ϕ, in the darker blue region to the right of the black curve, corresponding to the set where exactly one triangle transition occurs. After that triangle, the configuration is then a rhombic tiling. These orbits thus reach rhombic tiling chains in finite time . This ends the classification of the dynamics of orbits starting on C_3, and the proof that any such orbit converges to a rhombic tiling, with a precise distinction between those that do so in finite and those that do it in finite time.

2.4 Convergence in configurations starting with longer chains.

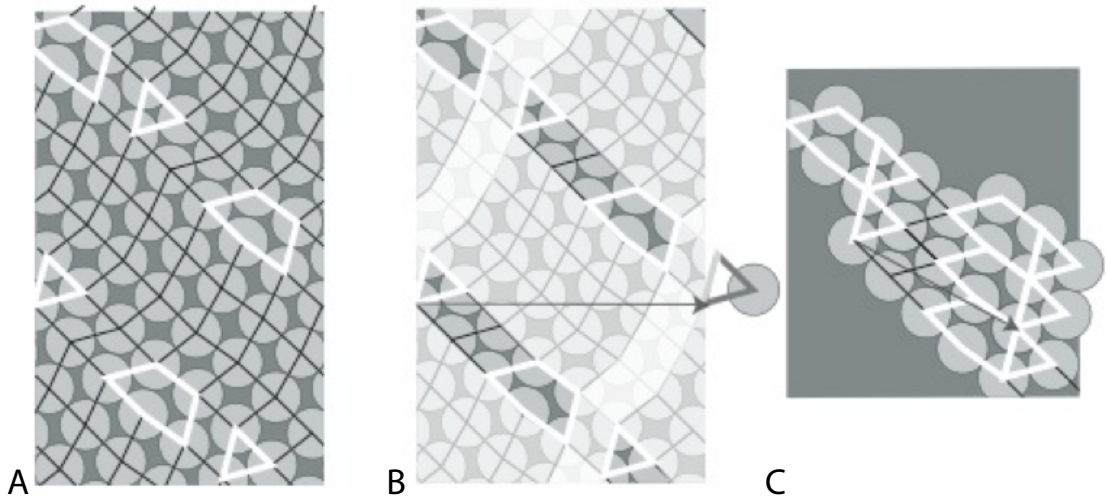

Figure 9: **Convergence in higher dimensions.** **A.** A pattern that goes from (4, 4) to (4, 5) and back to (4, 4) via triangle and pentagon pairs. The latter shrink slowly, indicating convergence. **B & C.** By removing many of the rhombi, we can "factor out" the non essential elements of the dynamics, *i.e.* , rhombi. Doing so reduces the pattern to the dynamics of convergence of smaller chains, pointing to the universality of the mechanism.

From our many simulations with initial conditions of various length, we found the same kind of convergence as with C_3 chains, and the same kind of convergence mechanism at play. Indeed, either we observed rhombic tilings, or sequences of triangle and pentagon pairs arranged along parastichies. There again, we observed the pentagons in these pairs disappear in finite time or shrinking asymptotically - in either cases the patterns converge to rhombic tilings. Figure 9 shows how the dynamics in higher dimensions (longer chains) can in a sense be reduced to lower dimensions (shorter chains). But things can get a little more complicated: we have also observed patterns where two distinct sequences of triangles and pentagons can evolve in parallel. We have also observed cases where an isolated hexagon transition may appear. But, again, all pattern we observed did converge to rhombic tilings, all eventually involving pairs of triangles and pentagons in a row, separated by rhombi.

Systematic iterations on a 2D slice of 5,3-fronts To get a more global view of convergence in the spaces of longer chains, we ran the disk stacking process on fronts from a two dimensional slice of the space of (5, 3)-chains of a given diameter. This space, around a generic point, is 6-dimensional: there are 8 angles defining the vectors of the front, but two of these are determined by the other 6.

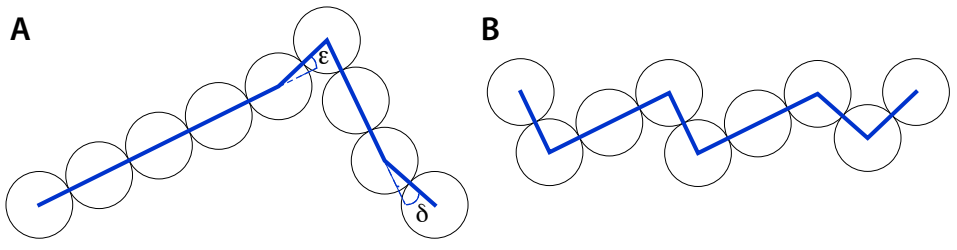

Figure 10: **Witches hats.** A 5,3 witches hat, with $\epsilon = .5$, $\delta = .4$, and its corresponding front.

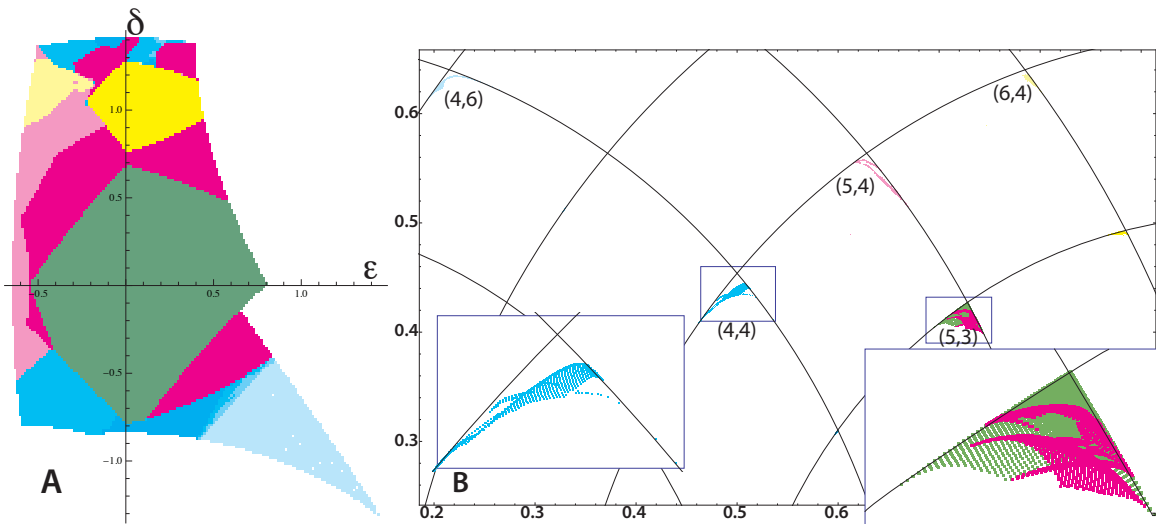

Figure 11: **Convergence in higher dimensions.** **A** The space of "witch hats" fronts as parametrized by ϵ, δ. It is colored according to the parastichy numbers of the final fronts after 100 iterations. Green: (5, 3)-rhombic tilings (the origin represents the (5, 3)- lattice with the given disk diameter), Red: converging to (5, 3)-rhombic tilings, pink: converging to (5,4) rhombic tilings, darker yellow: (6, 3), lighter yellow: (6,4), darker blue: (4,3), medium blue (4, 4), lighter blues: (4,5) and (4,6). **B** The same points, but projected via their sum of up vectors. The (4,3) and (4,5) points are not very visible, but they exist. The set of sum of up vectors of the (4,4) points (left insert) and (5, 3) points (right insert) have been magnified to show the folding occurring in the projection.

We swept through a 2 dimensional slice of this 6 dimensional space (with disk diameter 0.1688), by choosing fronts that are defined by taking all but one of each up and down vectors to be the same. The parameters are the angle ϵ and δ that the exceptional up vector (resp. exceptional down vector) makes with the rest. These are best visualized in the chain obtained by rearranging the vectors of the front, putting all the up vectors first, and then the down vectors looked to us as a "witch hat", hence the name. See Figure 10. Iterating $\mathcal{S}$ on this subset of (5, 3)-fronts, we observed systematic convergence to rhombic tilings, in either finite or infinite time. The irregularity of the witch hat fronts produces convergence to rhombic tilings of many different parastichy number, apart from the original (5, 3): (4, 3), (4, 4), (4, 5), (4, 6), (5, 4), (6, 3), (6, 4). Taking the quotient of the largest over the smallest of each pair yields values usually closer to one than the original 5/3. This is a phenomenon - migration towards quasi-symmetry- that we have studied more extensively in [12].

3 Dynamical and geometric definitions

3.1 Disk stacking process $\mathcal{S}$

As described earlier, the disk stacking process consists of adding disks of constant diameter on the surface of the cylinder in the lowest possible place with no overlap with the existing disks. This process is well defined when the configuration has no holes large enough to let the new disk percolate down indefinitely. When this is the case, it is intuitively clear that the new offspring disk will land tangentially to two parent disks of the configuration and that the parents are on opposite sides of the offspring. We make all these notions more precise in this section.

The cylinder $\mathcal{C}$ We define the cylinder $\mathcal{C}$ to be the plane with identifications: $(x+n, y) \cong (x, y), \forall n \in \mathbb{Z}$, that is $\mathcal{C} = \mathbb{R}/\mathbb{Z} \times \mathbb{R}$. We think of the plane $\mathbb{R}^2$ as an image of the unrolled cylinder. Mathematically, $\mathbb{R}^2$ is homeomorphic to the universal covering space $\tilde{\mathcal{C}}$ of the cylinder $\mathcal{C}$. With this convention, the cylinder has circumference 1.

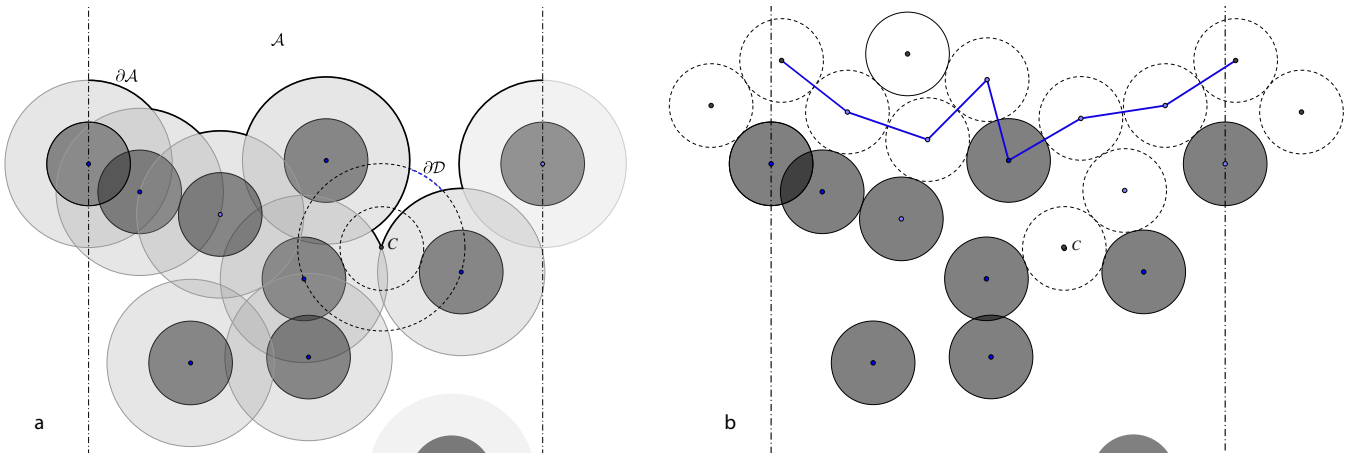

Figure 12: **Disk stacking process. a.** The dark gray disks of diameter b (= .184 here) form an admissible configuration: the corresponding disks of diameter $2b$ (lighter gray) form a bounding curve for the top component $\mathcal{A}$. The offspring disk of the configuration is centered at the minimum C of the bounding curve. The part of the circle $\partial\mathcal{D}$ of radius $2b$ centered at C replaces arcs in the former bounding curve to form the new one. **b.** After the stacking process is iterated 8 times (in this case), it forms a chain of disks, represented here by the blue zigzagging line joining the centers of its disk. As the offspring of this chain is higher than any of its disks the chain is actually a front.

Admissible configurations Given a finite configuration of closed disks of some fixed diameter[5] $b \leq 1$ (dark gray in Figure 12) on the surface of a cylinder $\mathcal{C}$, construct closed disks of diameter $2b$ (lighter gray in Figure 12) concentric to the smaller ones. Call Ω the set of these larger disks. Take a point P higher than any point of Ω. We say that a configuration is *admissible* if the connected component of P in the complement Ω^c is bounded below. Call this the *top component* $\mathcal{A}$ of the configuration.

Definition 3.1. (Disk stacking process $\mathcal{S}$) Given an admissible configuration of disks of diameter b, add a new disk of diameter b centered at the lowest point C of the boundary $\partial\mathcal{A}$ of the top component.

In practice, C is the lowest point of the connected component of $\partial\mathcal{A}$ that separates the cylinder into a part that contains $\mathcal{A}$ and an other that contains arbitrarily low points of the cylinder.

We call the new added disk the *offspring* of the configuration. Once the offspring is added, we obtain a new admissible configuration. Indeed, consider the closed disk $\mathcal{D}$ of diameter $2b$ about C. Adding $\mathcal{D}$ to Ω makes the new top component a subset of the former one. The new com which makes the new component bounded below. Hence the process can be iterated indefinitely.

Lemma 3.1. (No overlap condition) *The offspring of a configuration does not overlap the interior of the disks of the configuration.*

Proof. Since the center of the offspring is on a component of the boundary of Ω, which is made of arcs of the circles of diameter $2b$, it is at distance at least b from any (dark) disk in the configuration. □

Lemma 3.2. (Opposedness condition) *The offspring of a configuration is tangent to two disks of the configuration on opposite sides of a vertical line through the center of the offspring.*

Proof. To prove this, we show that the lowest point C of ∂A is at the intersection of two arcs of circles that bound disks of Ω, and that the centers of these circles are on opposite sides of the vertical through C. Since $\partial\mathcal{A}$ is a union of arcs of circles bounding disks of Ω, C must belong to one of those arcs. Assume by contradiction that C is not an intersection point of the arc with another disk of Ω. Since C must be

[5]The notation is that of van Iterson [11]. It is a fundamental parameter in phyllotaxis, that can be interpreted as the ratio of the primordium diameter over the circumference of the meristem. In [30] the related parameter $\Gamma = b/2\pi$, the ratio of the primordium diameter over the *radius* of the meristem is used.

the lowest point on this arc, it must be the bottom point of the circle the arc is on. Since the disk D the circle bounds is in Ω, and C is in $\partial\mathcal{A}$, there must exist $\epsilon > 0$ such that the ball $B_\epsilon(C)$ intersects both D and $\mathcal{A}$, and no other disk of Ω. Since $B_\epsilon(C) \cap D$ is above C, the points of $B_\epsilon(C)$ vertically below C, are all in $\mathcal{A}$. But as $\mathcal{A}$ is bounded below, these points themselves must be vertically above some point of $\partial\mathcal{A}$. This contradicts the fact that C is the lowest point of $\partial\mathcal{A}$. Hence C is the intersection point between two boundary circles of disks of Ω, of centers that we denote by P_1 and P_2. This makes the offspring disk, of diameter b centered at C, tangent to the configuration disks centered at P_1 and P_2. We claim that these points are on opposite sides of the vertical through C. Indeed, suppose not and, without loss of generality both P_1 and P_2 are to the left of C. Then C is at the intersection of the two right half-circles of radius b centered at these points, and there are points below C on the lowest of these two half circles that belong to $\partial\mathcal{A}$, a contradiction. □

As mentioned in the previous section, we call the two disks of radius b centered at P_1 and P_2 the *parents* of the offspring, and we say that the offspring is the *child* of these two disks. Note that, there can sometime be a third disk of Ω passing through C, but only two of these disks may contribute to the two arcs forming the boundary $\partial\mathcal{A}$ around C. This gives an unambiguous definition of the parents of a child: out of the all the configuration disks tangent to an offspring, its parents must be the highest possible opposite pair.

3.2 $\mathcal{S}$ as a dynamical system

We have defined a disk stacking process that can be iterated indefinitely. To make it into a discrete dynamical system, we need to define the state space on which $\mathcal{S}$ acts as a map. Each disk of the configuration can be characterized by two variables, namely the two coordinates of its center. To obtain a phase space of fixed dimension, we consider admissible configurations of a large enough number K of disks (depending on the size b of the disks: the smaller b is, the larger K must be) and, as we add an offspring to the configuration, we remove the lowest disk in the configuration. The process becomes then a map $\mathcal{S} : \mathcal{C}^K \mapsto \mathcal{C}^K$. The map is multivalued at (non-generic) configurations which possess two or more possible offsprings at the same height. Think for instance of a configuration made of equally spaced, horizontally aligned disks: any disk above, and tangent to two neighboring disks of the line is a legal candidate.

We say that two configurations have same (oriented) shape if one can be translated (on the cylinder) to the other. Having the same shape is a relation of equivalence $\sim$, whose set of equivalence classes, $\mathcal{C}^K/\sim$ is the *shape space* of configurations. The shape space has dimension $2(K-1)$: every configuration in an equivalence class can be translated to a representative that has its lower disk centered at a $(0, 0)$. This reduces the numbers of degrees of freedom by 2.

Clearly $\mathcal{S}$ commutes with any translation: the offspring of a translated configuration is the translation of the offspring. This allows us to think of the map $\mathcal{S}$ as acting on $C^K/\sim$, and we keep the same notation $\mathcal{S}$ for this quotient map.

Rhombic tilings as periodic orbits, lattices as fixed points We defined in the previous section rhombic tilings as configurations with only rhombic transitions (Figure 2A). We argued there that the effect of $\mathcal{S}$ on the fronts of a rhombic tiling was to transposition of a pair of down and up vectors, and therefore, if there are M down, and N up vectors, a maximum of MN transpositions can take place before the front recovers its original order of up and down vectors, and hence its original shape. Hence *rhombic tilings arising from disk stacking are periodic orbits of period MN for $\mathcal{S}$ acting on shape space*.

Note that this argument seems to rest solely on algebraic and combinatorial facts about the tilings. The algebraic tack is indeed taken in [22], where a rhombic tiling of parastichy numbers (M, N) is defined as a set of points that correspond to sums of down and up vectors chosen among M given down vectors, and N up vectors. These vectors and their sums satisfy certain periodicity conditions. The periodicity

of rhombic tilings under $\mathcal{S}$ is proven somewhat differently from the above argument ([22], Proposition 6.4), by counting the number of points between a front and its translation by the vector formed by summing all the up vectors.

Sometime, when some of the down (or up) vectors are equal, the minimum period of the rhombic tiling is a proper divisor of MN. This occurs for configurations starting with chains of C_3 in the diagonal of the kite (Figure 6) where the 2 up vectors are equal. In the part of a diagonal that's in a petal of C_3 (boundary between Regions A and A'), the chain becomes, in two iterations, a front of a 3,2 rhombic tilings, with two of its three down vectors equal (see Figure 28). The resulting configuration has period 3, which divides the full period 6. In the part of the diagonal that's in the blue region (boundary between Regions C and C'), the chain is immediately a front of a 1,2 rhombic tiling, but with equal up vectors. Simple observation shows that these tilings have period 1, which obviously divides the predicted period $MN = 2$.

The latter configurations are examples rhombic cylindrical lattices where all the up vectors are equal, and all the down vectors are equal. In general, a *cylindrical lattice* is a set of points obtained as the integer multiples of a given generating vector on the cylinder (*i.e.* (mod (1, 0) in the plane); this can be thought of as a representation of the group $\mathbb{Z}$ as a subgroup of the cylinder, itself seen as the group $\mathbb{S}^1 \times \mathbb{Z}$, [22]). A *rhombic* cylindrical lattice is a cylindrical lattice where the two closest neighbors of any given point are equidistant to it. Their set, parametrized by their generator, forms the "van Iterson Diagram", a $PSL(2,\mathbb{Z})$–invariant binary tree of the the upper half plane, formed by arcs of circles (hyperbolic geodesics).

Any rhombic lattice obtained by disk stacking is a fixed point of $\mathcal{S}$ acting on shape space ([22], Proposition 6.4). Visually, rhombic lattices are "straightened-up" rhombic tilings. The set of fixed points is a proper subset of the van iterson diagram: the tree must be "pruned" to only comprise the lattices that are orbits of $\mathcal{S}$ [8, 11, 23, 27].

A natural question arises: *Are there any periodic configurations other than rhombic tilings for $\mathcal{S}$?* Proving Conjecture 1 would answer this question by the negative: if all configurations tend to, or become rhombic tilings, then no indefinitely repeating configuration could be other than a rhombic tiling itself. Certainly, among all configurations starting with chains of C_3, all periodic configurations are rhombic tilings.

3.3 Chains, fronts and their notches

Chains and their properties As we have seen above, to describe the zigzagging lines joining adjacent disks in the upper layer of a configuration we use the language of chains and fronts. We now make their definitions rigorous and derive some general properties of these chains. A *polygonal chain* in the plane [36] (or, simply, *chain* in this article) is a piecewise linear curve consisting of vertices $A_0, A_1, \ldots, A_N$ and the line segments $A_{k-1}A_k$, $k \in \{1, \ldots, N\}$, called edges, that connect consecutive vertices. The *length* of a chain is its number of edges. Choosing an order for the vertices confers an orientation to the chain , in which each edge becomes a vector $\overrightarrow{A_{k-1}A_k}$. A chain $A_0A_2\cdots A_N$ is *closed* if $A_0 = A_N$, and is *open* otherwise. A chain is *simple* if only consecutive edges (that includes the first and last, for closed chains) intersect at their common vertex. A chain is *equilateral* if its edges all have same length, which we denote generically by b, as the diameters of the disks in [11]. In this article, unless otherwise mentioned *all chains are assumed to be simple and equilateral*. We call a (simple, equilateral) chain a *chain of disks* if the open disks of diameter b centered at its vertices do not intersect.

These notions transfer readily to the cylinder $\mathcal{C}$, with additional features. Indeed there are two kinds of closed chains in $\mathcal{C}$: those that are contractible (*i.e.* continuously deformable to a point) and those that are not. We call the non-contractible closed chains in the cylinder *cylindrical chains*. A cylindrical chain wraps around the cylinder once. Drawn on the unrolled cylinder, a cylindrical chain is an open planar chain whose end points differ by the vector $(\pm 1, 0)$.[6]

[6]Note that an open planar chain whose end points differ by the vector $(n, 0)$, with n an integer different from ± 1 would

We denote by d_X the *open* disk of diameter b about a point X, by D_X the *open* disk of diameter $2b$ about X and by $C_X = \partial D_X$ the circle of diameter $2b$ about a X. The disks d_X and d_Y overlap if $\overline{XY} < b$. This is equivalent to $X \in D_Y$ and $Y \in D_X$.

By extension, we will say that, given b, *the points X and Y overlap* if $d_X \cap d_Y \neq \emptyset$. Using this terminology, a (simple, equilateral) chain is a chain of disks whenever no two of its vertices overlap.

To make this more precise, recall that an orientation of the plane is given by the choice of an ordered basis that is declared positively oriented - usually the canonical basis $\{\overrightarrow{e_1}, \overrightarrow{e_2}\} = \{(1,0),(0,1)\}$. Any other basis falls into the positive or negative orientation category according to the sign of the determinant of its vectors expressed in the original basis.

Bearing angles and hinge angles of a chain We denote by $\angle(\overrightarrow{v}, \overrightarrow{w})$ the angle obtained by basing the vectors $\overrightarrow{v}, \overrightarrow{w}$ at the same point and traveling counterclockwise from vector $\overrightarrow{v}$ to vector $\overrightarrow{w}$. We use the same notation for the measure, in radians, of that angle. If the measure θ of the angle is greater than π, we also give it the measure $\theta - 2\pi$ when convenient. We use the notation $\angle ABC = \angle(\overrightarrow{BA}, \overrightarrow{BC})$ for the angle formed by three points in the plane. We say that C is *to the right* of $\overrightarrow{AB}$ if $\angle BAC < 0$ and *to its left* otherwise.

These definitions also hold in the cylinder as long as the x coordinates of the vectors involved are less than 1 in absolute value.

The *bearing angle* $\angle\vec{v}$ of a vector $\vec{v}$ in the cylinder or the plane is the angle it makes with the oriented horizontal axis - in other words it is the angular coordinate of the vector when written in polar coordinates. Equivalently, $\angle\vec{v} = \angle(\overrightarrow{e_1}, \overrightarrow{v})$, where $\overrightarrow{e_1} = (1,0)$. In a chain $A_0A_2\cdots A_N$ we denote by $\beta_j = \angle\overrightarrow{A_{j-1}A_j}$, the bearing angle of the j^{th} vector of the chain.

Up and down vectors and parastichy numbers of a prone chain. We say that a chain $A_0A_2\cdots A_N$ is *prone* if its bearing angles $\beta_j \in (-\pi/2, \pi/2), j \in \{1,\dots,N\}$. Intuitively, a prone chain is oriented from left to right, and it does not fold over itself, and can only close by going around the cylinder. A prone chain is monotone with respect to the horizontal, in the language of polygonal chains [36]. A vector $\overrightarrow{A_{j-1}A_j}$ in a prone chain is called a *down vector* if its bearing angle $\beta_j \in (-\pi/2, 0)$ and an *up vector* if $\beta_j \in [0, \pi/2)$.

If a chain has m down and n up vectors, we say that it has *parastichy numbers* (m,n) and that it is an m,n-chain. If $N = m+n$, we also say that it is an N-chain. When in a configuration the parastichy numbers of successive fronts are constant, their parastichy numbers correspond to the classical parastichy numbers of cylindrical lattices , see Figure 2 ([12, 22]).

We say that a chain is a *notch* if it is prone, and it consists of $k+j$ vectors where the k first are down vectors and the j last are up vectors. Clearly such a notch has parastichy numbers k, j and we say it is a k, j-notch. A prone, cylindrical chain can always be decomposed into a sequence of notches: starting at the highest disk of the chain, the first vector must be down, and the last must be up.

Hinge angles and the no-overlap condition We define the *hinge angle* h_j of a chain $A_0A_2\cdots A_N$ by

$$h_j = \angle A_{j+1}A_jA_{j-1} = \pi + \beta_j - \beta_{j+1}. \tag{1}$$

(See Figure 13). These angles determine the shape of the chain. Note that, representing them in $(-\pi, \pi]$, $h_j > 0$ means the chain is having a "left turn" at A_j, whereas $h_j < 0$ means it's having a "right turn". Hence in Figure 13, the chain is making a left turn at A_1 and at A_3, and a right turn at A_2,

A consequence of the no-overlap condition in an equilateral chain of disks $A_0A_2\cdots A_N$ is that

$$\left|h_j\right| \geq \pi/3. \tag{2}$$

necessarily self intersect in $\mathcal{C}$, or would not be homeomorphic to the circle.

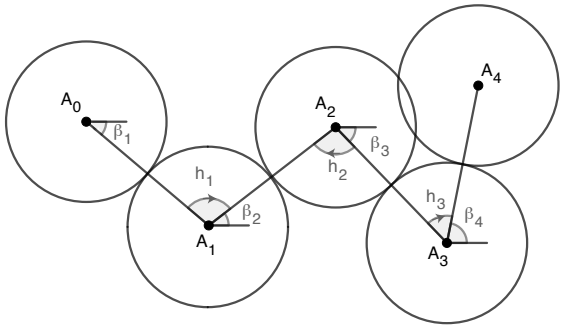

Figure 13: **Bearing angles, hinge angles, parastichy numbers and notches of a chain.** The chain $A_0A_1A_2A_3A_4$ is prone as $\beta_1, \beta_2, \beta_3, \beta_4 \in (-\pi/2, \pi/2)$ and equilateral, but it is not a chain of disks, since A_2 and A_4 overlap: $\pi - \beta_3 + \beta_4 = h_3 < \pi/3$. However the subchain $A_0A_1A_2A_3$ is prone, equilateral *and* a chain of disks: it has no overlaps. Neither chain is a cylindrical chain: A_0 and A_4 are not at the same height and thus could not represent the same point in the cylinder, and likewise for A_0, A_3. The vectors $\overrightarrow{A_0A_1}, \overrightarrow{A_2A_3}$ are down vectors since their bearing angles β_1, β_3 are negative. Likewise $\overrightarrow{A_1A_2}, \overrightarrow{A_3A_4}$ are up vectors since their bearing angles β_2, β_4 are positive. This means that $A_0A_1A_2A_3A_4$ has parastichy numbers (2, 2), whereas $A_0A_1A_2A_3$ has parastichy numbers (2, 1). $A_0A_1A_2A_3A_4$ is composed of the two 1,1-notches $A_0A_1A_2$ and $A_2A_3A_4$.

(or $h_j \in [\pi/3, 5\pi/3]$, when considering $h_j \in [0, 2\pi)$). Indeed $0 \leq h_j = \angle A_{j+1}A_jA_{j-1} < \pi/3$ implies that $\overline{A_{j+1}A_{j-1}} < b$, *i.e.* these two points overlap. In terms of the bearing angles, this local no-overlap condition is

$$\left|\beta_j - \beta_{j+1}\right| \leq 2\pi/3. \tag{3}$$

As could be expected, for a *prone*, *equilateral* chain of disks, the no-overlap with immediate neighbors implies no overlap at all:

Proposition 3.3. *An equilateral and prone chain in the plane, with hinge angles in* $[\pi/3, 5\pi/3]$ *has no overlap, i.e. it is a chain of disks.*

Proof. We prove the statement by induction on the length N of the chain. The first meaningful step is $N = 3$. Let $A_0A_1A_2$ be an equilateral, prone 3-chain. Its only hinge angle is $h_1 = \angle A_2A_1A_0$. Since $\overline{A_0A_1} = \overline{A_1A_2} = b$, the only overlap possible in the chain $A_0A_1A_2$ occurs when $\overline{A_0A_2} < b$, or equivalently $|\angle A_2A_1A_0| = h_1 < \pi/3$. Assume now by induction that any equilateral and prone chain of length strictly less than N with hinge angles within $[\pi/3, 5\pi/3]$ has no overlap. Let $A_0A_2 \cdots A_N$ be an equilateral, prone chain with hinge angles within $[\pi/3, 5\pi/3]$. The only points of the chain that could overlap are A_0 and A_N. Indeed, an overlap of A_j and A_k, with $\{j, k\} \neq \{0, N\}$, would contradict the induction hypothesis for the (prone, equilateral) subchain $A_j \cdots A_k$, which is of length strictly less than N.

Assume now by contradiction that A_0 and A_N overlap. Since the chain is prone, it is contained in the vertical strip of cylinder, call it $\mathcal{C}_{A_0A_N}$, between the vertical lines through A_0 and A_N (included): the chain would have to fold over itself otherwise. Without loss of generality we can also assume that A_1 is to the right of $\overrightarrow{A_0A_N}$, *i.e.* $\angle A_NA_0A_1 < 0$. We claim that A_{N-1} is then also to the right of $\overrightarrow{A_0A_N}$. If not, let $j \in \{1, \ldots, N-1\}$ be the last such that A_j is to the right of $\overrightarrow{A_0A_N}$. Then $\angle A_NA_0A_j < 0$ and $\angle A_NA_0A_{j+1} > 0$. Since $A_j, A_{j+1} \in \mathcal{C}_{A_0A_N}$, the segments A_jA_{j+1} and A_0A_N must cross and thus form the diagonals of a convex quadrilateral $A_NA_jA_0A_{j+1}$. Since A_0 and A_N overlap, these diagonals have both length $\leq b$, and at least one of the sides of the quadrilateral must have length less than b. But that means A_j and/or A_{j+1} overlap A_0 and/or A_N, a contradiction to our induction hypothesis. Since the chain is prone and both $A_1, A_{N-1} \in \mathcal{C}_{A_0A_N}$ and are to the right of $A_0\vec{A}_N$, we have

$$-\pi/2 < \angle\overrightarrow{A_0A_1} < \angle\overrightarrow{A_0A_1}, \quad \angle\overrightarrow{A_0A_1} < \angle\overrightarrow{A_{N-1}A_N} < \pi/2.$$

The line through A_0A_1 and the line through $A_{N-1}A_N$ must then meet at a point I in $\mathcal{C}_{A_0A_N}$ below A_0A_N. The law of cosines applied to the triangles $\triangle A_1IA_{N-1}$ and $\triangle A_0IA_N$, and their common angle $\angle A_0IA_N$,

shows that $\overline{A_1A_{N-1}} < \overline{A_0A_N} < b$, and hence A_1 and A_{N-1} overlap, a contradiction to our induction hypothesis. Thus A_0, A_N do not overlap. □

Remark 3.1. Note that if the angle condition for a prone chain was relaxed to allow bearing angle to roam over the *closed* interval $[-\pi/2, \pi/2]$,

the proof of Proposition 3.3 would still go through. The only case not covered is when A_1 is vertically below A_0 and A_{N-1} is vertically below A_N. In this case, $A_0A_1A_{N-1}A_N$ is a parallelogram, and thus $\overline{A_1A_{N-1}} = \overline{A_0A_N} < b$ yielding the contradiction that A_1 and A_{N-1} overlap if A_0 and A_N do. Note however that the boundary case $\overline{A_0A_N} = b$ is possible when we allow for vertical up vectors as well as vertical down vectors.

Propagation of chains and fronts All the configurations of disks that we will encounter in this paper are topped by a cylindrical chain. In fact, although we won't need this fact here, one can prove that any admissible configuration eventually yields a prone cylindrical chain on top of the configuration. We will say in this case that the configuration is topped by cylindrical chain. A precise way to say this that the complement of the disks (of diameter b) in the chain has two connected components, an upper one $\mathcal{U}$ containing arbitrarily high points of $\mathcal{C}$, and similarly for the lower component. The chain is on top of the configuration if the disks in the configuration are all in the complement $\mathcal{U}^\downarrow$ of $\mathcal{U}$. Equivalently, doubling the diameter of the disks, we get, using the notation in Definition 3.1, that the set Ω is bounded above by a curve that encircles the cylinder.

The following lemma shows that these top chains govern the dynamics of $\mathcal{S}$

Lemma 3.4. *If a configuration is topped by a prone cylindrical chain c of disks, then it is admissible and its image by $\mathcal{S}$ is also topped by a prone cylindrical chain of disks which is above c. A cylindrical chain is made of notches.*

Proof. Let a configuration be topped by a prone cylindrical chain of disks $c = A_0A_2\cdots A_N$. Since the chain is cylindrical, The complement of the set of closed disks of diameter b centered at its points separate the cylinder into an upper and a lower component.The set Ω consisting of disks of diameter $2b$ centered at the same points thus necessarily also separate the cylinder in two. Thus the chain c is an admissible configuration in of itself. By assumption the top component $\mathcal{A}$ of the complement of Ω is also the top component for the whole configuration. So the offspring K of this configuration is the same as the offspring of c. In particular, the parents of K are disks of c. One gets a new cylindrical chain c' of disks by taking the union of K and the points of c, and removing those that are strictly between the parents of K in c. This remains a prone chain, since the parents are on opposite sides of K by Lemma 3.2. Also, the removed points between the parents are below c', that is, in the complement of its top component $\mathcal{A}'$. Since $\mathcal{A}' \subset \mathcal{A}$ and the chain $c \subset \mathcal{A}^c$, we must have $c \subset \mathcal{A}'^c$, that is c' is above c.

To see that a prone cylindrical chain c is made of notches, start at the highest point of the chain. You must go down, and necessarily up again, since the chain is closed. Reaching the top of that first hill, if you are not back at the starting point, you necessarily have to go down again. Proceeding recursively this way, the last stretch is necessarily uphill since the start and end point is the highest. □

As mentioned earlier, if the offspring of the chain is higher than all the disks in the chain, we call the chain a *front* (see Figure 2). Although we will not need to prove this here, any chain that is not itself a front will eventually yield a front and from then on, the configuration is always bounded above by a front.

In a chain, the number of disks separating the parents of the offspring determines the parastichy numbers of the new chain formed. Indeed, if the parents of the offspring are adjacent, the offspring and its two parents form an equilateral triangle. This type of transition yields a net increase in one of the parastichy numbers of the chain, as one vector of the chain begets two new ones (Figure 14A). If there is exactly one disk of the front between the parents, that disk, the parents and the offspring form a a

rhombus (Figure 2B). In this case there is no net change in the parastichy numbers of the chain: the two front vectors involved are replaced by two parallel vectors, with a transposition in their order. More generally, we classify the type of transitions a new disk induces by the polygon it encloses with the the disks in the front: triangle, rhombus, pentagon and generally N-gon transitions. The general rule is that an N-gon transition adds a *total* of $4-N$ to the parastichy numbers.

By far the most common transitions in simulations are triangle, rhombus and pentagon transitions. They are the building blocks for all the commonly seen patterns in plants [12, 28]. Whereas it is possible to build chains or even fronts that yield N-gon transitions for any positive integer N (see *e.g.* the octagon in Figure 17B) in practice, transitions with $N = 6$ are very rare in computer experiments with random initial conditions, and, in our many simulations, we have never come across examples with $N > 6$. We suspect this to be the case in actual plant patterns as well.

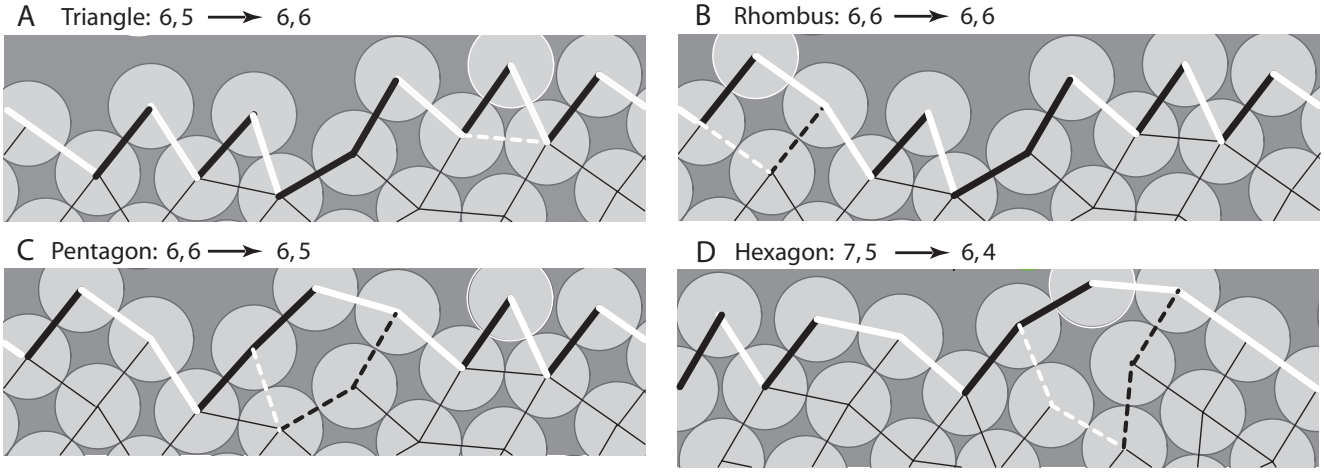

Figure 14: **Transitions in fronts.** The different transitions illustrate that an N-gon transition has the effect of changing the parastichy numbers by a total of $4-N$. **A.** A triangle transition increases one parastichy number by 4-3 = 1. **B.** A rhombic transition leaves parastichy numbers unchanged. **C.** Pentagon transition lowers one parastichy number by 1. **D.** A hexagonal transition that lowers by one each of the parastichy numbers.

Characterization of bearing angles of a cylindrical chain We spell out the restrictions on the bearing angles $\beta_1, \dots \beta_N$ of a prone, cylindrical N-chain $A_0A_2\cdots A_N$ of disks. Denoting by $v_k = \overrightarrow{A_{k-1}A_k}$, the k^{th} vector of the chain, we must have

$$\sum_{k=1}^{N} v_k = (1,0),$$

as the chain wraps around the cylinder. Since $v_k = b(\cos(\beta_k), \sin(\beta_k))$, this can be expressed as:

$$b\sum_{k=1}^{N} \cos(\beta_k) = 1 \tag{4}$$

$$\sum_{k=1}^{N} \sin(\beta_k) = 0 \tag{5}$$

Because of the chain is prone we must have:

$$-\pi/2 < \beta_k < \pi/2. \tag{6}$$

Since c is a chain of disks, it satisfies the no-overlap condition (Equation 3):

$$\left|\beta_{k+1} - \beta_k\right| \leq 2\pi/3 \tag{7}$$

where k and $k+1$ are computed mod N, that is, $N+1 \equiv 1$. In terms of hinge angles, this is simply $\left|h_j\right| \geq \pi/3$.

Putting these conditions together, we have:

Proposition 3.5. (Characterization of chains in terms of their bearing angles) *An N-tuple $(\beta_1, \beta_2, \ldots, \beta_N)$ of real numbers represents the bearing angles of an equilateral, prone, cylindrical chain of disks if and only if it satisfies Conditions (5), (6), (7) for all $k \in \{1, 2, \ldots, N\}$.*

Proof. The discussion above is essentially the proof of the forward implication in our statement. We now prove the converse. Any equilateral cylindrical chain with bearing angles $(\beta_1, \beta_2, \ldots, \beta_N) \in (-\pi/2, \pi/2)^N$ (Condition 6), that satisfies Condition 5 has its start and end points at the same height. Since for all k, $\cos(\beta_k) > 0$, one can find b such that Equation 4 is satisfied. Placing a disk of diameter b at each vertex of the chain, one obtains a chain of disks: the disks on two adjacent vertices are automatically tangent, and overlap is avoided by Equation 7. □

4 Offspring classification of 2- or 3-notches

We will see that, in the context of this paper, we are able to reduce the study of offsprings of configurations to those of prone chains, and then to offspring of notches to notches of length 2 or 3. This section classifies all possible transitions on these short notches, according to their hinge angles and one bearing angle (namely β_2), given us the solid building blocks to all the dynamics we will encounter.

4.1 More definitions and notation

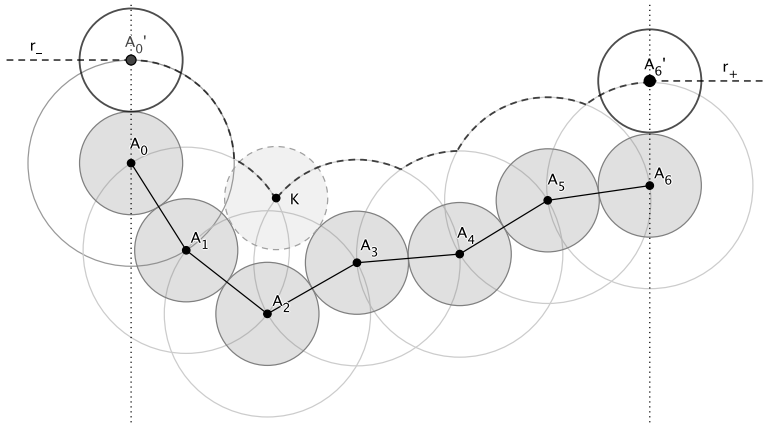

Figure 15: **Offspring of a notch** The chain $A_0A_1A_2A_3A_4A_5A_6$ is a prone notch of disks. The set Ω of disks of diameter $2b$ centered at the points of the notch together with the rays r_- and r_+ partition the plane in an upper and lower region. The lowest point of the upper boundary U (dashed) of that set is the offspring K.

Offspring of a notch Our definition of offspring of a notch is essentially the same as for an admissible configuration. In particular, it only depends on geometric data from the notch alone. To set it up requires a little work however.

Let $A_0A_2\cdots A_N$ be a notch and consider the union Ω of open disks $D_{A_0}, D_{A_1}, \ldots D_{A_N}$ of diameter $2b$. Let A_0' be the point at distance b vertically above A_0, and likewise for point A_N' and A_N. The chain

$A'_0A_0A_2\cdots A_NA'_N$ is prone, except for the fact that A'_0A_0 and $A_NA'_N$ are vertical. Applying Proposition 3.3 and Remark 3.1 to this chain implies that neither A'_0 nor A'_N belong to Ω: else these points would overlap with other points of the chain. Considering the notch as a chain in the plane, draw the infinite horizontal ray r_- starting from A'_0 pointing left, and another one, r_+, starting from A'_N pointing right. The complement of the set $\Omega' = \Omega \cup r_- \cup r_+$ in the plane has two unbounded components. The boundary of the top component is a curve comprising of the two rays, and arcs of some of the circles $C_0, C_1, \ldots, C_N$. We know that A'_0 and A'_N belong to the boundary of Ω since they do not overlap with other points of the chain. Orienting the curve from left to right, consider the segment U of it starting at A'_0 and ending A'_N. We define the offspring of the notch to be the lowest point of U. This definition works also for a chain made of multiple notches. It is not hard to see that the minimum does occur at the intersection of two circles C_{A_k} and C_{A_j}, and not on the rays r_- and r_+.

Notation for 2- and 3-chains Given an (open or closed) oriented equilateral 3-chain $ABCD$, as before we denote the bearing angles of the vectors $\overrightarrow{AB}, \overrightarrow{BC}, \overrightarrow{CD}$ by $\beta_1, \beta_2, \beta_3$ respectively, and we let $b = \overline{AB} = \overline{BC} = \overline{CD}$. The shape of the chain is determined by the two hinge angles h_1, h_2 which we re-baptize τ, γ:

$$\begin{aligned} \tau &= \angle CBA = \angle(\overrightarrow{BC}, \overrightarrow{BA}) &&= \pi + \beta_1 - \beta_2 \\ \gamma &= \angle DCB = \angle(\overrightarrow{CD}, \overrightarrow{CB}) &&= \pi + \beta_2 - \beta_3 \end{aligned} \tag{8}$$

See Figure 16, top left. The offspring of the chain is determined by the intersection of corresponding circles C_A, C_B, C_C, C_D of diameter $2b$. We denote by T_0 the point in $C_A \cap C_B$ that is to the left of $\overrightarrow{AB}$, and T'_0 the one on the right. Note that T_0 and T'_0 form equilateral triangles $\triangle ABT_0$ and $\triangle ABT'_0$ with the chain. We define similarly $T_1, T'_1 \in C_B \cap C_C$, and $T_2, T'_2 \in C_C \cap C_D$. The intersections of disks whose centers are separated by one vertex of the chain form rhombi with the chain. We call them $R_1, R'_1 \in C_A \cap C_C$ and $R_2, R'_2 \in C_B \cap C_D$, where R'_1 is to the right of $\overrightarrow{AC}$ and $R'2$ is to the right of $\overrightarrow{BD}$. Note that if $\tau < \pi$, $R'_1 = B$ and if $\tau > \pi$, $R_1 = B$, with a similar statement for γ, R_2, R'_2 and C. Finally P and P' are the intersection points of C_A and C_D (when it exists), with P to the left of $\overrightarrow{AD}$ and P' to the right.

We adopt the same notations for a 2 chains ABC, where it makes sense.

4.2 Offsprings of 1,1 notches

Even though the choice of offspring of a 1,1 notch is intuitively clear, its rigorous analysis is a good test ground for the concepts and methods used in the much more complicated case of 3-notches.

Proposition 4.1. *A 1,1-notch yields a triangle on the least steep of its two vectors if the notch angle $\tau \geq \frac{2\pi}{3}$ and yields a rhombus otherwise.*

Proof. Let ABC be a 1,1 notch with bearing angles $\beta_1 < 0 < \beta_2$. Assume $\boldsymbol{\tau \geq \frac{2\pi}{3}}$. The angles $\angle R_1CB$ and τ of the rhombus $ABCR_1$ add up to π. From our assumption, $\angle R_1CB = \pi - \tau < \frac{\pi}{3}$. Thus $\overline{R_1B} < b$ and R_1 overlaps B. If $\left|\beta_1\right| < |\beta_2|$, T_0 is lower than T_1 and is thus the offspring. Likewise, if $\left|\beta_1\right| > \left|\beta_2\right|$, T_1 is the offspring. When $\left|\beta_1\right| = \left|\beta_2\right|$ the offspring has the two values T_0 and T_1. [7]

Now let $\boldsymbol{\tau \leq \frac{2\pi}{3}}$. The triangles ABT_0 and BCT_1 are equilateral, thus $\angle CBT_0 = \angle T_1BA = \tau - \frac{\pi}{3} < \frac{\pi}{3}$. This implies $\overline{CT_0} = \overline{AT_1} < b$. This in turns means that T_0 overlaps with C and T_1 overlaps with A. On the other hand $\angle R_1CB = \pi - \tau \geq \frac{\pi}{3}$ and R_1 does not overlap with B: it must be the offspring. □

[7] In plants, this simple fact is actually rather momentous: The choice of T_0 or T_1 at a stage of the pattern formation determines the chirality of the subsequent spiral pattern, which varies within plants of the same specie and even different organs of the same plant [28].

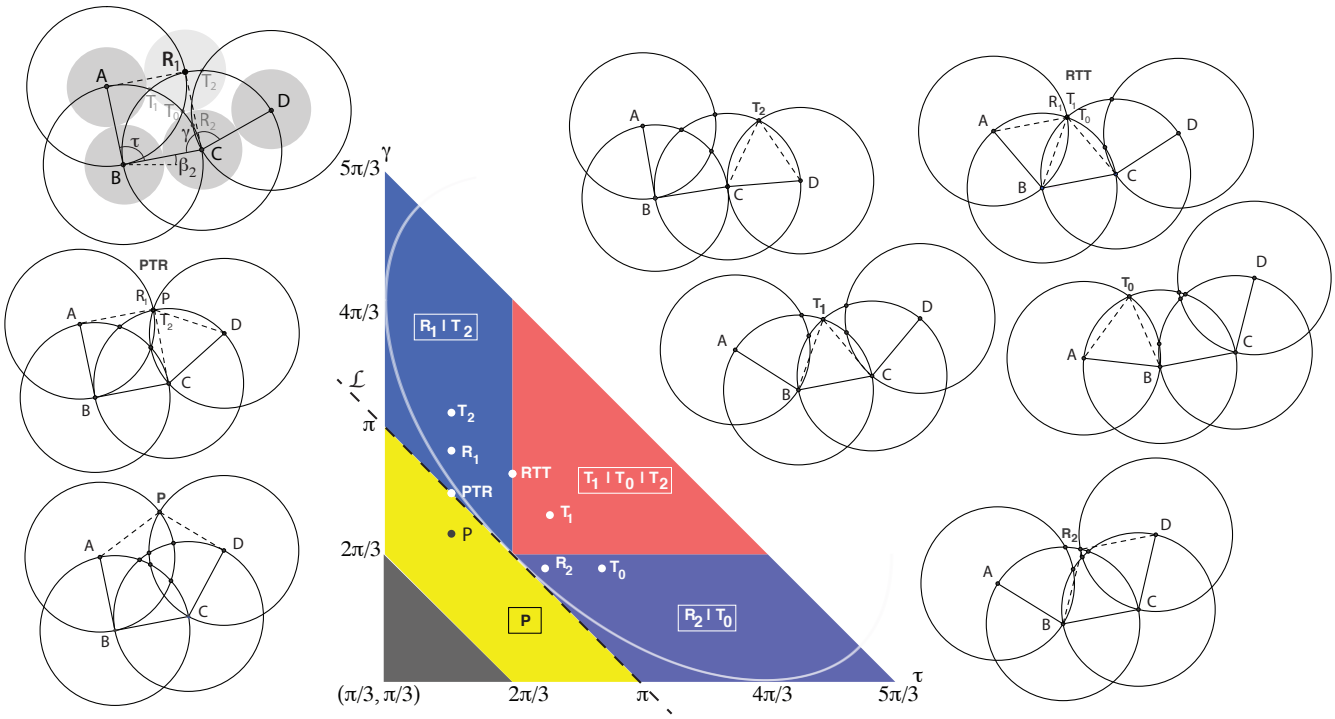

Figure 16: **Shape space of 3-chains and offsprings of 1,2-notches.** The shape of a 3-chain is parametrized by its hinge angles $\tau = \angle CBA$ and $\gamma = \angle DCB$. We chose $\beta_2 = \angle BC$ to control the angular orientation of the chain in the plane - it is the same for all chains (notches) represented here. We restricted the parameter space to $\tau \geq \pi/3, \gamma \geq \pi/3$ (no overlap) and $\tau + \gamma \leq \pi$ (chains which, given a proper β_2 are notches) and partitioned it according to which points of pairwise intersection of the circles C_A, C_B, C_C and C_D *do not* overlap with the points of the chain. The offspring of a notch is located at such a point, which are labeled according to the type of transition they give rise to: T for triangle, R for rhombus, P for pentagon. These regions' boundaries are determined in Lemma 4.2, with the most crucial, at the boundary of the region where P does not overlap, denoted by $\mathcal{L}$. The white, elliptical looking curve is the boundary of the region where P exists. Applying to a point in the triangular region the reflexion about the diagonal boundary $\tau + \gamma = \pi$ transforms a chain into one of same shape, rotated by π. Even though these chains can't be notches as they satisfy $\beta_1 > \beta_3$, the partition of that upper triangle of the parameter space is identical. See the online Geogebra file https://ggbm.at/prevpdfk for an interactive version of this figure.

4.3 Partition of the shape space of 3-chains according to overlaps

The location of the offspring of a 3-notch depends on both the overlaps of the intersection points of the circles C_A, C_B, C_C, C_D with the vertices of the notch, as well as on the overall orientation of the notch. We first concentrate on the overlaps, which are uniquely function of the shape of the notch, that is of the angles τ, γ. Figure 16 represents the shape space of 3-chains in the γ, τ-plane, partitioned according to the different possible offsprings the chains may have: the intersection points that do not overlap. This partition is established rigorously in the following lemma, which refers to the colored regions in Figure 16:

Lemma 4.2. *In a chain of disks $ABCD$ with hinge angles τ and γ, the following holds:*

(i) $\tau \in [\pi/3, 5\pi/3],\ \gamma \in [\pi/3, 5\pi/3],\ \tau + \gamma \geq \pi$ *(left and bottom sides of the triangle, and line between the grey and yellow regions)*

(ii) $\tau + \gamma = 4\pi/3 \Leftrightarrow R_1 = T_2 \Leftrightarrow R_2 = T_0 \Leftrightarrow P$ *and* P' *exist and* $\{T_0, T_2\} = \{P, P'\}$ *(line between the yellow and blue regions).*

(iii) $\tau + \gamma < 4\pi/3 \Leftrightarrow R_1$ *overlaps with* $D \Leftrightarrow T_2$ *overlaps with* $A \Leftrightarrow R_2$ *overlaps with* $A \Leftrightarrow T_0$ *overlaps with* D *(yellow region: no T's or R's).*

(iv) $\tau + \gamma \leq 4\pi/3 \Leftrightarrow P$ *exists and does not overlap with any point in the chain (yellow region: P).*

(v) *$\tau+\gamma > 4\pi/3$ and $\tau < 2\pi/3 \Leftrightarrow T_0, T_1, R_2$ and P overlap with some point of the chain, and T_2, R_1 do not. $\tau+\gamma > 4\pi/3$ and $\gamma < 2\pi/3 \Leftrightarrow T_1, T_2, R_1$ and P overlap with some point of the chain, and T_0, R_2 do not. (Blue regions are R's or T's)*

(vi) *$\tau+\gamma > 4\pi/3$ and $\tau > 2\pi/3, \gamma > 2\pi/3 \Rightarrow R_1, R_2$ and P overlap with some point of the chain, and T_0, T_1, T_1 do not (pink region is only T's).*

(vii) *$\tau+\gamma > 4\pi/3$ and $\tau = 2\pi/3 \Rightarrow R_1 = T_0 = T_1$ and this point does not overlap with any vertex of the chain and neither does T_2, but R_2 and P do.*

$\tau+\gamma > 4\pi/3$ and $\gamma = 2\pi/3 \Rightarrow R_2 = T_2 = T_1$ and this point does not overlap with any vertex of the chain and neither does T_0, but R_1 and P do.

(Lines between blue and pink regions: some R's and T's coincide, P is out).

We leave the rather involved proof to Appendix A. The reader is urged to visually check its validity using the online interactive version of Figure 16 in Geogebra https://ggbm.at/prevpdfk.

Remark 4.1. Note that an equivalent way to express the pentagon condition $\tau+\gamma \leq 4\pi/3$ is that the hinge angle between the first and last vectors of the notch is small enough:

$$\angle(\vec{CD}, \vec{BA}) \leq \pi/3.$$

Indeed, let I be the intersection of lines AB and CD, and consider the triangle $\triangle BIC$: it has angles $\angle B = \pi - \tau, \angle C = \pi - \gamma, \angle(\vec{CD}, \vec{BA}) = \angle I = \gamma + \tau - \pi$. So indeed $\tau+\gamma \leq 4\pi/3 \implies \angle(\vec{CD}, \vec{BA}) \leq \pi/3$

4.4 Offsprings of 3-notches

We now complement the statements of Lemma 4.2 by incorporating the information about the angular orientation of a notch to entirely determine its offspring as function of τ, γ and β_2.

Proposition 4.3. *The following table classifies the conditions under which the different candidates are offsprings of a 3-notch.*

<table>
<tr><td>$\gamma+\tau \leq 4\pi/3$
$(\beta_3-\beta_1 \geq 2\pi/3)$</td><td colspan="2"></td><td>P</td></tr>
<tr><td rowspan="6">$\gamma+\tau \geq 4\pi/3$
$(\beta_3-\beta_1 \leq 2\pi/3)$</td><td rowspan="2">$\tau \leq 2\pi/3$
$(\beta_2-\beta_1 \geq \pi/3)$</td><td>$\tau-\gamma+2\beta_2 \geq -\pi/3$
$(\beta_1+\beta_3 \geq -\pi/3)$</td><td>$R_1$</td></tr>
<tr><td>$\tau-\gamma+2\beta_2 \leq -\pi/3$
$(\beta_1+\beta_3 \leq -\pi/3)$</td><td>$T_2$</td></tr>
<tr><td rowspan="2">$\gamma \leq 2\pi/3$
$(\beta_3-\beta_2 \geq \pi/3)$</td><td>$\tau-\gamma+2\beta_2 \leq 2\pi/3$
$(\beta_1+\beta_3 \leq 2\pi/3)$</td><td>$R_2$</td></tr>
<tr><td>$\tau-\gamma+2\beta_2 \geq 2\pi/3$
$(\beta_1+\beta_3 \geq 2\pi/3)$</td><td>$T_0$</td></tr>
<tr><td rowspan="3">$\tau \geq 2\pi/3$
$\gamma \geq 2\pi/3$
$(\beta_2-\beta_1 \leq \pi/3)$
$(\beta_3-\beta_2 \leq \pi/3)$</td><td>$\tau \geq \pi-2\beta_2$
$(\beta_2 \geq \lvert\beta_1\rvert)$</td><td>$T_0$</td></tr>
<tr><td>$\{\tau \leq \pi-2\beta_2,\ \beta_2 \geq 0\}$ *or* $\{\gamma \geq \pi+2\beta_2,\ \beta_2 \leq 0\}$
$(0 \leq \beta_2 \leq \lvert\beta_1\rvert$ *or* $0 \leq -\beta_2 \leq \beta_3)$</td><td>$T_1$</td></tr>
<tr><td>$\tau \leq \pi-2\beta_2, \beta_2 \leq 0$
$(0 \leq \beta_3 \leq -\beta_2)$</td><td>$T_2$</td></tr>
</table>

Proof. The first two columns of the table correspond to the partition of shape space in Figure 16, and Lemma 4.2: the top row corresponds to the yellow region, and below that, in the second column, the first two cells correspond to the two blue region and the third cell to the red region.

Our task is now to further partition these four distinct regions into sub regions where only one offspring is possible. This is done according to the chain's angular orientation, as measured by β_2, under the

assumption that the chain is indeed a notch, *i.e.* $\beta_1 \leq 0 \leq \beta_3$. The sign of β_2 further determines the kind of notch the chain is: a 1,2 notch if $\beta_2 \geq 0$ and a 2,1 notch if $\beta_2 \leq 0$. The static Figure 16 cannot account for this added third dimension. It is best visualized with the interactive applet https://ggbm.at/prevpdfk, where a shaded square region represents the range of shapes that form a notch for a given value of β_2. This square, as well as (dashed) boundary lines separating the options in the colored region, move with the slider for β_2, sweeping over all the possibilities for the parameters τ, γ, β_2. In this proof, we use the inequalities in terms of $\beta_1, \beta_2, \beta_3$ that appear in parenthesis in the table. We let the reader translate the different cases in terms of the angles (τ, γ, β_2).

P when $\tau + \gamma \leq 4\pi/3$. As established in Lemma 4.2, the angle condition $\tau + \gamma < 4\pi/3$ insures that P is the only possible offspring: all the other potential points overlap with the notch's vertices. When the inequality is an equality, P is still the offspring, but it is also equal to either T_0 and R_2, or T_2 and R_1.

$\mathbf{R_1}$ vs. $\mathbf{T_2}$ when $\tau + \gamma \geq 4\pi/3, \gamma \leq 2\pi/3 : \mathbf{R_1} \Leftrightarrow \beta_1 + \beta_3 \geq -\pi/3$ (Top blue region). Lemma 4.2 shows that these two points are the only two free from overlap with notch vertices in this case. The offspring is the lowest of the two. The height difference between R_1 and C is $b\sin(-\beta_1)$. The height difference between T_2 and C is $b\sin(\beta_3 + \pi/3)$. If $\beta_3 + \pi/3 > \pi/2$, T_2 is to the left of both its parents C and D and thus can't be the locus of the minimum height. So we can restrict ourselves to the range $0 \leq \beta_3 + \pi/3 < \pi/2$ where sin is an increasing function. The angle $-\beta_1$ is also in this range, so:

$$R_1 \text{ is lower than } T_2 \Leftrightarrow -\beta_1 \leq \beta_3 + \pi/3 \Leftrightarrow \beta_1 + \beta_3 \geq -\pi/3$$

$\mathbf{R_2}$ vs. $\mathbf{T_0}$ when $\tau + \gamma \geq 4\pi/3, \gamma \leq 2\pi/3 : \mathbf{R_2} \Leftrightarrow \beta_1 + \beta_2 \leq 2\pi/3$ (bottom blue region). Similar to the previous case, except that we compare the differences of heights between B and T_0 ($b\sin(-\beta_1 + \pi/3)$) and between B and R_2 ($bsin(\beta_3)$) here.

$\mathbf{T_0}$ vs. $\mathbf{T_1}$ vs.$\mathbf{T_2}$ when $\tau + \gamma \geq 4\pi/3, \tau \geq 2\pi/3, \gamma \geq 2\pi/3$ (Red region): reduces to the 1,1 notch ABC if $\beta_2 \geq 0$ or to BCD if not.

Assume $\beta_2 \geq 0$. The other case is similar. We first show that T_2 is irrelevant in this case, by showing that its height is always greater or equal than that of T_1.

The difference of heights between T_1 and C is $b\sin(\beta_2 + 2\pi/3)$ and $b\sin(\beta_3 + \pi/3)$ between T_2 and C. Let $\omega_1 = \beta_2 + 2\pi/3$, $\omega_2 = \beta_3 + \pi/3$. Since $\beta_3 \geq 0$ and $\gamma \geq 2\pi/3$, $\omega_2 \in [\pi/3, \omega_1]$. The minimum of $\sin(\omega_2)$ on the sub-interval $\omega_2 \in [\pi/3, 2\pi/3]$ is attained at $\pi/3$ and $2\pi/3$. Since $\beta_2 < \pi/2$, we must have $\omega_1 \in [2\pi/3, 7\pi/6)$, and $\sin(\omega_2)$ is a decreasing function of $\omega_2 \in [2\pi/3, \omega_1]$ and thus has its minimum at $\omega_2 = \omega_1$ on that interval. Hence, we have proven that $\sin(\omega_2) \geq \sin(\omega_1)$, that is T_1 is always lower, or at same height as T_2 (equality occurs in the case $\omega_2 = \omega_1$, that is $\gamma = 2\pi/3$ or $\omega_1 = \pi/3, \omega_2 = 2\pi/3$, which happens when $\beta_2 = \beta_3 = 0$).

To determine the offspring of the notch, we thus have to compare the heights of T_0 and T_1. Given our assumptions, we have $2\pi/3 \leq \tau < \pi$, and ABC is a 1,1 notch. Proposition 4.1 implies that the offspring occurs at T_1 if $\beta_2 \leq \left|\beta_1\right|$, and at T_0 otherwise. □

4.5 Offsprings of chains of two short notches

In this section we show that, in the context of orbits of $\mathcal{S}$ starting on chains of C_3, we can reduce our study of offsprings of chains to that of notches of maximum length 3. This is because all the chains encountered will be of maximum length 5 and made of a maximum of 2 notches of types (1, 1), (1, 2), (2, 1). We will also encounter (2, 2) notches but whose offspring, by some distance estimates, will necessarily have their parents in a 2, 1 or 1, 2 sub-notch (see Corollary 6.3). At any rate, we will not encounter the case shown in Figure 17 b, of a chain of length 6.

Proposition 4.4. *Let c be a chain of disks with two notches, one of type (1, 1), the other of type (1, 1), (2, 1) or (1, 2). The offspring of c must have both it parents in one of the notches.*

Note that this statement does not preclude a parent being in two notches.

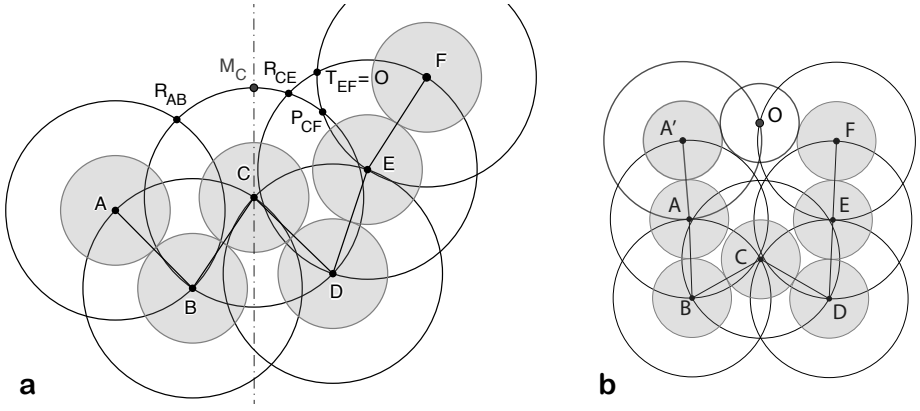

Figure 17: **Offsprings of chains with two notches. a.** The chain ABCDEF is made of the 1,1 notch ABC and the 1, 2 notch CDEF. If its offspring had parents A and E, it would be at the top intersection point of circles C_E and C_A. But such an intersection occurs only when R_{CE} is to the left of R_{AB}. That's impossible since R_{AB} is to the left of M_C, and R_{CE} is to the right of the same line, since $\vec{RC} \parallel \vec{AB}$, a down vector, and $\vec{CR'} \parallel \vec{DE}$, an up vector. Other possibilities are treated similarly. **b.** An example of a prone chain of disks composed of a 2,1 notch and a 1, 2 notch, and whose offspring straddles the two notches.

Proof. Without loss of generality, we treat the case of a chain ABCDEF with ABC a 1,1 notch, and CDEF a 1,2 notch. The other cases have similar proofs. The situation is illustrated in Figure 17.

Let us extend some prior notation for this proof. As before, we denote by C_X the circle of radius b centered at X, and by D_X the open disk it bounds. We denote the upper intersection point of C_X and C_Y by T_{XY} if X and Y are adjacent in our chain (triangle case), by R_{XY} when they are separated by one point (rhombus case), P_{XY} when they are separated by 2 points (pentagon). We also denote by M_X the top point of the circle C_X.

Given a prone chain $c = A_0A_2\cdots A_N$, we call $U(c)$ or U the upper boundary of $\Omega = \bigcup_{k=0}^{N} D_{A_k}$ in the strip $\mathcal{C}_{A_0A_N}$ (see Figures 15, and 18). We claim that if c is made of 1,1 notches, then $U(c)$ is a graph over the horizontal axis. Proving is reduced to the case of 1,1 notches of the chain, which we do in the caption of Figure 18. Note that the analysis shows that if ABC is a 1,1 notch, the curve $U(ABC)$ must start at M_A and end at M_C.

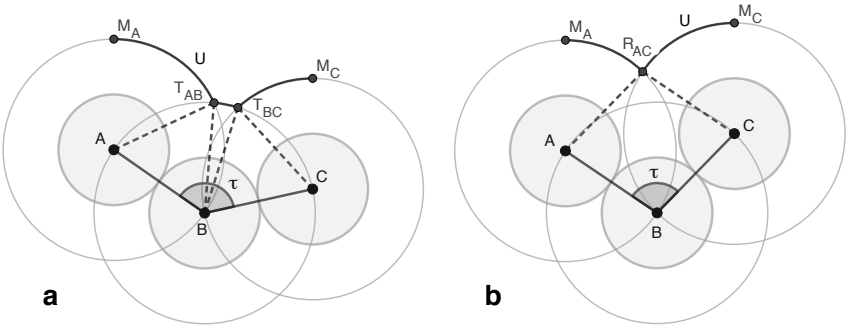

Figure 18: **Curve U on a 1,1 notch is always a graph. (a)** When the hinge angle $\tau \geq 2\pi/3$, the curve U must contain the triangle points T_{AB} and T_{BC} (and not R_{AB} which overlaps with B, and is thus inside D_B). Since $\beta_1 = \angle\overrightarrow{AB} > -\pi/3$ (else we would have $\angle\vec{BC} < 0$), $\angle\overrightarrow{AT_{AB}} = \beta_1 + \pi/3 > 0$ and thus the arc of U between M_A and T_{AB} is on the upper half circle of C_A. Similar reasoning applies to the other 2 arcs of U. **(b)** When the angle $\tau \leq 2\pi/3$, U must contain the rhombic point R_{AB} (and not the triangular points T_{AB} and T_{BC} which overlap with C and A respectively). Since $\angle\overrightarrow{AR_{AC}} = \angle\overrightarrow{BC} \in [0, \pi/2)$ the arc of U between M_A and R_{AC} is on the upper part of C_A and hence a graph over the x-axis, and likewise for the arc between R_{AC} and M_C.

Back to our prone chain of disks $c = ABCDEF$, its subchain $ABCDE$ is made of two 1,1-notches and the curve $U(ABCDE)$ is thus a graph, and always contains an arc of the circle C_C and the point M_C.

We first show that A and D (and, symmetrically, E and B) can't be parents of the offspring of c. If they were, their child disk would be P_{AD} in the 3-chain $ABCD$. But, by Lemma 4.2 (iv), such a point exists without overlap with the other points of $ABCD$ only if the hinge angles add up to less than $4\pi/3$. But since $\angle CAB > \pi/3$ and $\angle DCB > \pi$ here, P_{AD}, if it exists at all, cannot be an offspring of $ABCD$, and thus even less so of the longer chain c. Likewise P_{BE} can't be an offspring of $BCDE$, nor of c.

To show that A and E can't be parents of the offspring of c, fix the chain $ABCD$ and let E rotate on C_D in its allowable angular range of $\beta_4 \in (0, \pi/2)$ (as $\overrightarrow{DE}$ is an up vector). Since $U(ABCD)$ is a graph, as β_4 increases the leftmost intersection point O of $U(ABCD)$ and C_E moves continuously to the left on $U(ABCD)$. For O to have parents A and E, it would have to be to the left of M_C. But $O = M_C$ means in particular that $O \in C_C \cap C_E$, *i.e.* $O = R_{CE}$. In the rhombus $CDER_{CE}$, $\overrightarrow{CR_{CE}} \parallel \overrightarrow{DE}$, and the latter has bearing angle less than $\pi/2$. In other words, for O to reach M_C, E would have to go beyond its allowable angular course on C_D (See Figure 17 a).

To show that A or B and F can't be parents of the offspring of c, we proceed similarly: we fix the chain $ABCDE$ and let F rotate on C_E in its allowable angular range of $\beta_5 \in (0, \pi/2)$. As before the leftmost point O of intersection of C_F and $U(ABCDE)$ (which is a graph) travels continuously to the left as the β_5 increases. And as before we show that O must be to the right of M_C and thus can never reach the disks C_B or C_A. For O to reach M_C would mean that $O \in C_C \cap C_F$, or in other words $O = P_{CF}$. But in the quadrilateral $CEFP_{CF}$, $\overline{CE} \geq \overline{P_{CF}F} = b$. This implies in turn that $\angle \overrightarrow{CP_{CF}} \leq \angle \overrightarrow{EF} < \pi/2$, and P_{CF} can't reach M_C.

We have exhausted all the possibilities, and shown that the offspring of c could not have parents in two different sub-notches. □

Finally, we show that in conditions where they will be encountered in this paper, the offsprings of 2,2-notches have both their parents in the same 1,2- or 2,1-sub notch. This finishes justifying our concentrating on understanding offsprings of notches of length no more than 3.

Proposition 4.5. *Let ABCDA be a 2,2-notch that is also a cylindrical chain of disks and let $b < 1/2$. The offspring of ABCDA has parents either both in the 1,2-notch BCDE or both in the 2,1-notch ABCD.*

Proof. If $b < 1/2$, the disks of diameter b at a point A and its translate by $(1, 0)$ to the right in the unrolled cylinder are too far to be parents of a disk of diameter b. □

4.6 Pentagon Lemma

The following lemma is a consequence of our study of shapes of 3-chains, and will be used repeatedly in Section 7.

Lemma 4.6. (Pentagon Lemma). *Let ABCDP be a non self-intersecting equilateral pentagon in the plane with inner angles greater or equal to $\pi/3$. Then ABCDP is convex and the hinge angle between any two non-adjacent sides is comprised in the interval $[0, \pi/3]$.*

Proof. We let $ABCDP$ be an equilateral pentagon with edge length b and all inner angles greater than or equal to $\pi/3$. We want to show that $\angle(\overrightarrow{CD}, \overrightarrow{BA}) \in [0, \pi/3]$. The proof for the other angles is obtained from this one by relabeling.

We first prove that $\angle(\overrightarrow{CD}, \overrightarrow{BA}) \geq 0$. When this angle is 0, AB and BC are parallel, so that $ABCD$ is a rhombus and $\overline{AD} = b$. If $\angle(\overrightarrow{CD}, \overrightarrow{BA}) < 0$, the rays continuing $\overrightarrow{BA}$ and $\overrightarrow{CD}$ intersect and simple trigonometry shows that $\overline{AD} < \overline{BC} = b$. The isosceles triangle $\triangle ADP$ must then have angle $\angle APD < \pi/3$, which contradicts our assumption about inner angles.

To prove $\angle(\overrightarrow{CD}, \overrightarrow{AB}) \leq \pi/3$, we rephrase it in terms of the hinge angles angles $\tau = \angle CBA, \gamma = \angle DCB$. Assuming $\angle(\overrightarrow{CD}, \overrightarrow{BA}) > 0$ and denoting by I the intersection point of the lines BA and CD, the triangle $\triangle BIC$ has angles $\angle B = \pi - \tau, \angle C = \pi - \gamma$ which makes $\angle(\overrightarrow{CD}, \overrightarrow{BA}) = \angle I = \tau + \gamma - \pi$.

The assumption on the inner angles implies that no two vertices of the pentagon overlap (in the sense defined in the beginning of this section). In particular, $ABCD$ can be seen as a chain of disks, with no vertices overlapping. Lemma 4.2 (iv) applies and shows that, since P exists and does not overlap with the other points of the chain, we must have $\tau + \gamma \leq 4\pi/3$, which is equivalent to $\angle(\overrightarrow{CD}, \overrightarrow{BA}) = \tau + \gamma - \pi \leq \pi/3$.

To prove the convexity of $ABCDE$, note that $\tau + \gamma \leq 4\pi/3$ and $\tau \geq \pi/3, \gamma \geq \pi/3$ implies $\tau \leq \pi, \gamma \leq \pi$. Relabeling the points, we find that all the inner angles are less than π, and thus the pentagon is convex. □

5 Parametrization of the space C_3

We first give the proper definition of C_3:

Definition 5.1. C_3 is the space of prone, cylindrical 3-chain of disks.

In other words, chains in C_3 are made of 3 disks of equal radius, that wrap around the cylinder without overlaps or switchbacks.

As before, we denote by $\{\beta_1, \beta_2, \beta_3\}$ the bearing angles of a 3-chain. The following proposition characterizes C_3 and its parametrization (see Figure 19):

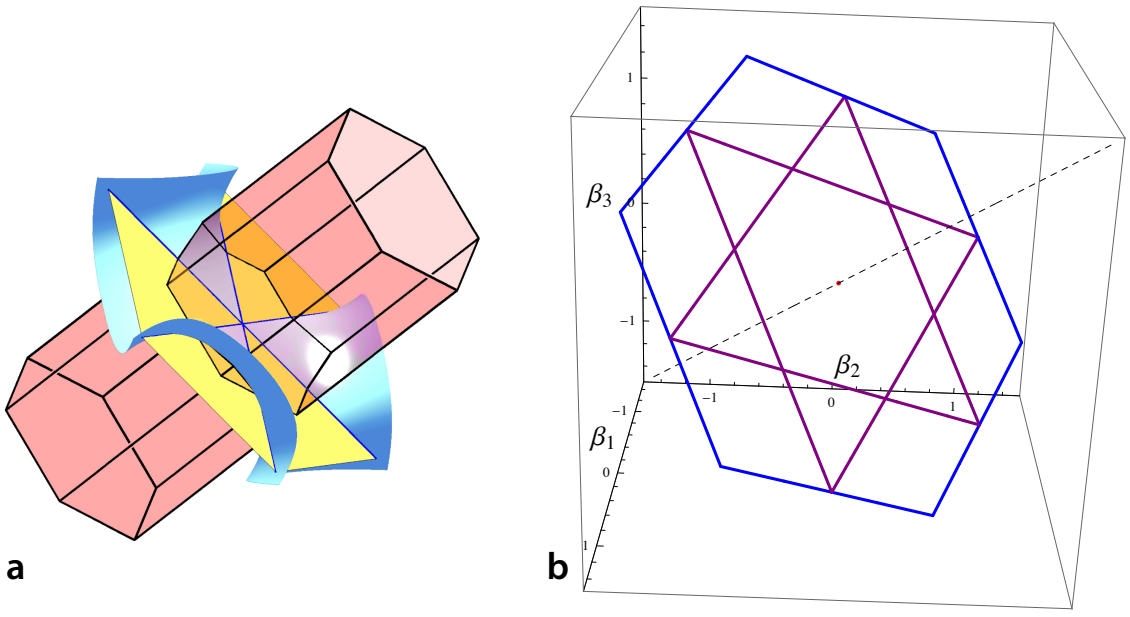

Figure 19: **Representation of C_3 in the space of bearing angles. a.** (Courtesy S. Hotton) The hexagonal prism (in pink) forming the boundary of the region satisfying $|\beta_{k+1} - \beta_k| \leq 2\pi/3,\ k \in \{1,2,3\}$, intersecting the surface $\sin(\beta_1)+\sin(\beta_2)+\sin(\beta_3) = 0$ (in blue) and its tangent plane $\mathcal{T}_0$ (in yellow). **b.** The hexagon, projection of C_3 on $\mathcal{T}_0$, which we use to parametrize C_3. The star of David inside the hexagon bounds regions with distinct dynamics.

Proposition 5.1. *C_3 is a bounded surface in the 3-space of bearing angles characterized by*

$$\text{(Cylinder chain)} \qquad \sin(\beta_1) + \sin(\beta_2) + \sin(\beta_3) = 0 \tag{9}$$

$$\text{(Prone)} \qquad |\beta_k| \neq \pi/2,\ k \in \{1,2,3\} \tag{10}$$

$$\text{(No overlap)} \qquad |\beta_{k+1} - \beta_k| \leq 2\pi/3,\ k \in \{1,2,3\} \tag{11}$$

The last condition is understood mod 3: if $k = 3$, we set $k + 1 \equiv 1$. C_3 is parametrized by the inverse of the orthogonal projection on its tangent plane $\beta_1 + \beta_2 + \beta_3 = 0$ at (0,0,0), with hexagonal domain that we call H_3, bounded by $\left|\beta_{k+1} - \beta_k\right| = 2\pi/3,\ k \in \{1,2,3\}$ (mod 3), with vertices removed.

The inequalities (11) represent 6 half spaces bounded by the planes $\beta_j - \beta_k = 2\pi/3, k \neq j \in \{1,2,3\}$, each of which contains the origin. Hence, C_3 is obtained by carving out the surface given by Equation (9) with a hexagonal "cookie cutter", conserving the boundary, except for the corners. See Figure 19.

Proof. The equations and inequalities characterizing C_3 in our statement are a direct application of Proposition 3.5, with the notable exception of Equation 10, which replaces the inequalities $-\pi/2 < \beta_k < \pi/2$ in that proposition. It turns out that, in C_3, strict inequality in (11) implies $-\pi/2 < \beta_k < \pi/2$. Although this can be proven using algebra, it is better seen geometrically through the contrapositive statement: if one of the bearing angles is strictly greater than $\pi/2$ in absolute value, overlap must occur. See Figure 20.

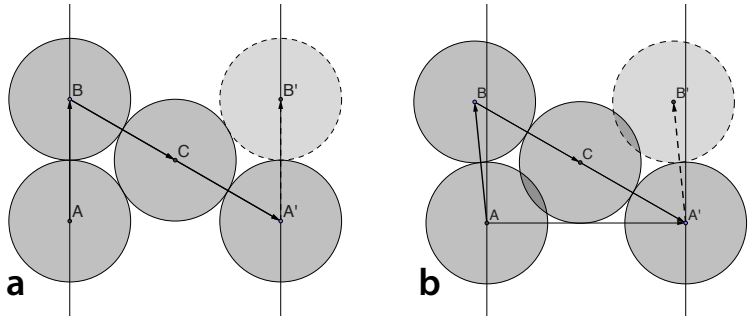

Figure 20: **Fold implies overlap in C_3. a.** The only possible cylindrical chain of disks with $\beta_1 = \pi/2$. The points A' and B' are identified to A and B in the cylinder. The figure shows the 3-chain of minimum disk diameter satisfying $\beta_1 = \pi/2$ ($b = 1/\sqrt{3}$ since $\left|BA'\right| = 2|AB|$). But this is also the only value of b where a 3-chain with $\beta_1 = \pi/2$ shows no overlap: the disk at C must overlap one of the 4 other disks if its diameter is increased. **b.** Overlap must occur when $\beta_1 > \pi/2$. For the given β_1, the figure shows the chain with smallest b. Overlap already occurs here and increasing b would make it worse.

We conclude from Figure 20 that there are only 6 chains that satisfy $\left|\beta_k\right| = \pi/2,\ k \in \{1,2,3\}$ with no overlap: the chain in Figure 20a, its reflection about the horizontal axis, and the 4 similar chains obtained starting the chain at B or C instead of A. These chains form the corners in the boundary of the admissible region for the no-overlap Condition (11): the configuration in Figure 20a satisfies $\left|\beta_2 - \beta_1\right| = 2\pi/3$ & $\left|\beta_3 - \beta_1\right| = 2\pi/3$.

Since the gradient vector of the function $\sin(\beta_1) + \sin(\beta_2) + \sin(\beta_3)$ is $(1,1,1)$ at $(0,0,0)$, the tangent plane of C_3 at $(0,0,0)$ has equation $\beta_1 + \beta_2 + \beta_3 = 0$. To parameterize C_3, we use the inverse map of the orthogonal projection on the tangent plane at the origin. This is possible since the projection is 1-1, as we prove in Appendix B. Since the 6 planes $\beta_{k+1} - \beta_k = \pm 2\pi/3,\ k \in \{1,2,3\}$ (mod 3) are all perpendicular to the tangent plane, they also bound the domain of the parametrization of C_3. □

In the rest of this paper, we identify C_3 with the domain of its parametrization, the closed hexagonal region H_3 in the tangent plane (with the vertices removed).

6 Dynamics on C_3: early iterations

We now explain in detail the effect on 3-chains of the first four iterations of $\mathcal{S}$. Our findings are summarized in Figure 21. Our first step is to reduce the hexagon H_3 parametrizing C_3 by symmetry. We then go into the fine geometric conditions that give rise to either rhombic, triangle or pentagon transitions. These conditions partition C_3 with the star of David figure and we then analyse the early dynamics of $\mathcal{S}$ in each region. A subsequent section delves into the asymptotic dynamics of chains in the inner hexagonal region.

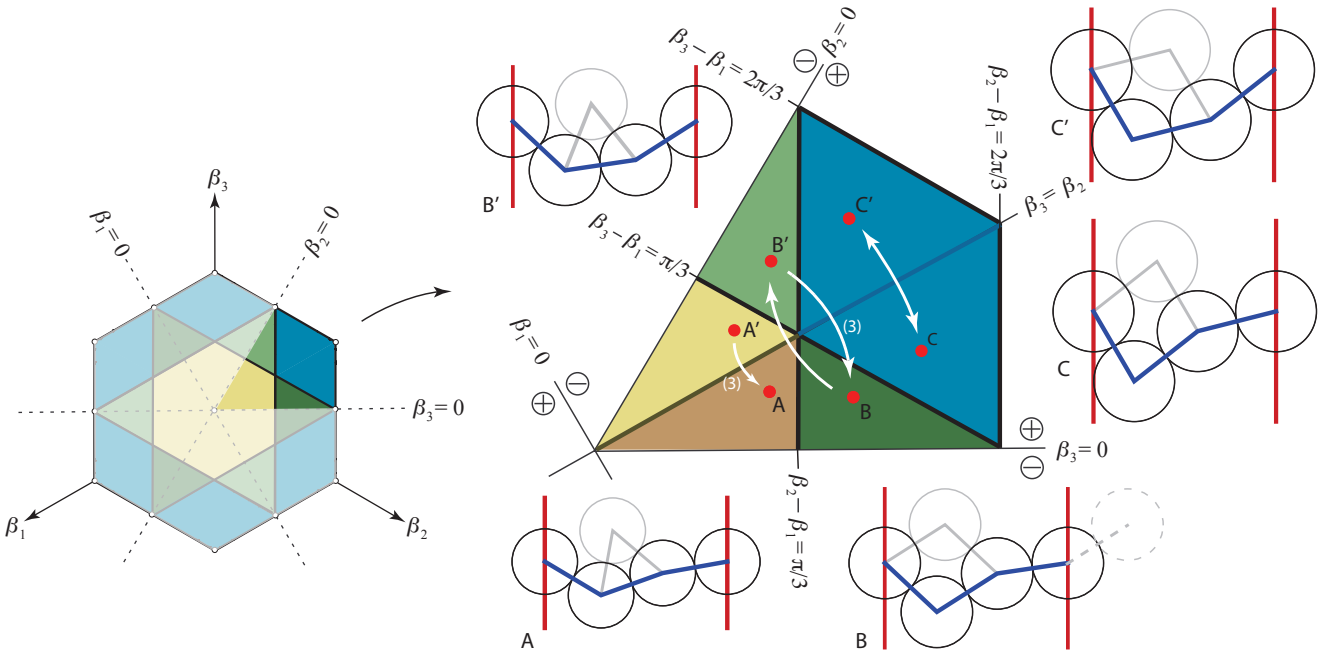

Figure 21: **Early dynamics of $\mathcal{S}$ on C_3. a.** On the left, the space C_3 of all 3-chains as represented by the hexagon H_3 in the tangent plane, seen from the axis $\beta_1 = \beta_2 = \beta_3$ perpendicular to it. On the right, by symmetry considerations, we concentrate on a kite-shaped sector of H_3 corresponding to 1,2-chains with bearing angles $\beta_1 \le 0, \beta_2 \ge 0, \beta_3 \ge 0$. A representative sample of such chains, with their respective offsprings is shown, with the points they correspond to in H_3. We use the names of these points to label their regions. Points in the regions A, A' and B', correspond to chains with triangle transitions, which exit C_3 upon the first iterate of $\mathcal{S}$. The regions B, C, C' correspond to chains that undergo a rhombic transition. The points corresponding to these chains are reflected about the diagonal axis $\beta_2 = \beta_3$ upon applying $\mathcal{S}$, as represented by the white arrows. Chains in Regions C and C' remain in C_3 forever under iterations of $\mathcal{S}$ as they are reflected indefinitely with period 2, thus generating rhombic tilings. Points on the darker segment of $\beta_2 = \beta_3$ correspond to lattices, which are fixed points for $\mathcal{S}$. All the chains above $\beta_2 = \beta_3$ (e.g. A', B', C') are reflected across that line (to A, B, C) in 3 iterates. This makes points in the regions B and B' periodic of period 4. Chains in the regions A and A' converge in either finite time, or infinite time to rhombic tilings chains. The map $\mathcal{S}$ is multivalued and discontinuous on the segment of $\beta_3 = 0$ bounding region A, as well as on its images under rotations by $\pm\frac{2\pi}{3}$.

6.1 Reduction of C_3 by symmetry

The definition of $\mathcal{S}$ relies entirely on geometry, and as such it interacts naturally with geometric operations that do not change shapes of chains, or change them in ways compatible with its action.

The shape of a chain is independent of the choice of starting point for the chain. This implies that relabeling the starting point of a chain is an operation that commutes with $\mathcal{S}$. This relabeling operation corresponds to circular permutations of the angles $\beta_1, \beta_2, \beta_3$. In the parameter space H_3, such a circular permutation is equivalent to a rotation by $2\pi/3$ or $-2\pi/3$ as the β_k-axes ($k \in \{1,2,3\}$) project to three evenly distributed rays. This explains the 3-fold rotational symmetry of the partition in the hexagon H_3 (see Figure 21, Left).

Hence, without loss of generality we can choose the highest point as first point of our chain. This is equivalent to restricting our study to the "first" sector, representing 1/3 of of the hexagon H_3, satisfying $\beta_1 \le 0$,and $\beta_3 \ge 0$.

This sector has itself a 2-fold symmetry, namely reflection about its bisecting plane $\beta_2 = 0$, which separates the sector into 2 kite-shaped regions. As can be seen by following the axes and their reflections about the line $\beta_2 = 0$ on the left of Figure 21, this symmetry corresponds to the transformation

$$\chi : (\beta_1, \beta_2, \beta_3) \mapsto (-\beta_3, -\beta_2, -\beta_1),$$

which amounts to reflecting about the vertical axis in the planar representation of the chain. Note that, in particular, χ turns up-vectors into down-vectors and vice-versa, and thus switches the parastichy numbers as well. In botanical language, χ has the effect of switching the chirality of the pattern. Note also that, because of its geometric definition, $\mathcal{S}$ commutes with χ: applying $\mathcal{S}$ to a chain and then χ has the same result as applying χ and then $\mathcal{S}$. This implies that our findings about the dynamical behavior of the chains in the lower half kite $\beta_1 \leq 0, \beta_2 \geq 0, \beta_3 \geq 0$ translate to the upper kite by reflection, as represented by the color scheme in Figure 21.

Definition 6.1. (Kite region $\mathcal{K}_{12}$) We let $\mathcal{K}_{12}$ be the lower kite region, which correspond to 1,2-chains whose first point is the highest, that is chains satisfying $\beta_1 \leq 0, \beta_2 \geq 0, \beta_3 \geq 0$.

In the remainder of the paper, we will study the dynamics of $\mathcal{S}$ with initial conditions restricted to $\mathcal{K}_{12}$. While the kite $\mathcal{K}_{12}$ has a remaining 2-fold symmetry along its long diagonal, we will see that, in some cases, it coincides with the action of $\mathcal{S}$.

For the record, here are the defining inequalities for the different sub-regions of $\mathcal{K}_{12}$:

Properties 6.1. As subsets of C_3, Regions A, B, C, A', B' , C' all satisfy:

$$\left|\beta_{k+1} - \beta_k\right| \leq 2\pi/3,\ k \in \{1,2,3\}\text{ , and }\ \sin(\beta_1) + \sin(\beta_2) + \sin(\beta_3) = 0.$$

And as subsets of the chosen kite region, they all satisfy

$$\beta_1 \leq 0,\ \beta_2 \geq 0,\ \beta_3 \geq 0.$$

Individually they further satisfy:

- Region A: $\beta_2 - \beta_1 < \pi/3,\ \beta_3 < \beta_2$ (or $\tau > 2\pi/3,\ \gamma > \pi$)
- Region A': $\beta_3 - \beta_1 < \pi/3,\ \beta_3 > \beta_2$ (or $\tau + \gamma > 5\pi/3,\ \gamma < \pi$)
- Region B: $\beta_2 - \beta_1 > \pi/3,\ \beta_3 - \beta_1 < \pi/3$ (or $\tau < 2\pi/3,\ \tau + \gamma > 5\pi/3$)
- Region B': $\beta_2 - \beta_1 < \pi/3,\ \beta_3 - \beta_1 > \pi/3$ (or $\tau > 2\pi/3,\ \tau + \gamma < 5\pi/3$)
- Region C: $\beta_3 - \beta_1 > \pi/3,\ \beta_3 < \beta_2$ (or $\tau > \pi/3,\ \tau + \gamma < 5\pi/3,\ \gamma > \pi$)
- Region C': $\beta_3 - \beta_1 < 2\pi/3,\ \beta_2 - \beta_1 > \pi/3,\ \beta_3 > \beta_2$ (or $\gamma + \tau > 4\pi/3,\ \tau < 2\pi/3,\ \gamma < \pi$)

Proposition 6.2. *In C_3, the maximum distance to the origin, and the maximum value for b are attained at the points corresponding to each of the 6 vertices of H_3. Likewise, on the regions of C_3 corresponding bounded by the inner hexagon and the two regions bounded by the triangles forming the star of David, these quantities are maximized at the vertices of these regions. The data is as follows:*

H_3. *Vertices*

$$\left\{\pm\left(-\frac{4\pi}{9}, \frac{2\pi}{9}, \frac{2\pi}{9}\right), \pm\left(-\frac{2\pi}{9}, -\frac{2\pi}{9}, \frac{4\pi}{9}\right), \pm\left(\frac{2\pi}{9}, -\frac{4\pi}{9}, \frac{2\pi}{9}\right)\right\}.$$

Distance to the origin: $\frac{2}{3}\sqrt{\frac{2}{3}}\pi \approx 1.71007$. $b = (\cos(4\pi/9) + 2\cos(2\pi/9))^{-1} \approx 0.586257$.

Rays of star of David. *Vertices (light and dark triangles respectively):*

$$\left\{\left(-\frac{\pi}{3}, 0, \frac{\pi}{3}\right), \left(\frac{\pi}{3}, -\frac{\pi}{3}, 0\right), \left(0, \frac{\pi}{3}, -\frac{\pi}{3}\right)\right\}, \qquad \left\{\left(-\frac{\pi}{3}, \frac{\pi}{3}, 0\right), \left(\frac{\pi}{3}, 0, -\frac{\pi}{3},\right), \left(0, -\frac{\pi}{3}, -\frac{\pi}{3}\right)\right\}$$

Distance to the origin: $\sqrt{2\pi/9} \approx 1.48096$. $b = 1/2$. *(Same for both triangles).*

Inner hexagon. *Vertices:*

$$\left\{\pm(p,q,q),\ \pm(q,p,q),\ \pm(q,q,p)\right\}$$

where $p = \cos^{-1}(2/\sqrt{7})) \approx 0.713724$ *and* $q = p - \pi/3 \approx 0.33347$. $b = 1/\sqrt{7}$.

Distance to the origin: $\sqrt{2(\pi/3 - \cos^{-1}(2/\sqrt{7}))^2 + \cos^{-1}(2/\sqrt{7})^2} \approx 0.85546$.

The proof is in Appendix C.

Corollary 6.3. In an orbit of $\mathcal{S}$ starting in the inner hexagon (*e.g.* regions A and A'), no chain can have an offspring with the same parent on the left and on the right.

Proof. For the same point to be the parents of the offspring on the left and on the right, its two representatives in the unrolled cylinder would have to be at distance less than $2b$. Since they are at distance 1, we should have $b \geq 1/2$. But Proposition 6.2 shows, for chains in the inner hexagon, that b is maximized at the vertices, where $b = 1/\sqrt{7} < 1/2$. □

An immediate consequence of this corollary is that, for a cylindrical 2,2-notch in an orbit of a chain in A, the parents of its offspring must both be in either its 2,1 or 1,2-sub-notch.

6.2 Partition of $\mathcal{K}_{12}$ in regions of rhombus and triangle transitions

Proposition 6.4. *A 1,2-chain in $\mathcal{K}_{12}$ has offspring T_1 when $\beta_2 - \beta_1 \leq \pi/3$ (subregions A, A', B'), and R_1 if $\beta_2 - \beta_1 \geq \pi/3$. On the plane $\beta_2 - \beta_1 = \pi/3$ between these two regions, these two offsprings coincide. On the boundary of $\mathcal{K}_{12}$ there are cases when the map $\mathcal{S}$ is multivalued and discontinuous, where it has one or two more equally possible offsprings other than T_1 or R_1. The choice of one offspring over the other in these cases either reflects the configuration about a vertical axis (with change of chirality) or has no effect:*

1. *On the lower boundary of sub-region A ($\beta_3 = 0, 0 \leq \beta_2 - \beta_1 \leq \pi/3$), offsprings: T_0 or T_1 (chirality change).*
2. *At the tip $(\beta_1, \beta_2, \beta_3) = (0, 0, 0)$ of $\mathcal{K}_{12}$, offsprings: T_0, T_1 or T_2 (no long term change).*
3. *On the vertical boundary $\beta_2 - \beta_1 = 2\pi/3$ of $\mathcal{K}_{12}$, offsprings: R_1 or T_2 (chirality change).*

Note that this statement extends to all of C_3 by symmetry. For instance, in the upper kite, *i.e.* for 2,1-chains, the same statement holds by swapping T_2 and T_0, R_2 and R_1. For the other sectors of C_3 the same 2 types of transitions occur, but with the second or third point of the chain being the highest. The net effect in C_3 is that the region inside the inner hexagon correspond to chains with triangular offspring, while the region outside of that hexagon corresponds to chains with rhombic offsprings.

Proof. We make repeated use of the angle conditions of Proposition 4.3. We rule out the offsprings P, T_0, R_2 and T_2 one by one, in this order (except for some boundary cases).

P The angle condition $\beta_3 - \beta_1 \geq \frac{2\pi}{3}$ for a pentagon transition is the opposite of one of the equations defining $C_3 : \left|\beta_3 - \beta_1\right| \leq \frac{2\pi}{3}$ (see Equation 11). In other words, pentagons can only occur at the upper boundary $\beta_3 - \beta_1 = 2\pi/3$ of sub-region C' of $\mathcal{K}_{12}$, where the points P, T_2 and R_1 coincide. Since $\angle \overrightarrow{T_2 C} = \angle \overrightarrow{R_1 C} = \beta_1 > -\pi/2$, T_2 is to the left of its parents C and D: we don't consider it a legitimate offspring in this case, but we interpret this case as an R_1 transition.

$\mathbf{T_0}$ For T_0 to be the offspring, we need $\tau \geq \frac{2\pi}{3} \Leftrightarrow \beta_2 - \beta_1 \leq \pi/3$ and $\left|\beta_1\right| \leq \beta_2$. If $\left|\beta_1\right| < \beta_2$, C is higher than A, and thus higher than $D = A + (1, 0)$, *i.e.* $\beta_3 < 0$. This means that the chain is not a 1,2-chain, but a 2,1-chain, which is not in $\mathcal{K}_{12}$. When the equality $\left|\beta_1\right| = \beta_2$ occurs, the angle β_3 must be 0. By symmetry, the offspring can either be T_0 or T_1 in this case. The map $\mathcal{S}$ is then multivalued, and discontinuous at these points. Choosing one or the other will affect the rest of the orbit by symmetry about the vertical line through B, *i.e.* a change of chirality.

$\mathbf{R_2}$ For R_2 to occur, we would need $\gamma \leq \frac{2\pi}{3}$. Since $\beta_2 \geq 0$, B is lower than C. But since A and $D = A+(1,0)$ are at the same height, we must have $\left|\beta_1\right| \geq \beta_3$. This in turn implies $\tau \leq \gamma$ as is readily seen on a sketch, or via algebra. Since $\gamma \leq \frac{2\pi}{3}$, we obtain $\tau + \gamma \leq \frac{4\pi}{3}$, the condition for a pentagon to occur, which we have already seen can only happen at the at the upper boundary $\beta_3 - \beta_1 = 2\pi/3$ of sub-region C', where $P = R_1 = T_2$, but does not equal R_2.

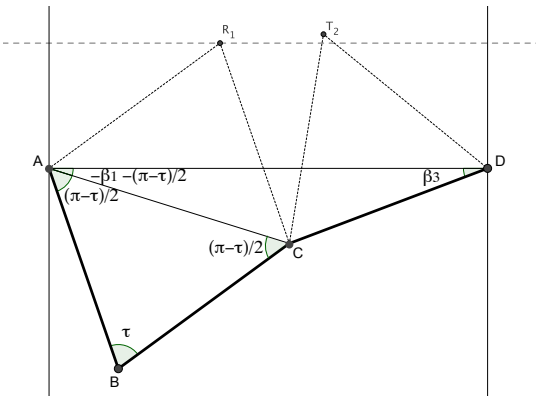

Figure 22: T_2 higher than R_1.

$\mathbf{T_2}$ We now show that, in $\mathcal{K}_{12}$, T_2 can only be the offspring at $(\beta_1, \beta_2, \beta_3) = (0,0,0)$, or at the vertical boundary $\beta_2 - \beta_1 = \pi/3$ of $\mathcal{K}_{12}$.

Assume first that $\tau > 2\pi/3$. Proposition 4.3 tells us that, for T_2 to be the offspring, we must have $0 \leq \beta_3 \leq -\beta_2$. Since in $\mathcal{K}_{12}$, $\beta_2 \geq 0$, this implies $\beta_2 = \beta_3 = 0$, which in turns implies $\beta_1 = 0$. There, the three triangle offsprings T_0, T_1, T_2 are equally possible: the map is multi-valued, and discontinuous at this point. But each of these points *will* eventually be offspring, and their order is indifferent to the overall, long range outcome, which is a 3,3-whorled pattern.

Now assume that $\tau = \angle CBA \leq 2\pi/3$ ((Figure 6.2). Since there is no overlap, $\tau \geq \pi/3$ and thus $\overline{AC} \geq \overline{CD} = b$.

This implies that $\angle CAD \geq \angle ADC$ (law of cosine in $\triangle ACD$). Since $\angle CAD = -\beta_1 - \left(\frac{\pi-\tau}{2}\right)$ and $\angle ADC = \beta_3$, we obtain $\beta_3 \geq -\beta_1 - (\pi - \tau)/2$ which, using $\tau \geq \pi/3$, yields:

$$\beta_3 + \beta_1 \geq -(\pi - \tau)/2 \geq -\pi/3.$$

When the inequality is strict, Proposition 4.3 implies that T_1 is the only offspring. When equality occurs, $\tau = \pi/3$ and thus the disks at A and C are tangent, and the offspring of $ABCD$ is the same as for the 1,1-notch ACD. Since A and $D = A + (1,0)$ are at same height, the offsprings R_1 and T_2 are equally possible. Since $\tau = \pi/3 \Leftrightarrow \beta_2 - \beta_1 = \pi/3$ this occurs at the right, vertical boundary of $\mathcal{K}_{12}$.

We have shown that, in the interior of $\mathcal{K}_{12}$ only R_1 and T_1 can be the offsprings: we have ruled out the other possibilities one by one. Since these two points are offsprings on the 1,1-notch ABC, R_1 is the offspring when $\tau \leq 2\pi/3 \Leftrightarrow \beta_2 - \beta_1 \leq \pi/3$ (corresponding to sub-regions A, A', B'), and T_1 is the offspring when $\tau \geq 2\pi/3 \beta_2 - \beta_1 \geq \pi/3$. At the boundary $2\pi/3 \beta_2 - \beta_1 \geq \pi/3$ between these two regions, the two offsprings coincide. On the boundary of $\mathcal{K}_{12}$, the map may be multivalued, but in each case either T_1 or R_1 is a possible offspring.

□

6.3 $\mathcal{S}$ acts as reflection in the right half of $\mathcal{K}_{12}$

As we have seen in the previous section, chains from Regions B, C and C' of the kite undergo a rhombic transition, which doesn't change the parastichy numbers. Hence the new chain is still a 1,2-notch, but with highest point R_1. Taking this point as the starting point of the chain, the set of bearing angles is the same as for the original chain, but with a permutation of the last two angles: $(\beta_1, \beta_3, \beta_2)$. That is, a generic point in the regions B, C, C' corresponds to a chain whose image under $\mathcal{S}$ is its reflection about the bissectrice $\beta_3 = \beta_2$ of the kite. Since Regions C and C' are images of one another under this reflection, any point in these regions correspond to a chain that comes back to itself in two iterates, with only rhombic transitions: they are (1, 2)-rhombic tilings. A special case is the chains that correspond to points on the diagonal $\beta_2 = \beta_3$ separating Regions C and C'. In this case, all the rhombi are identical, and the chains generate cylindrical lattices. These chains are fixed points in shape space: changing β_2 into β_3 has no effect on the shape of the chain. Summarizing these statements:

Proposition 6.5. *$\mathcal{S}$ acts as reflection about the line $\beta_2 = \beta_3$ in regions B, C and C′. The regions C and C′ correspond to 1,2 rhombic tilings, which are period 2 orbits for $\mathcal{S}$. The segment of line $\beta_2 = \beta_3$ separating C and C′ corresponds to rhombic 1,2-lattices, which are fixed points for $\mathcal{S}$.*

6.4 The upper half of $\mathcal{K}_{12}$ reflects into the lower half under $\mathcal{S}^3$

Proposition 6.6. *Chains in the upper region $A' \cup B' \cup C'$ of $\mathcal{K}_{12}$ are reflected into chains in the lower region $A \cup B \cup C$ after 3 iterates of $\mathcal{S}$. Chains in B reflect back to B' and thus chains in $B \cup B'$ have period 4 under $\mathcal{S}$. They form Benhardt rhombic tilings. Chains in the boundary between Regions A and A' have period 3.*

More notation For the figures (in this section and next) where disks are numbered, we refer to chains, angles and polygons by numbers separated by period signs, *e.g.* 5.6.4.5, ∠4.1.3. To denote the types of transitions (triangle, rhombic, pentagon), we use the letters T, R, P together with the indices of the two parents. Hence T_{25} is a triangle transition on the two parents 2 and 5, $R_{(11)8}$ is a rectangle transition with parents 11 and 8.

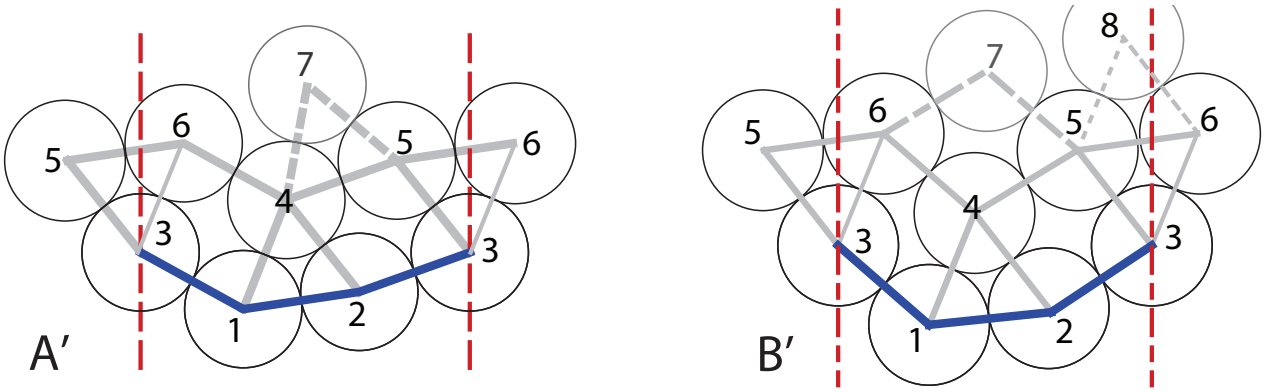

Figure 23: **Early dynamics in Regions A' and B'.** Chains corresponding to points in these regions yield, after 3 iterates of $\mathcal{S}$, their reflection about $\beta_3 = \beta_2$ in the kite. Both chains satisfy $\beta_2 - \beta_1 < \pi/3$ and $\beta_3 \leq \beta_2$ and undergo a triangular transition (Point 4) in the first iterate and a rhombic one (Point 5) in the second iterate. The third iterate (Point 6) has the double interpretation of a rhombus/pentagon transition and yields the chain 6.4.5.6 which has the same vectors as the original 3.1.2.3, but with the two up-vectors in reversed order: the chain corresponds to the lower kite point which is the reflection of the original around $\beta_2 = \beta_3$. The choice of Point 7 is where the two situations differ. The rhombic transition in the chain B' switches the 2 up vectors back to their original order, yielding a chain 7.5.6.7 that is a translation of the original one, showing that $\mathcal{S}$ is of period 4 on chains of Region B' (but not on those of Region A'). The next offspring in B' (Point 8) forms the characteristic double triangle of Benhardt tilings.

Proof. Take a chain in the upper region of the kite where $\beta_3 \geq \beta_2$ (Region $A' \cup B' \cup C'$ in Figure 21). We first assume that $\beta_2 > 0$ and will treat the boundary case $\beta_2 = 0$ later. From Proposition 6.5, a chain in Region C' is reflected to one in Region C under one iteration of $\mathcal{S}$. In two more iterations, the chain does a round-trip C→ C'→ C, reflecting about $\beta_3 = \beta_2$ each time. Thus our statement is proven in this case.

For chains in A'∪ B', we proceed step by step, showing that the evolution of their orbit is indeed universally captured by Figure 23.

Disk 4: T_{12} A chain A'∪ B' satisfies $\beta_2 - \beta_1 < \pi/3$. Since the chain is a 1,2-notch, $\beta_2 \leq |\beta_1|$ and by Proposition 6.4, its offspring Point 4 must be $T_1 = T_{12}$ here.

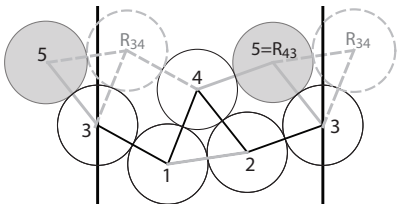

Disk 5: R_{43}. The chain 4.2.3.1.4 obtained after this first iteration has parastichy numbers (2,2) (so $\mathcal{S}$ immediately takes the original chain in C_3 to one in the space C_4 of 4-chains). We first claim that the next transition is rhombic. Indeed, there are 2 notches 3.1.4 and 4.2.3 in the chain 4.2.3.1.4, and the angles of these notches preclude a triangle transition: $\angle 4.1.3 < 2\pi/3$ since $\angle 2.1.3 \leq \pi$ (as $\beta_1 \leq 0 \leq \beta_2$) and $\angle 4.2.1 = \pi/3$. Likewise $\angle 3.2.4 \leq 2\pi/3$ since $\beta_3 \geq \beta_2$, and $\angle 4.2.1 = \pi/3$.

When these inequalities become equalities, the offspring can be a triangle, but it can also be interpreted as a rhombus. Thus the offsprings of notch 3.1.4 is R_{34} and that of 4.2.3 is R_{43}

We now show that R_{43} is lower than R_{34}. The difference of height between $R_{43}$and Point 1 is the sum of the y-coordinates of $\overrightarrow{14}$ and $\overrightarrow{4R_{43}} = \overrightarrow{23}$. The height of R_{34} is the sum of y-coordinates of $\overrightarrow{13}$ and $\overrightarrow{3R_{34}} = \overrightarrow{14}$. Thus the difference of height between R_{34} and R_{43} is the difference between the y-coordinates of $\overrightarrow{13}$ and $\overrightarrow{23}$, namely $\left|\sin(\beta_1)\right| - \sin(\beta_3)$. This difference is positive since $\sin(\beta_2) > 0$ and $\sin(\beta_1) + \sin(\beta_2) + \sin(\beta_3) = 0$, and thus R_{43} is the offspring.

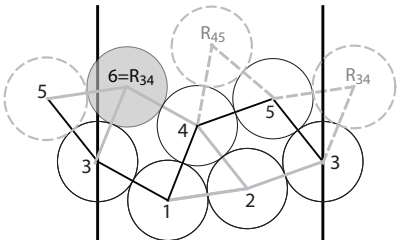

Disk 6: R_{34}. The chain 5.3.1.4.5 is a 2,2-notch. Corollary 6.3 implies that point 5 can't be both parent to the left and the right of the offspring. Thus we assume that both parents of the offspring are in the 1,2-notch 3.1.4.5 or both are in the 2,1-notch 5.3.1.4. We show that for both notches, the offspring is R_{34}.
Consider first 3.1.4.5. According to Proposition 4.3, we want to show that the bearing angles $\alpha_1, \alpha_2, \alpha_3$ of 3.1.4.5 satisfy

$$\alpha_3 - \alpha_1 \leq 2\pi/3, \quad \alpha_2 - \alpha_1 \geq \pi/3, \quad \alpha_3 + \alpha_1 \geq -\pi/3. \tag{12}$$

Note that $\alpha_1 = \beta_1$ (the notches 3.1.2.3 and 3.1.4.5 share their first vector $\overrightarrow{31}$), $\alpha_2 = \beta_2 + \pi/3$ ($\angle 2.1.4 = \pi/3$) and $\alpha_3 = \beta_3$ ($\overrightarrow{45} = \overrightarrow{23}$, by rhombic transition). Since $\beta_1 \leq 0 \leq \beta_2, \alpha_2 - \alpha_1 = \beta_2 - \beta_1 + \pi/3 \geq \pi/3$. Proposition 6.4 shows that $\beta_3 - \beta_1 \geq 2\pi/3$ (occurrence of a pentagon offspring) can only occur as an equality in $\mathcal{K}_{12}$, on the upper right boundary segment, which intersects Region B' at its top point (See Figure 21). This is also the endpoint of the boundary segment $\beta_2 = 0$, which we treat at the end of the proof. In all other cases, we have $\beta_3 - \beta_1 < 2\pi/3$ and thus $\alpha_3 - \alpha_1 < 2\pi/3$. We know $\beta_2 \geq 0$ and $\beta_2 - \beta_1 \leq \pi/3$, thus we have $\beta_1 \geq -\pi/3$. Since $\beta_3 \geq 0$, $\alpha_1 + \alpha_3 = \beta_1 + \beta_3 \geq -\pi/3$. Since $\angle 2.1.3 < \pi$ notch angle $\angle 4.1.3 = \angle 2.1.3 - \pi/3 < 2\pi/3$ which means $\alpha_2 - \alpha_1 > \pi/3$, and finishes to prove Equations 12 and thus that R_{34} is the offspring of 3.1.4.5.

Considering now notch 5.3.1.4. Note that, since $\overrightarrow{53} \parallel \overrightarrow{42}$, $\angle(\overrightarrow{35}, \overrightarrow{14}) = \pi/3$ and we're in Case (ii) of Lemma 4.2 where three different possible offsprings coincide. In this notch, this means that the offspring is $R_{34} = P_{54} = T_{53}$. This must also be the offspring of the whole chain 5.3.1.4.5.

4^{th} iterate as a reflection. Since $\overrightarrow{53} \parallel \overrightarrow{42}$ and $\overrightarrow{41} \parallel \overrightarrow{63}$, the third sides $\overrightarrow{12}$ and $\overrightarrow{56}$ of equilateral triangles $\triangle 3.6.5$ and $\triangle 1.2.4$ must be parallel. In other words, the chain 6.4.5.6 and the original 3.1.2.3 have same vectors, with their up vectors' order switched. If $\beta_1', \beta_2', \beta_3'$ are the bearing angles of chain 6456, then, in terms of the original bearing angles, we have $\beta_1' = \beta_1, \beta_2' = \beta_3, \beta_3' = \beta_2$. This shows that the two chains correspond to points that are reflections about $\beta_2 = \beta_3$ of one another.

Special boundary case. We now look at chains where $\beta_2 = 0$ (upper left boundary of $\mathcal{K}_{12}$). In this case, the chain is symmetric about the vertical line $x = 1/2$ $\beta_1 = -\beta_3$, and after the first triangle transition, it remains symmetric with Points 5 and 6 at the same height: $\mathcal{S}$ is multivalued at this 2,2-chains. But whatever the choice of offspring 5 or 6 at this stage, the next will be 6 or 5 respectively, as they don't overlap. Our reasoning about the resulting chain having same vectors with the order of the up vectors switched remains valid, even though one of them really is horizontal. The upper tip of Region B is an

even more special case: it has bearing angles $(-\pi/3, 0, \pi/3)$, which means that its offspring is tangent to all the disks of the notch, and to Disk 3 on both sides, forming a horizontal new chain. This is a case where all the possible offsprings $T_0, T_1, T_2, R_1, R_2, P$ coincide. The pattern generated is an hexagonal packing of circles. In terms of phyllotaxis, it corresponds to a 2,2 whorled pattern.

The fourth iteration of $\mathcal{S}$ is where the chains in Regions A' and B' behave differently. The two regions are separated by the plane $\beta_3 - \beta_1 = \pi/3$. For chains in A', we have $\beta_3 - \beta_1 \leq \pi/3$, which turns into $\beta_2' - \beta_1' \leq \pi/3$ in the chain 6456. By Proposition 4.3, this means that the notch angle $\tau \geq 2\pi/3$ and a triangle offspring must occur. Likewise, a rhombic offspring must occur at the 4^{th} iterate of $\mathcal{S}$ of a chain in B'. This rhombic transition has for effect another reflection about $\beta_3 = \beta_2$ which brings the chain back to its starting shape. Thus chains in B' are of period 4. And since any chain of B reflects to one in B' under $\mathcal{S}$, chains of B are also of period 4.

Chains from the diagonal of the kite bounding region A and A' where $\beta_2 = \beta_3$ still behave like those of the upper kite, in that their third iterates is also their image by the reflexion with respect to $\beta_2 = \beta_3$, which in this case is themselves. So chains on this axis have period 3 under $\mathcal{S}$.

Benhardt tilings. The chains in B and B' form Benhardt tilings (see Figure 3 B) under repeated iteration of $\mathcal{S}$: even though the first transition of a chain in B' is triangular, each subsequent triangle can be interpreted as a rhombus, as one triangle is stacked onto another one. For instance, in Figure 23 B', Point 8 can be interpreted as a triangle offspring of chain 7.5.6.7, with parents 5 and 6. But it can also be interpreted as a rhombic offspring of the chain 7.5.3.6.7, also with parents 5 and 6. These double triangles repeat periodically in the pattern.

□

7 Non periodic dynamics in Regions A and A'

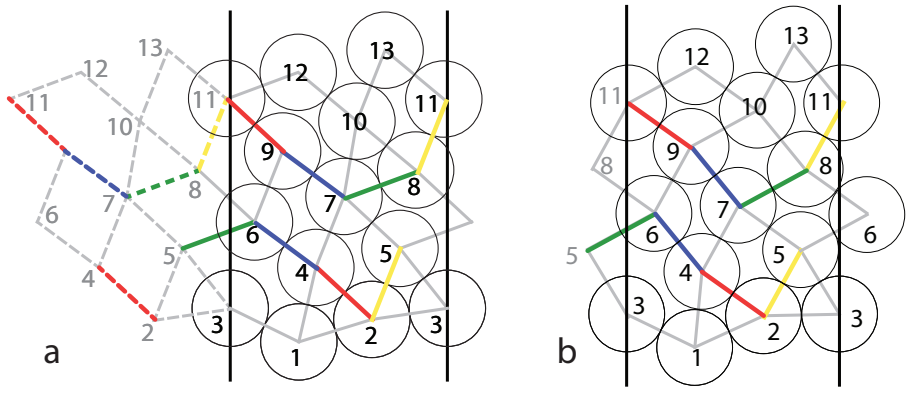

Figure 24: **Typical orbit of a chain in Region A.** Chains in Region A share the same type of transition at each step, at least until, in some cases (b), the triangle/pentagon pairs disappear at Disk 10. As shown by the color-coding, when the pairs of triangle/pentagon propagate, the new pair inherits its bottom vectors from the top vectors of the old one. Indeed, the shape of notch 11.9.7.8 is the same as that of the inverted notch 5.6.4.2, as one is obtained from the other by a translation and rotation by π. This provides a conserved quantity, namely the distance between Disks 2 and 5, for the dynamics of the sixth iterate $\mathcal{S}^6$ of the stacking process.

We have seen in the previous section that a chain in $\mathcal{K}_{12}$ can be periodic of period 1 (for chains at the boundary between Regions C and C'), of period 2 (in C and C'), period 3 (at the boundary between Regions A and A') and period 4 (in Regions B and B'). All these patterns are, at least after 1 iterates rhombic tilings. In all these cases, our understanding of the dynamics is thus complete. The long term dynamics in Regions A and A' (away from the diagonal $\beta_2 = \beta_3$) remain to be elucidated. As suggested by our numerical simulations, they display the richest and most surprising behavior of the

system: either finite or infinite convergence to rhombic tilings via pairs of pentagons and triangles. We show in this section that the way the pentagons change their geometry along the pattern determines whether these pairs disappear in finite time or continue for ever. More precisely, the conserved quantity $\overrightarrow{25} = \overrightarrow{8(11)} = \cdots = \overrightarrow{(2+6j)(5+6j)}, j \in \mathbb{N}$ provides the explanation for the shape of the petals in the rosace: their boundaries are isoline of $\left\|\overrightarrow{25}\right\|$ plotted in the proper coordinates.

Since by Proposition 6.6 chains from Region A' reflect into chains of Region A after 3 iterates, we concentrate on chains in Region A. We first determine how the pairs of triangles and pentagons come about in orbits of chains in A in a predictable way. We use the same notation for chains and their offsprings as in the previous section.

Lemma 7.1. *Chains in Region A all share the same transitions up to the 9^{th} disk. Disk 10 is either R_{98} or T_{78}. Disk 11 is always R_{89}.*

This means that for all chains in Region A, the transitions follow the same combinatorics as shown on Figure 24, up to Disk 9 included. For instance, for all chains in that region, Disk 7 has parents Disks 4 and 5 and occurs in a quadrilateral transition, *i.e.* R_{45}.

Proof. This proof refers to Figure 24, out of which we have extracted relevant sections as needed. Most of our conclusions, are, implicitly or explicitly, based on Proposition 4.3. We start with a chain of disks in the region A of $\mathcal{K}_{12}$, numbered according to the height order of the disks. The original chain is thus 3.1.2.3, and by definition of region A, $\tau = \angle 2.1.3 > 2\pi/3$ and $\beta_2 = \angle\overrightarrow{12} > \beta_3 = \angle\overrightarrow{23}$ (see Section 6.2). Since $\tau = \pi + \beta_1 - \beta_2$, and $\beta_1 \leq 0 \leq \beta_3 \leq \beta_2$, these inequalities can also be subsumed as:

$$0 \leq \beta_3 \leq \beta_2 \leq \left|\beta_1\right| \leq \pi/3 \tag{13}$$

We actually know a little more about these angles: let m be the point of intersection of the line through Points 1 and 2 and the horizontal through 3. Then, in the triangle $\triangle 3.1.m$, $\angle 3 = \left|\beta_1\right|, \angle m = \beta_2$ and $\angle 1 = \tau \geq 2\pi/3$, so that $\left|\beta_1\right| + \beta_2 \leq \pi/3$. Since $\left|\beta_1\right| \geq \beta_2$, we must have $\beta_2 \leq \pi/6$ and hence:

$$0 \leq \beta_3 \leq \beta_2 \leq \pi/6. \tag{14}$$

We now determine the parents - and thus the type of transition - for each successive offspring up to Disk 11.

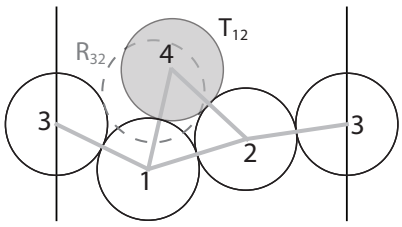

Disk 4: T_{12}. By Proposition 6.4, the chain 3.1.2.3, which is in $\mathcal{K}_{12}$ by assumption, can only have offsprings R_1 (= R_{32} here) or T_1 (= T_{12} here). By Proposition 4.3 it must be the latter since $\tau = \angle 2.1.3 > 2\pi/3$. Note that Disk 4 is higher than the other disks in the chain 3:1:4:2:3 obtained, since $\left|\angle\overrightarrow{31}\right| \leq \pi/3 \leq \angle\overrightarrow{14} \leq \pi/2$. The reader can likewise check in the rest of this proof that each successive disk is the highest in the new chain it forms. Hence all chains are fronts here.

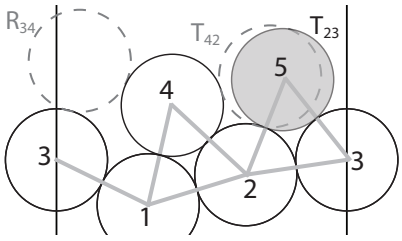

Disk 5: T_{23}. The chain 3.1.4.2.3 is composed of the two 1,1-notches, 3.1.4 and 4.2.3, whose offsprings we determine and compare in height. Since $\beta_1 \leq 0$ and $\beta_2 > 0, \angle 2.1.3 < \pi$. This implies that $\angle 4.1.3 = \angle 2.1.3 - \pi/3 < 2\pi/3$, and the offspring of notch 3.1.4 is R_{34}. Since $\angle 3.2.4 = 2\pi/3 + \beta_2 - \beta_3 > 2\pi/3$, the offspring of notch 4.2.3 must be either T_{42} or T_{23}. We now determine which of the two it is. Since the quadrilateral 3.1.2.4 is not rhombic, we have $\pi - \angle\overrightarrow{24} > \left|\beta_1\right|$, and by extension $\pi - \angle\overrightarrow{24} > \left|\beta_1\right| > \beta_3 = \angle\overrightarrow{23}$. This means that $\overrightarrow{24}$ is steeper than $\overrightarrow{23}$ and the offspring of notch 4.2.3 must be T_{23}. We must now compare the heights of the offsprings R_{34} of 3.1.4 and T_{23} of 4.2.3. The height difference between R_{34} and Disk 3 is $\sin(\angle\overrightarrow{14}) = \sin(\beta_2 + \pi/3)$. The height difference between T_{23} and

Disk 3 is $\sin(\beta_3 + 2\pi/3)$. From Inequalities (13) we obtain $\beta_2 + \pi/3 \in (\pi/3, 2\pi/3)$ and $\beta_3 + 2\pi/3 \in (2\pi/3, \pi)$. Thus $\sin(2\pi/3 + \beta_3) < \sin(\beta_2 + \pi/3)$, *i.e.* R_{34} is higher than T_{23}. Disk 5 is thus at T_{23}.

Summary of properties for 5.3.1.4.2.5. We now take stock of all the angle properties of chain 5.3.1.4.2.5. They will be crucial to the mechanism of infinite convergence.

$$0 \leq \angle\overrightarrow{25} - \pi/3 \leq \angle\overrightarrow{14} - \pi/3 = \angle\overrightarrow{42} + \pi 3 \leq \left|\angle\overrightarrow{31}\right| \leq \pi/3 \tag{15a}$$

$$\angle\overrightarrow{25} - \angle\overrightarrow{53} \leq 2\pi/3 \tag{15b}$$

$$\angle\overrightarrow{14} - \angle\overrightarrow{53} \geq 2\pi/3 \tag{15c}$$

Inequalities (15a) are a direct consequence of those in (13). Inequality (15b) is actually an equality here, since $\triangle 2.3.5$ is equilateral, but we will need this more general property for subsequent iterates of this pattern. Inequality (15c) derives from (15a): $\angle\overrightarrow{14} = \angle\overrightarrow{12} + \pi/3 \geq \angle\overrightarrow{23} + \pi/3 = \angle\overrightarrow{25} = \angle\overrightarrow{53} + 2\pi/3$, as $\triangle 235$ is equilateral. Thus $\angle\overrightarrow{14} - \angle\overrightarrow{53} \geq 2\pi/3$.

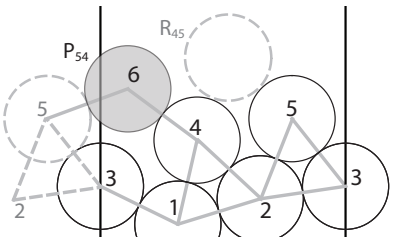

Disk 6: P_{54}. The chain at hand is now 5.3.1.4.2.5, which has the two notches 5.3.1.4 and 4.2.5. Inequality 15c is the difference between the first and third bearing angles of the notch 5.3.1.4. This inequality implies, via Proposition 4.3, that the offspring of this 2,1-notch is P_{54}. We now show that the offspring of 4.2.5 is R_{45}. From Equation 15a we have $(\angle\overrightarrow{24} - 2\pi/3) - (\angle\overrightarrow{25} - \pi/3) = (\angle\overrightarrow{42} + \pi/3) - (\angle\overrightarrow{25} - \pi/3) \leq \pi/3$, from which we deduce:

$$\angle 5.2.4 = \angle\overrightarrow{24} - \angle\overrightarrow{25} \leq 2\pi/3$$

and the offspring of 4.2.5 is indeed R_{45}. To compare the heights of these two notches' offsprings, note that P_{54} and R_{45} have the same parents, 4 and 5 (in the cylinder, but $5 - (1, 0)$ and 5 in the plane). We show that P_{54} is lower than R_{45} by showing that the x coordinate of $\overrightarrow{54}$ is greater than that of $\overrightarrow{45}$. We decompose $x(\overrightarrow{54}) = x(\overrightarrow{53}) + x(\overrightarrow{31}) + x(\overrightarrow{14})$. Since $\beta_3 \in (0, \pi/3)$, $x(\overrightarrow{53}) > x(\overrightarrow{25})$, as the latter vector is more horizontal than the former in the equilateral $\triangle 235$. We've seen that $\overrightarrow{42}$ is more vertical than $\overrightarrow{31}$, which implies $x(\overrightarrow{42}) < x(\overrightarrow{31})$. Since 4 is between its parents 1 and 2, $x(\overrightarrow{14}) > 0$. Putting these inequalities together, we get: $x(\overrightarrow{54}) = x(\overrightarrow{53}) + x(\overrightarrow{31}) + x(\overrightarrow{14}) > x(\overrightarrow{25}) + x(\overrightarrow{42}) + 0 = x(\overrightarrow{45})$.

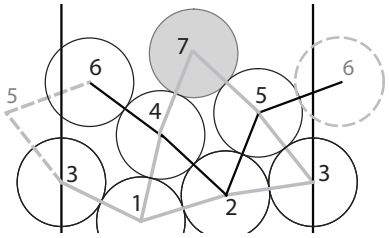

Disk 7: R_{45}. The chain we obtained in the previous step is the 2,2-notch 6.4.2.5.6. By Corollary 6.3, the offspring can't be hexagonal, with parents 6 (left) and 6 (right). The parents of the offspring are thus necessarily in one of the smaller sub-notches: the 2,1-notch 6.4.2.5 and/or the 1,2-notch 4.2.5.6 (with intersection 4.2.5). To show that notch 6.4.2.5 can't have P_{65} as offspring we estimate the difference $\angle\overrightarrow{25} - \angle\overrightarrow{64}$ between its third and first bearing angles.

Using Equation (15)b and the Pentagon Lemma 4.6 applied to the pentagon 3.1.4.6.5, and sides 53 and 64, we have $\angle\overrightarrow{25} - \angle\overrightarrow{64} = (\angle\overrightarrow{25} - \angle\overrightarrow{53}) + (\angle\overrightarrow{53} - \angle\overrightarrow{64}) \leq 2\pi/3 + 0$. Proposition 4.3 implies that P_{65} can't be the offspring of this notch. Likewise, using the Pentagon Lemma with the sides 56 and 14 of the same pentagon shows $\angle\overrightarrow{24} - \angle\overrightarrow{56} = \angle\overrightarrow{24} - \angle\overrightarrow{14} + \angle\overrightarrow{14} - \angle\overrightarrow{56} \geq \pi/3 + 0 \geq \pi/3$ which is equivalent to $\angle\overrightarrow{56} - \angle\overrightarrow{42} \leq 2\pi/3$ and Proposition 4.3 implies that 4.2.5.6 can't have P_{46} as offspring.

Notch 4.2.5.6 has notch angle $\angle 5.2.4 < 2\pi/3$ as we established in the previous case. Proposition 4.3 tells us its offspring may be either R_{45} or T_{56}, depending on whether the sum of its first and last bearing angles is greater or less (*resp.*) than $-\pi/3$. But the first angle is $\angle\overrightarrow{42}$ which is greater than $-\pi/3$

by Equation 15. The last angle, $\angle\overrightarrow{56}$ is positive: $\angle\overrightarrow{56} \geq \angle\overrightarrow{14} - \pi/3 \geq 0$ by the Pentagon Lemma and Equation (15). Thus the offspring of 4.2.5.6 is R_{45}. Similarly to 4.2.5.6, the notch 6.4.2.5 has notch angle $\angle 524 < 2\pi/3$, and symmetrically, we can establish T_{64} is not the offspring by estimating the sum of the first and last bearing angle of the notch. Summing its first and last bearing angles and using the Pentagon Lemma and Equation (15), we obtain $\angle\overrightarrow{64} + \angle\overrightarrow{25} \geq \angle\overrightarrow{31} - \pi/3 + \angle\overrightarrow{25} \geq \angle\overrightarrow{31} \geq -\pi/3$. Hence the offspring for this notch is also R_{45}. This must then be the offspring of the greater notch 6.4.2.5.6.

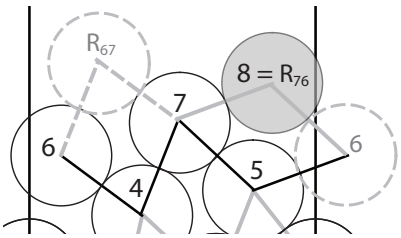

Disk 8: R_{76}. The chain at hand is now 6.4.7.5.6, composed of the two notches 6.4.7 and 7.5.6. We have $\angle 7.4.6 = \angle(\overrightarrow{47}, \overrightarrow{46}) = \angle(\overrightarrow{25}, \overrightarrow{46}) = \angle(\overrightarrow{52}, \overrightarrow{64}) = \pi/3 + \angle(\overrightarrow{53}, \overrightarrow{64}) \leq 2\pi/3$, the last inequality coming from the Pentagon Lemma 4.6, and hence the offspring is the rhombic R_{67} on notch 6.4.7. Likewise $\angle 6.5.7 = \pi/3 + \angle(\overrightarrow{56}, \overrightarrow{41}) \leq 2\pi/3$ by the Pentagon Lemma, and notch 7.5.6 has offspring R_{76}. We now need to compare their heights, which can be read off their y-coordinates:

$$y(R_{67}) - y(R_{76}) = y(\overrightarrow{7R_{67}}) - y(\overrightarrow{7R_{76}}) = y(\overrightarrow{46}) - y(\overrightarrow{56}) > 0,$$

since 5 is higher than 4, confirming that Disk 8 is R_{76}.

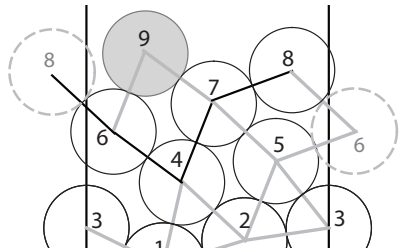

Disk 9: R_{67} The chain is now the 2,2-notch 8.6.4.7.8. The reasoning for this chain is similar to that for the 2,2-chain 6.4.2.5.6 (see Disk 7). In particular we can rule out an offspring with parents 8 and 8. The offspring must then be on either the 2,1-notch 8.6.4.7 or the 1,2-notch 6.4.7.8. We rule out pentagon offsprings in both. For 8.6.4.7, we do this by estimating the differences between the third and first bearing angle: $\angle\overrightarrow{47} - \angle\overrightarrow{86} = \angle\overrightarrow{25} - \angle\overrightarrow{42} = \beta_3 + \pi/3 - (\beta_2 - \pi/3) = \beta_3 - \beta_2 + 2\pi/3 \leq 2\pi/3$, since $\beta_3 - \beta_2 \leq 0$ in Region A. To show 6.4.7.8 can't have P_{68} as offspring, we show that the sum $\angle 7.4.6 + \angle 8.7.4$ of its hinge angles is greater than $4\pi/3$. We know that $\angle 7.4.6 \geq \pi/3$ since 6 and 7 don't overlap. Since 4 is lower than 5, which is lower than 6, $y(\overrightarrow{78}) = y(\overrightarrow{56}) < y(\overrightarrow{46}) \leq y(\overrightarrow{47})$ which implies $\angle\overrightarrow{47} > \angle\overrightarrow{78}$ and thus $\angle 8.7.4 > \pi$, proving that $\angle 7.4.6 + \angle 8.7.4 > 4\pi/3$, ruling out a pentagon offspring.

The notch angle for both 8.6.4.7 and 6.4.7.8 is $\angle 7.4.6$ which we showed is less than $2\pi/3$ in the Disk 8 step. So the offspring of notch 8.6.4.7 is either T_{86} (a.k.a. T_0 for this notch) or R_{67} (a.k.a. R_2); and the offspring of 6.4.7.8 is either R_{67} (a.k.a R_1) or T_{78} (a.k.a T_2). We rule out T_{86} as offspring of 8.6.4.7 by estimating the sum of first and last bearing angles of the notch: $\angle\overrightarrow{86} + \angle\overrightarrow{47} = \angle\overrightarrow{42} + \angle\overrightarrow{25} = \beta_2 - \pi/3 + \beta_3 + \pi/3 = \beta_2 + \beta_3 \leq 2\pi/3$ since by Equation (13) $0 \leq \beta_3 \leq \beta_2 \leq \pi/3$. We rule out T_{78} on 6.4.7.8, by looking at the difference of the two hinge angles plus two times the second bearing angle:

$$\angle 7.4.6 - \angle 8.7.4 + 2\angle\overrightarrow{47} \geq \pi/3 - 4\pi/3 + 2\pi/3,$$

where the second term is explained by the fact that Disk 5 stops Disks 4 and 8 to be too close, *i.e.* $\angle 4.7.8 \geq 2\pi/3 \Leftrightarrow \angle 8.7.4 \leq 4\pi/3$, and the other terms have already been explained above. So, by elimination, the offspring of both 8.6.4.7, and 6.4.7.8 is R_{67}, which is thus Disk 9.

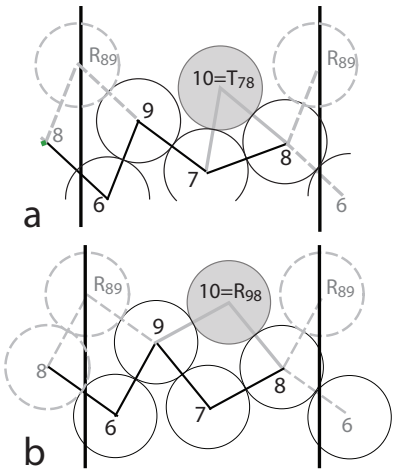

Disk 10: either R_{98} or T_{78}. The chain at 9 has the 2 notches 8.6.9 and 9.7.8. Since by rhombic transitions $\overrightarrow{69} = \overrightarrow{25}$ and $\overrightarrow{68} = \overrightarrow{24}$, $\angle 9.6.8 = \angle 5.2.4 \leq 2\pi/3$, as proven for Disk 6, and hence the offspring of 8.6.9 is R_{98}. As for the offspring of 8.7.9, we have two cases to consider depending on the sign of $\angle 8.7.9 - 2\pi/3$.

By Proposition 4.1, if $\angle 8.7.9 \leq 2\pi/3$, the offspring is R_{98} (see Figure b). If $\angle 8.7.9 > 2\pi/3$, $\left|\angle \overrightarrow{97}\right| \geq \angle \overrightarrow{78}$ since 9 is higher than 8, and thus T_{78} must be the offspring of notch 9.7.8. We now prove that whether it is R_{98} or T_{78}, the offspring of 9.7.8 is lower than the offspring R_{89} of 9.7.8. If T_{78} is the offspring of 9.7.8, then $\angle \overrightarrow{78} \in [0, \pi/6]$, since 7 is lower than 8 and the parents of T_{78} must be on opposite sides of it (and thus $\angle \overrightarrow{7T_{78}} \leq \pi/2$). This means that $\angle \overrightarrow{8T_{78}} \in [0, \pi/6] + 2\pi/3 = [2\pi/3, 5\pi/6]$. On the other hand R_{89} satisfies $\angle \overrightarrow{8R_{89}} = \angle \overrightarrow{25} = \beta_3 + \pi/3 \in [\pi/3, \pi/2]$. The properties of the sine function show that $\sin(\angle \overrightarrow{8T_{78}}) < \sin(\angle \overrightarrow{8R_{89}})$ and T_{78} is lower than R_{89}.

If R_{98} is the offspring of 9.7.8, then $\angle \overrightarrow{9R_{98}} = \angle \overrightarrow{78} \in [0, \pi/6]$ as we argued before. On the other hand, by rhombic transitions, $\overrightarrow{9R_{98}} = \overrightarrow{68} = \ldots = \overrightarrow{24} = \beta_2 + 2\pi/3 \in [2\pi/3, 5\pi/6]$, by Equation (13). Using the properties of sine, we find that R_{98} is lower than R_{89}. This finishes to prove that Disk 10 is either R_{89} if $\angle 8.7.9 \leq 2\pi/3$ or T_{78} if $\angle 8.7.9 > 2\pi/3$.

Disk 11 = R_{89}. We show, whether Disk 10 = R_{98} or T_{78}, that 11 = R_{89}.

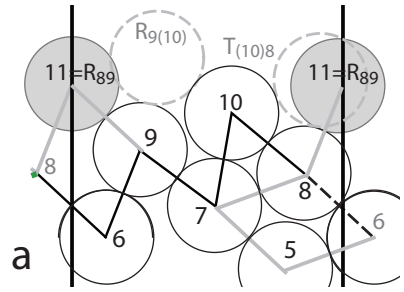

Case Disk 10 = T_{78} The chain at 10 is 8.6.9.7.10.8, with the 2 notches 10.8.6.9 and and 9.7.10. $R_{9(10)}$ is the offspring of 9.7.10: $\angle 10.7.9 < 2\pi/3$ since otherwise $\angle 8.7.9 \geq \pi$ and $\overrightarrow{97}$ would not be a down vector.

We now show that notch 10.8.6.9 can't have a pentagon offspring. Its first hinge angle $\angle 6.8.10 = \angle(\overrightarrow{86}, \overrightarrow{8(10)}) = \angle(\overrightarrow{75}, \overrightarrow{8(10)}) = \angle(\overrightarrow{75}, \overrightarrow{78}) + \angle(\overrightarrow{78}, \overrightarrow{8(10)}) \geq \pi/3 + 2\pi/3 = \pi$, where the first term comes from the non-overlap of 5 and 8. As for the second hinge angle, by no-overlap of 8 and 9, we have $\angle 9.6.8 \geq \pi/3$.

The sum of the hinge angles is therefore greater than $4\pi/3$ and the offspring is not a pentagon, by Proposition 4.3. As we have seen above $\angle 9.6.8 = \angle 5.2.4 \leq 2\pi/3$, therefore the possible offsprings for 10.8.6.9 are $T_{(10)8}$ and R_{89}. But the first one is ruled out since we know from the Disk 10 case that $\angle \overrightarrow{78} \leq \pi/6$ and thus $\angle \overrightarrow{T_{(10)8}8} = \angle \overrightarrow{78} - 2\pi/3 \in [-2\pi/3, -\pi/2]$. This in turn implies that $\overrightarrow{T_{(10)8}8}$ is not a down vector, which it should be for 8 to be the right parent of $T_{(10)8}$. Hence the offspring of 10.8.6.9 is R_{89}.

The difference of heights between R_{89} and $R_{9(10)}$ is

$$y(\overrightarrow{9R_{89}}) - y(\overrightarrow{9R_{9(10)}}) = y(\overrightarrow{68}) - y(\overrightarrow{7(10)}) = b(\sin(\angle \overrightarrow{68}) - \sin(\angle \overrightarrow{7(10)}).$$

By rhombic transitions, we have $\angle \overrightarrow{68} = \angle \overrightarrow{24} = \beta_2 + 2\pi/3 \geq 2\pi/3$. On the other hand, since $\angle 6.8.10 \geq \pi$ (see above), $\angle \overrightarrow{7(10)} = \angle \overrightarrow{8(10)} - \pi/3 \geq \angle \overrightarrow{68} - \pi/3 \geq \pi/3$. Since sin is an increasing function in $[\pi/3, \pi/2]$ $\sin(\angle \overrightarrow{68}) \leq \sin(\angle \overrightarrow{8(10)}$ and thus R_{98} must be the offspring in this case.

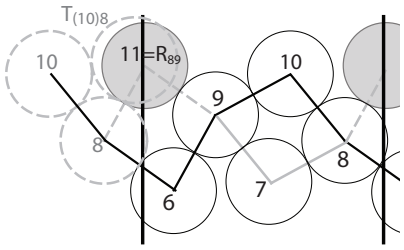

Case Disk 10 is R_{98}. In this case the resulting notch is the 2,2 notch 10.8.6.9.10. A hexagon transition with parents 10 and 10 is once again excluded because of the value of b in Region A. We have shown in the previous case that $\angle 9.6.8 \leq 2\pi/3$, ruling out triangle offsprings there. To rule out the pentagon offspring $P_{(10)9}$, we use Remark 4.1 and show that the hinge angle $\angle(\vec{69}, 8(\vec{10}) \geq \pi/3$. But that angle is equal to $\angle\overrightarrow{96} - \angle\overrightarrow{(10)8} = \angle 6.9.7$ which is indeed $\geq \pi/3$ since 6 and 7 do not overlap.
We can also easily dismiss $P_{8(10)}$ and R_{68} since in this case $\angle\overrightarrow{69} - \angle\overrightarrow{9(10)} = \angle\overrightarrow{47} - \angle\overrightarrow{78} > 0$ where the last inequality comes from our study of Disk 9.
Finally we rule out $T_{9(10)}$. Using Proposition 4.3 on notch 8.6.9.10 where

$$\beta_1 = \angle\overrightarrow{86} = \angle\overrightarrow{42} = \angle\overrightarrow{12} - \pi/3 \geq -\pi/3, \beta_3 = \angle\overrightarrow{9(10)} = \angle\overrightarrow{56} > \angle\overrightarrow{23} \geq 0,$$

we find that $\beta_1 + \beta_3 > -\pi/3$ ruling out the triangle $T_2 = T_{9(10)}$ for this notch.

□

Proposition 7.2. *A configuration starting with a chain in Region A, and with $\angle 564 \leq 2\pi/3$, becomes a 2,2-rhombic tiling starting at Disk 6. When $\angle 564 > 2\pi/3$, the chain 11.9.7.10.8.11 has the same angle properties (Equations 15) as chain 5.3.1.4.2.5 and thus undergoes the same transitions for another 4 iterations, after which it can either yield a rhombic tiling or undergo a triangle/pentagon transition. In all cases, the notch 11.9.7.8 is obtained from the chain 5.6.4.2 by a rotation by π about the midpoint of points 4 and 6 and translation by vector $\overrightarrow{47}$.*

Proof. This proof, like the previous one, relies heavily on Figure 24. If $\angle 5.6.4 \leq 2\pi/3$, then $\angle 8.7.9 = \angle 5.6.4 \leq 2\pi/3$, and $10 = R_{98}$, by Lemma 7.1. But then, since there are only rhombic transitions between them, Chain 10.8.6.9.10 is a translation of 6.4.2.5.6 by the vector $\overrightarrow{6(10)}$ and by symmetry, chains repeat every 4 iterates, translated by that same vector. Each chain (front) after 5.3.1.4.2.5 is (2, 2), so the configuration has become (2, 2)-rhombic tiling.

If $\angle 879 = \angle 564 > 2\pi/3$, Lemma 7.1 implies that $10 = T_{78}$. We now relate the angles of 11.9.7.10.8.11 to those of 5.3.1.4.2.5, and prove that they satisfy inequalities corresponding to those in Equations 15. Notice that the indices of points in chain 11.9.7.10.8.11 are obtained by adding 6 to those of 5.3.1.4.2.5.

By rhombic transitions, we have the equalities (shown by matching colors in Fig. 24):

$$\overrightarrow{(11)9} = \overrightarrow{42},\ \overrightarrow{8(11)} = \overrightarrow{25},\ \overrightarrow{78} = \overrightarrow{56},\ \overrightarrow{97} = \overrightarrow{64}. \tag{16}$$

Using these relationships we can now derive the analog to the Inequalities 15a:

$$0 \overset{1}{\leq} \angle\overrightarrow{8(11)} - \pi/3 \overset{2}{\leq} \angle\overrightarrow{7(10)} - \pi/3 \overset{3}{=} \angle\overrightarrow{(10)8} + \pi/3 \overset{4}{\leq} \left|\angle\overrightarrow{97}\right| \overset{5}{\leq} \pi/3.$$

Inequality 1 derives from $0 \leq \angle\overrightarrow{25} - \pi/3$ and $\overrightarrow{8(11)} = \overrightarrow{25}$.

For Inequality 2, since $\beta_3 \leq \beta_2$, we have $\angle\overrightarrow{8(11)} = \angle\overrightarrow{25} = \beta_3 + \pi/3 \leq \beta_2 + \pi/3 = \angle\overrightarrow{14}$. The Pentagon Lemma finishes the job since: $\angle\overrightarrow{14} \leq \angle\overrightarrow{56} + \pi/3 = \angle\overrightarrow{78} + \pi/3 = \angle\overrightarrow{7(10)}$.

Equality 3 is due to $\triangle 7.8.10$ being equilateral. Inequality 4 comes from the fact that Disk 9 is higher than Disk 8, and thus $\angle\overrightarrow{7(10)} - \pi/3 = \angle\overrightarrow{78} \leq \left|\angle\overrightarrow{97}\right|$. Inequality 5 derives from $\angle\overrightarrow{97} = \angle\overrightarrow{64} \geq \angle\overrightarrow{53}$ (Pentagon Lemma) and $\angle\overrightarrow{53} = \angle\overrightarrow{23} - \pi/3 \geq -\pi/3$.

The analog of Inequality 15b, namely $\angle\overrightarrow{8(11)} - \angle\overrightarrow{(11)9} \leq 2\pi/3$, holds since Disks 8 and 9 do not overlap.

Finally the analog of Inequality 15c, that is $\angle\overrightarrow{7(10)} - \angle\overrightarrow{(11)9} \geq 2\pi/3$ derives from:

$$\angle\overrightarrow{7(10)} - \angle\overrightarrow{(11)9} = \angle\overrightarrow{78} - \angle\overrightarrow{(11)9} + \pi/3 = \angle\overrightarrow{56} - \angle\overrightarrow{42} + \pi/3 = \angle\overrightarrow{56} - \angle\overrightarrow{41} + 2\pi/3 \geq 2\pi/3,$$

the last inequality coming from the Pentagon Lemma. Since the type and location of transitions in the orbit of the chain 5.3.1.4.2.5 derived entirely from Inequalities 15 in Lemma 7.1, the analog angle inequalities 11.9.7.10.8.11 ensure that it this chain undergoes the same types of transitions for 6 iterates.

As for the last statement of this proposition, note that only rhombic transitions occur between chains 5.6.4.2 and 11.9.7.8. The color coding in Figure 24 makes it clear that 5.6.4.2 and 11.9.7.8 are composed of the same three vectors, and that the rotation and translation proposed does transform the former chain into the latter. □

Proposition 7.2 can be seen as the first step of some kind of inductive statement: it says that if a 3, 2-chain, with points of same height order as 5.3.1.4.2.5 satisfies the same angle conditions as Equations 15, the pattern will evolve with the same sequence of transitions as those following 5.3.1.4.2.5. To make that statement more precise, we introduce a short-hand notation for chains. Given a chain of disks of the configuration $n_1 n_2 \dots n_N$ we denote:

$$n_1 n_2 \dots n_N \ (+K) := (n_1 + K)(n_2 + K)\dots(n_N + K).$$

We also use this notation for statements involving multiple chains. For instance, Equations 15 (+6k) means Equations 15 where all the disk indices involved have been translated by 6k. Note that, implicit in the notation $n_1 n_2 \dots n_N$ or $n_1 n_2 \dots n_N \ (+K)$ is the fact that these chains are chain of disks of the given configuration. In particular they are equilateral, with edge length equal to b.

Proposition 7.3. *If Chain* 5.3.1.4.2.5$(+6j)$ *satisfies Equations 15 (+6j) for all* $j \leq k$*, then if* $\angle 564\ (+6k) \leq 2\pi/3$ *the configuration becomes a rhombic tiling, or else, if* $\angle 564(+6k) > 2\pi/3$ *the chain yields in 6 iterates a chain* 5.3.1.4.2.5 $(+6(k+1))$ *which satisfies Equations 15 (+6(k+1)). In the latter case the process continues with a new pair of pentagon/triangle transition. In all cases, the chain* 5312 $(+6(k+1))$ *is obtained from the chain* 5.6.4.2 $(+6k)$ *by a rotation by* π *about the midpoint of points 4 and 6 (+6k) and translation by vector* $\overrightarrow{47}$ $(+6k)$.

Proof. Just re-index Proposition 7.2 and its proof by adding $(+6j)$ (or $(+6k)$) to every disk index. □

Remark 7.1. Note that, as a consequence of Proposition 7.3, if the orbit of a chain in Region A satisfies Equations 15 (+6j) for all $j \leq k$, it has exactly $k+2$ triangle transitions, and k pentagon transitions up to Disk $4 + 6k$ included. Conversely, if a configuration from Region A has $k+2$ triangle transitions up to Disk $4 + 6k$, Chain 5.3.1.4.2.5$(+6j)$ must be an equilateral chain of disks of the configuration and must satisfy Equations 15 (+6j) for all $j \leq k$.

7.1 The pentagon deformation map $\phi(\tau, \gamma)$ and its relation to $\mathcal{S}^6$.

Proposition 7.3 indicates that the dynamics in Region A may yield two types of behavior: the configuration becomes a rhombic tiling in a finite number of iterates or, *theoretically*, it may continue forever with pairs of triangle and pentagon transitions every 6 iterates. We now show that the second behavior does indeed occur, and we circumscribe the sub-region of Region A (*i.e.* the petal) where it does. We also show that, in some precise sense, the configuration approaches that of a rhombic tiling when it does not become one in finite time.

Assuming that, in the language of Proposition 7.3, Chain 5.3.1.2 $(+6k)$ satisfies Equations 15 (+6k), the key to our analysis is given by the geometric correspondence between Chains 5.3.1.2 $(+6k)$ and 5.3.1.2 $(+6(k+1))$ as mediated by the chain 5.6.4.2 $(+6k)$. Chain 5.3.1.2 $(+6k)$ lines the bottom of a triangle/pentagon pair. Chain 5.6.4.2 $(+6k)$ lines the top of the same pair, and (by rotation and translation)

has the same shape as Chain 5.3.1.2 ($+6(k+1)$) due in part to the fact that only rhombic transitions separate these two chains (see Figure 24). Therefore, to understand how the geometry of these chains evolves, we need to analyze how the relationship between the bottom and top chains of a triangle/pentagon pair. We do so by finding the map ϕ that relates the hinge angles (τ, γ) and (τ', γ') of these two chains.

Lemma 7.4. *In a convex equilateral hexagon, if two opposite sides are parallel, all opposite sides are parallel in pairs. If two opposite angles are equal, all opposite angles are equal in pairs.*

Proof. (See Figure 25 a). Let ABCJDPA be a convex equilateral hexagon and suppose the opposite sides $\overrightarrow{BC} = \overrightarrow{PD}$ are equal. Then $BCPD$ is a parallelogram, and $\overrightarrow{CD} = \overrightarrow{BP}$. The triangles $\triangle ABP$ and $\triangle JCD$ are isosceles and congruent. Convexity ensures that A lays in the half-plane bounded by line BP which contains no other point of the hexagon, and likewise for J and line CD. Since these two lines are parallel, $\triangle JCD$ is obtained from $\triangle ABP$ by a reflection about line BP and translation by $\overrightarrow{BC}$. This in turns implies that $\overrightarrow{AP} = \overrightarrow{CJ}$ and $\overrightarrow{AB} = \overrightarrow{DJ}$. Now assume that $\angle BAP = \angle CJD$ in the equilateral convex hexagon $ABCJDP$. Then $\overline{BP} = \overline{CD}$, and since $\overline{PD} = \overline{BC}$ the quadrilateral $BCDP$ is a parallelogram and $BC \parallel PD$. Applying the first part of the lemma, opposite sides are parallel, and thus opposite angles are equal. □

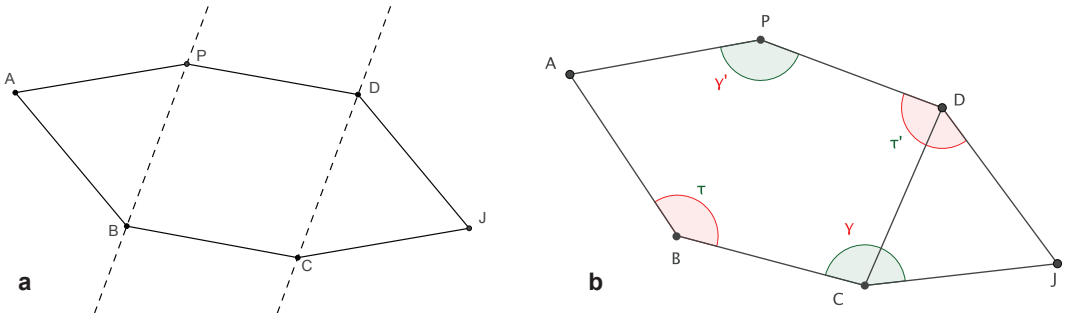

Figure 25: **a. Equilateral hexagon with parallel opposite sides (Lemma 7.4).** $BC \parallel PD$ implies that $AP \parallel CJ$ and $AB \parallel DJ$ in this equilateral, convex hexagon. **b. The map ϕ (Lemma 7.5).** The effect on hinge angles of a triangle/pentagon pair of transitions. Using the Pentagon Lemma, Lemma 7.5 shows that, in this picture τ' and γ' are determined by τ and γ and $\tau' \geq \tau$ and $\gamma' \leq \gamma$, with equality exactly when $\angle BAP = \angle DJC = \pi/3$. All chains are disk chains here.

Proposition 7.5. *Let ABCJDPA be a closed hexagonal, equilateral chain of disks where $\angle CJB = \pi/3$ and where we denote, as in Figure 25b, $\tau = \angle CBA, \tau' = \angle PDJ, \gamma = \angle JCB, \gamma' = \angle APD$. Then the pair (τ', γ') is uniquely determined by a map $(\tau', \gamma') = \phi(\tau, \gamma)$ (see formula in Proposition AD.1).*

The map ϕ has the properties:

1. *ϕ is differentiable and invertible.*
2. *$\tau' \geq \tau$ and $\gamma' \leq \gamma$, and these inequalities are strict if and only if no pair of opposite sides are parallel in the hexagon. In particular, the fixed points $(\tau, \gamma) = \phi(\tau, \gamma)$ of ϕ occur exactly when*

$$\overrightarrow{JD} = \overrightarrow{BA} \Leftrightarrow \overrightarrow{DP} = \overrightarrow{CB} \Leftrightarrow \overrightarrow{AP} = \overrightarrow{CJ} \Leftrightarrow \angle BAP = \pi/3 \Leftrightarrow \tau + \gamma = 5\pi/3$$

3. $\frac{\partial \gamma'}{\partial \gamma} > 0$.
4. *The quantity $I = \|AJ\|^2/b^2$ which, in terms of (τ, γ) is:*

$$I(\tau, \gamma) = (1 - \cos(\tau) - \cos(\gamma))^2 + (\sin(\tau) - \sin(\gamma))^2 = 3 - 2\cos(\tau) - 2\cos(\gamma) + 2\cos(\tau + \gamma),$$

is preserved by ϕ, in the sense that $I\mathbb{S}^1\phi(\tau, \gamma) = I(\tau, \gamma)$.

Proof. That (τ', γ') is uniquely determined by (τ, γ) can be seen geometrically: the shape of the chain $ABCD$ is uniquely determined by (τ, γ). In turn, the point P is determined as the only point (when it exists) such that $\triangle ADP$ is isosceles with $\overline{AP} = \overline{PD} = \overline{CD}$ and P lies in the open half plane bounded by line AD and that does not contain any of the points A, B, C, D and J. Given P, and the rest of the chain, the angles $\tau' = \angle APD, \gamma' = \angle PDJ$ which are independent of rotation and translation of the figure, are also uniquely determined. In a symmetric way, the angles (τ', γ') of the chain $APDJ$ determine (τ, γ), which shows that ϕ is invertible.

From the computation of ϕ, *i.e.* of $\tau'(\tau, \gamma), \gamma'(\tau, \gamma)$ in Appendix D, we see that these functions, as composition of trigonometric functions, are continuously differentiable and thus ϕ is differentiable.

We prove the other properties of ϕ geometrically. We refer to Figure 25 b. By the Pentagon Lemma 4.6, $\angle(\overrightarrow{CD}, \overrightarrow{BA}) \in [0, \pi/3]$. Hence

$$\angle(\overrightarrow{JD}, \overrightarrow{BA}) = \angle(\overrightarrow{JD}, \overrightarrow{CD}) + \angle(\overrightarrow{CD}, \overrightarrow{BA}) = -\pi/3 + \angle(\overrightarrow{CD}, \overrightarrow{BA}) \in [-\pi/3, 0].$$

This implies $\angle\overrightarrow{JD} \geq \angle\overrightarrow{BA}$. Likewise, the Pentagon Lemma shows that $\angle(\overrightarrow{DP}, \overrightarrow{CB}) \in [0, \pi/3]$, which implies $\angle\overrightarrow{DP} \leq \angle\overrightarrow{CB}$. As a result, we obtain:

$$\begin{aligned}\tau' = \angle PDJ &= \pi - \angle\overrightarrow{DP} + \angle\overrightarrow{JD} \\ &\geq \pi - \angle\overrightarrow{CB} + \angle\overrightarrow{BA} = \angle CBA = \tau,\end{aligned}$$

with the equality occurring exactly when $\overrightarrow{JD} = \overrightarrow{BA} \Leftrightarrow \overrightarrow{DP} = \overrightarrow{CB} \Leftrightarrow \overrightarrow{AP} = \overrightarrow{CJ}$ (see Lemma 7.4). Since $\angle DJC = \pi/3$, these equalities are also equivalent to $\angle BAP = \pi/3$. From the fact that $BCPD$ is then a parallelogram, and the triangles $\triangle ABP, \triangle CDJ$ are equilateral, one easily deduces that $\gamma + \tau = 5\pi/3$ (see Figure 25a).

As seen in Figure 25b, the role of the pair (γ', γ) is symmetric to that of (τ, τ') (in that order). The exact same proof thus shows $\gamma \geq \gamma'$, with equality occurring exactly when pairs of opposite sides of the hexagon are equal or, equivalently, $\angle BAP = \pi/3$. Hence the fixed points, which are such that $\tau' = \tau, \gamma' = \gamma$, occur exactly in the latter case.

As for the second property, it can be done using Calculus on the explicit formula for $\phi(\tau, \gamma)$. We prefer the following simple geometric proof. In Figure 25b, fix τ and increase γ. This increases $\overline{AD}$ which makes the isosceles triangle $\triangle APD$ flatter, *i.e.* forces γ' to increase.

To prove the third property, note that the chains ABCJ and APDJ of Figure 25b have same endpoints whose normalized distance squared $I = \|AJ\|^2/b^2$ can be computed by the same trigonometric formula (see Lemma D.2) using either of these two chains, *i.e.* either (τ, γ) or (τ', γ'). □

Correspondence between ϕ and $\mathcal{S}^6$ We can now apply Proposition 7.5 to spell out the correspondence between ϕ and the sixth iterate of $\mathcal{S}$ on the chains 5.3.1.4.2.5 $(+6k)$. Theses chain (up to translation) have the bearing angles (see Figure 26):

$$(\rho, \rho + (\pi - \tau), \rho + (\pi - \tau) + (\pi - \gamma) + \pi/3, \rho + (\pi - \tau) + (\pi - \gamma) - 2\pi/3, \alpha),$$

where, as in the previous section, we use the hinge angles notation $\tau = \angle 135\ (+6k), \gamma = \angle 213\ (+6k)$. The last bearing angle $\alpha = \angle\overrightarrow{25}\ (+6k)$ is constant under $\mathcal{S}^6$, and is determined by the initial value of (τ, γ). In other words, 5.3.1.4.2.5 $(+6k)$ can be parametrized by (τ, γ, α) and, from Propositions 7.3 and 7.5, the map $\mathcal{S}^6$ on these chains and in these coordinates is given by

$$\mathcal{S}^6((\tau, \gamma), \alpha) = (\phi(\tau, \gamma), \alpha). \tag{17}$$

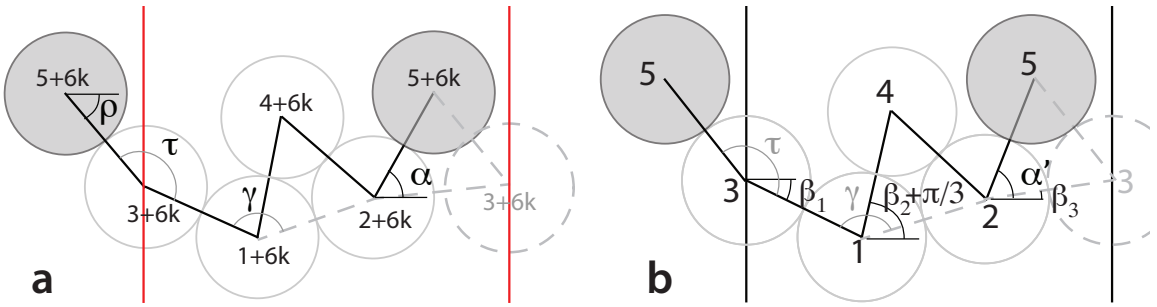

Figure 26: **a.** Chain $5.3.1.4.2.5+6k$ from an orbit of a chain in region A. **b.** The projection of the chain in **a.** into C_3. The angles τ,γ remain the same, but α and b usually change. The correspondence between the parametrizations by (τ,γ,α') and $(\beta_1,\beta_2,\beta_3)$.

7.2 Partition of Region A into finite and infinite convergence

To explain the distinct convergence behaviors in Region A, we use another change of coordinates which project chains $5.3.1.4.2.5\ (+6k)$ into C_3, see Figure 26. In general Disks $2+6k$ and $3+6k$ are not tangent. By rescaling $3.1.4.2\ (+6k)$ together with the diameter b of the disks until $2+6k$ and $3+6k$ are tangent, keeping $5+6k$ as their child, we obtain a chain $5.3.1.4.2.5$ such that $3.1.2.3$ is in C_3. Since rescaling does not change hinge angles, this new chain has angle (τ,γ,α'). For this new chain, the bearing angles $(\beta_1,\beta_2,\beta_3)$ of $3.1.2.3$ and the coordinates (τ,γ,α') can be readily checked on Figure 26b:

$$(\tau,\gamma,\alpha')=\left(\frac{2\pi}{3}+\beta_3-\beta_1,\pi+\beta_1-\beta_2,\beta_3+\frac{\pi}{3}\right)\Leftrightarrow(\beta_1,\beta_2,\beta_3)=\left(\alpha'-\tau+\frac{\pi}{3},\alpha'-\gamma-\tau+\frac{4\pi}{3},\alpha'-\frac{\pi}{3}\right)\qquad(18)$$

When projected down from C_3 to its tangent plane $\beta_1+\beta_2+\beta_3=0$, in the coordinates (x,y) from the orthonormal basis

$$\vec{v}_1=\begin{pmatrix}-\frac{1}{\sqrt{2}}\\ \frac{1}{\sqrt{2}}\\ 0\end{pmatrix},\qquad \vec{v}_2=\begin{pmatrix}-\frac{1}{\sqrt{6}}\\ -\frac{1}{\sqrt{6}}\\ \sqrt{\frac{2}{3}}\end{pmatrix},$$

we obtain (taking the dot product with $\vec{v}_1$ and $\vec{v}_2$ respectively) the change of variables :

$$(x,y)=\left(\frac{\pi-\gamma}{\sqrt{2}},\frac{3\gamma+6\tau-7\pi}{3\sqrt{6}}\right)\Leftrightarrow(\tau,\gamma)=\left(\frac{x+\sqrt{3}y}{\sqrt{2}}+\frac{2\pi}{3},\pi-\sqrt{2}x\right)\qquad(19)$$

Note that α' has disappeared in the process, and that (τ,γ) can be used to parametrize Region A, which can in turn be used to vizualize the dynamics of ϕ and, therefore $\mathcal{S}^6$. The boundaries of Region A are (see Figures 21, 27), in the two sets of coordinates:

$$\beta_3=0\Leftrightarrow 3\gamma+6\tau-7\pi=0\Leftrightarrow y=0\qquad\text{(bottom)}$$
$$\beta_2-\beta_3=0\Leftrightarrow\tau+\gamma=5\pi/3\Leftrightarrow y=x/\sqrt{3}\qquad\text{(top)}$$
$$\beta_2-\beta_1=\pi/3\Leftrightarrow\gamma=2\pi/3\Leftrightarrow x=\frac{1}{3\sqrt{2}}\qquad\text{(right)}$$

From which we obtain the coordinates of the vertices of the triangular region A:

$$\left\{(0,0),\left(\pi/3\sqrt{2},0\right),\left(\pi/3\sqrt{2},\pi/3\sqrt{6}\right)\right\}$$

in the (x,y) coordinates and $\{(2\pi/3,\pi),(5\pi/6,2\pi/3),(\pi,2\pi/3)\}$ in the (τ,γ) coordinates. Note that the equation $\tau+\gamma=5\pi/3$ of the top boundary confirms that it corresponds to the limit of existence of the pentagon 5.3.1.4.6.5, as the sum of the hinge angles of 5.3.1.4, $\angle 135+\angle 413=\tau+\gamma-\pi/3=4\pi/3$. Proposition 7.5 also shows that these chains correspond to fixed points of ϕ. Likewise, the right boundary, where $\angle 213=\gamma=2\pi/3$, is the limit of existence of the triangle $\triangle 124$.

The functions I and ϕ in Region A The change of coordinates above allows us to express the functions ϕ and I in the variables x and y. The connection between ϕ and $\mathcal{S}^6$ disappears for points outside of Region A: above it, the corresponding chain 5.3.1.4.2.5 cannot produce a pentagon, to the right, 3.1.2.3 cannot produce a triangle, and below, the chain 3.1.2.3 is not a 1, 2-chain anymore but a 2, 1-chain. Figure 27A and B show the isolines of I in Region A, in the coordinates (τ,γ) and (x,y) respectively. The arrows and dots in B indicate the direction of the dynamics under ϕ, a.k.a. $\mathcal{S}^6$.

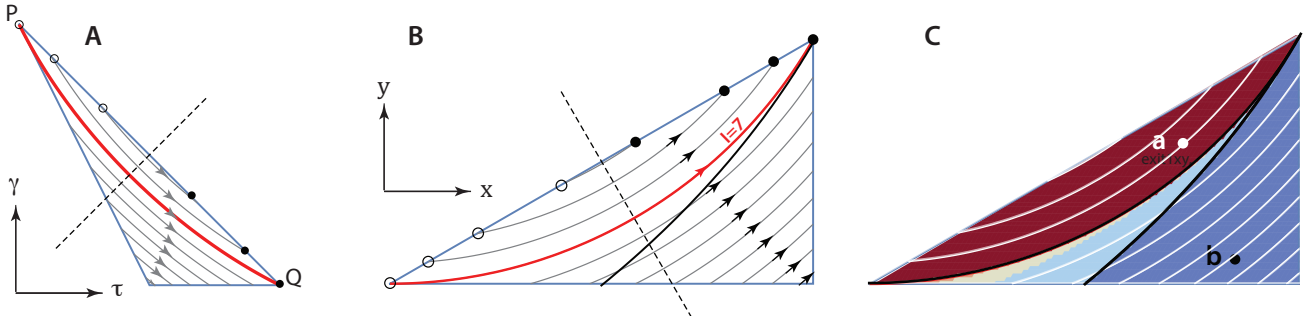

Figure 27: **A.** The isolines of $I(\tau,\gamma)$ in Region A represented in the (τ,γ)-plane. The line of symmetry (dashed) $\tau=\gamma$ is the perpendicular bisector of the top boundary. The isoline $I=7$ is marked in red. **B.** The isolines of $I(x,y)$ in Region A, with the (x,y) coordinates. The perpendicular bisector of the top boundary remains the line of symmetry. The arrows indicate the direction that $\mathcal{S}^6$ maps points on the isolines. Each point in the top boundary is a fixed point. The points represented by empty circles repel points in the interior of Region A, the points with filled circles attract them. The isoline $I=7$ (in red) partitions Region A into 2 regions: in the top one, points take infinitely many iterations to converge to a fixed point; in the bottom region, points exit Region A in finite time. The black line represents the pre-image by $\mathcal{S}^6$ of the boundary $x=\pi/(3\sqrt{2})$. **C.** The isolines are superimposed onto the the numerical sweep of Figure 3, where the redder the point, the more pairs of triangles and pentagons its orbit contains. The petal like red region discovered numerically has boundary the isoline $I=7$, confirming that it contains chains that converge to rhombic tilings in infinite time. The coloring of the region below the petal, with the darker blue region exiting Region A in one iterate, is also consistent with the dynamics of $\mathcal{S}^6$.

Theorem 2. *The isoline $\phi=7$ splits Region A in two subregions. The top one, (coinciding with half a red petal in Figure 3), corresponds to chains converging, under infinitely many iterations of $\mathcal{S}$, to 2,3-rhombic tilings . The bottom subregion corresponds to chains that become in finite time chains of 2,2-rhombic tilings.*

Proof. For simplicity, we use the (τ,γ) coordinates. The points $P=(2\pi/3,\pi)$ and $Q=(\pi,2\pi/3)$ are the top and right vertices of Region A in those coordinates. Substitution in $I(\tau,\gamma)=3-2\cos(\tau)-2\cos(\gamma)+2\cos(\tau+\gamma)$ yields $I(P)=I(Q)=7$. That these values are the same is no surprise as the function I is clearly invariant under the reflexion $(\tau,\gamma)\to(\gamma,\tau)$ about the line $\tau=\gamma$. [8]

We show that the isoline $I=7$ restricted to Region A forms one single curve connecting P and Q and projecting 1 to 1 on the boundary segment PQ.

We first show that, on the boundary of Region A, $I=7$ only occurs at P and Q. The segment PQ affords the parametrization $(\tau,5\pi/3-\tau),\tau\in[2\pi/3,\pi]$. Restricting I to PQ yields $I(\tau,5\pi/3-\tau)=4-3\cos(\tau)+\sqrt{3}\sin(\tau)$. Calculus and trigonometry show that this function is symmetric about the midpoint $5\pi/6$ of the interval $[2\pi/3,\pi]$, it increases on the first half of the interval to a maximum of $2(1+\sqrt{2})$ and

[8] Under the affine change of coordinates to (x,y), the reflection becomes the one about the line $y=-\sqrt{3}x+\sqrt{2/27}\pi$, which is also the perpendicular bisector of the top boundary in these coordinates. I is also invariant under this reflection in those coordinates, as is clear in Figure 27B

decreases on the second half. In particular, the minimum is attained exactly at $\tau = 2\pi/3$ and π (*i.e.* at P and Q), at which we know $I = 7$. Thus P, Q are the only elements of $I = 7$ on the boundary segment PQ. Likewise, the restriction of I on the left boundary is $I(\tau, 7\pi/3 - 2\tau) = \sqrt{3}\sin(\tau) - \sqrt{3}\sin(2\tau) - \cos(\tau) - \cos(2\tau) + 3, \tau \in [2\pi/3, 5\pi/6]$, which has a unique maximum 7 at $\tau = 2\pi/3$, *i.e.* at P. Finally, on the lower boundary $I(\tau, 2\pi/3) = -\sqrt{3}\sin(\tau) - 3\cos(\tau) + 4, \tau \in [5\pi/6, \pi]$ which has maximum 7 at (only) π, *i.e.* at Q.

We now show that *all* isolines of I restricted to Region A project injectively on PQ, by showing that they are all transverse to the lines of slope 1, which are perpendicular to PQ. We do so by computing the minimum of the directional derivative $\nabla_{\overrightarrow{d}} I(\tau, \gamma) = 2\sin(\tau) + 2\sin(\gamma) - 4\sin(\tau + \gamma)$ in Region A, where $\overrightarrow{d} = (1, 1)$. The Lagrange multiplier method (or a computer algebra software) shows that the minimum of $2\sqrt{3}$ for this derivative function is attained at P and Q. That this minimum is greater than 0, has three consequence: 1) there are no critical points for I in Region A; 2) no isoline has tangent vector $(1, 1)$ in Region A; 3) These isolines project injectively to the top boundary PQ. Note also that each isoline is compact, as a pre-image in the compact Region A of a singleton, under the continuous I.

We now show that $I = 7$ has a unique connected component, which therefore mus connect P and Q. By continuity, the set $\{I = 7\} \cap A$ is closed and bounded, and hence compact, and the same holds for its connected components. By continuity, the orthogonal projection of the connected component of P in $I = 7$ on PQ is compact, and attains a minimum in height, say M. We must have $M \neq Q$, since no point of Region A projects on Q other than Q itself. The unique point of $I = 7$ in Region A that projects onto M is either on the boundary, tangent to the perpendicular to PQ, or a critical points - all three possibilities have been ruled out above. The same reasoning, looking at the highest point of the projected component proves that P belongs to the component. Hence the isoline $I = 7$ connects P and Q within Region A, and splits the region in two sub-regions. Since $\nabla_{\overrightarrow{d}} I(\tau, \gamma) = 2\sqrt{3} > 0$, $I > 7$ above $I = 7$ and $I < 7$ below.

The same proof that we used for $I = 7$ can be used to show that the isoline $I = s$ for $s \in [7, 2(1 + \sqrt{2}))$ is a curve that connects two points P_s and Q_s on PQ, symmetrically located on opposite sides of its midpoint. The region enclosed by $I = 7$ and PQ is thus foliated by these isolines, and we now claim that points inside that region correspond to chains of $\mathcal{K}_{12}$ that converge in infinite time to 2,3-rhombic tilings. Since they are on PQ, the points P_s and Q_s are fixed points. A point M_s of coordinates (τ, γ) on $I = s$ and in the interior of Region A will have iterate $(\tau', \gamma') = \phi(\tau, \gamma)$ where $\tau' > \tau$ and $\gamma' < \gamma$ according to Proposition 7.5. Hence points travel down and right along the curve $I = s$, under ϕ (a.k.a $\mathcal{S}^6$). Moreover, according to the same proposition, since $\frac{\partial \gamma'}{\partial \gamma} > 0$, and since $\gamma(P_s) < \gamma(M_s) < \gamma(Q_s)$, $\phi(M_s)$ must remain between P_s and Q_s on $I = s$. Since $\gamma' \leq \gamma$, the sequence $\gamma(\phi^n(M_s))$ is decreasing and bounded. It must converge to a point where $\gamma' = \gamma$, *i.e.* a fixed point which can only be $\gamma(Q_s)$. Thus $\lim_{n\to\infty} \phi^n(M_s) = Q_s$.

This convergence can't occur in finite time: if $\phi^n(M_s) = Q_s$ for some $n \in \mathbb{N}$, replacing M_s by its iterate $\phi^{(n-1)}(M_s)$, we get $\phi(M_s) = Q_s$. But, since $\frac{\partial \gamma'}{\partial \gamma} \geq 0$ (with equality only at fixed points) any point in the segment

$$\{R \in \{I = s\} \mid \gamma(M_s) \leq \gamma(R) \leq \gamma(Q_s)\}$$

must then be mapped to Q_s by ϕ. But this is impossible since ϕ is invertible.

To see that the orbit of Q_s can be interpreted as a 3,2 rhombic tiling, note that, since $\beta_2 = \beta_3$ for these chains, we have $\overrightarrow{14} = \overrightarrow{25}$ (see Figure 28). As is characteristic of fixed points of ϕ (see Proposition 7.5), the quadrilateral 1463 is a rhombus, so we also have $\overrightarrow{14} = \overrightarrow{36}$ and $\overrightarrow{31} = \overrightarrow{64}$. As a result, Disks 4, 5 and 6 form a lign of tangent disks, *i.e.* $\overrightarrow{45} = \overrightarrow{56} = \overrightarrow{12} = \overrightarrow{23}$. In other words, Chain 6456 is Chain 3.1.2.3 translated by $\overrightarrow{14}$, and the pattern is periodic of period 3. The same kind of reasoning implies that the quadrilaterals 2.5.7.4.2 and 3.6.8.5.3 are rhombi and the 3,2-Chain 6.4.2.5.3.6 can be seen as a chain generating a 2, 3-rhombic tiling, of period 6, but reducible to period 3 in this case, since the up vectors are identical, and so is a pair of down vectors ($\overrightarrow{42} = \overrightarrow{53}$).

We now prove that points on $I = s, s < 7$ must converge to 2,2 rhombic tilings in finite time. Since the compact isoline $I = s$ is separated from PQ by $I = 7$, there are no fixed points for ϕ on $I = s$. Hence

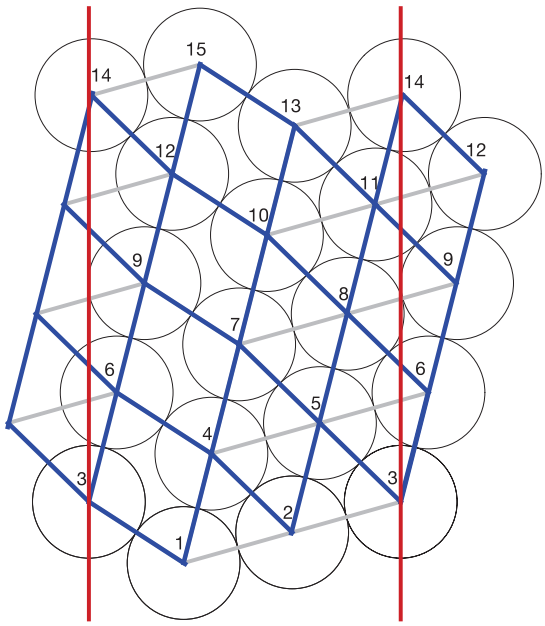

Figure 28: **Fixed points of the map $\mathcal{S}^6$.** A configuration to which the chains in isoline $I = 7.283$ converge. This configuration can be seen as a 2,3-rhombic tiling (blue edges, superimposed to the dynamically defined gray edges), which are generally of period 6. It is also of period 3 here: because of triple tangencies, it has a pair of equal down vectors, and its two up vectors are the same. Some of its transitions can also be seen as triangle (e.g. at 7 or 8) and pentagons (e.g. at 9 or 12). Note the line-slip structure [21] of 3 interlocked, straight and parallel up-parastichies, a characteristic feature of these fixed points.

function $= \gamma(\phi(\tau,\gamma)) - \gamma = \gamma'(\tau,\gamma) - \gamma < 0$ on $I = s$ and must attain a strictly poisitve lower bound. Given any point M_s of $I = s$, Since $\gamma(M_s) \in [2\pi/3, \pi]$, there exists a positive integer n for which $\gamma(\phi^n(M_s)) < 2\pi/3$ and $\gamma(\phi^{(n-1)}(M_s)) \geq 2\pi/3$. The point $\phi^n(M_s)$ corresponds to a chain 5.3.1.4.2.5(+6n) where $\gamma' = \angle 5.6.4(+6n) = \angle 8.7.9(+6n) < 2\pi/3$, which must yield a rhombic transition $10(+6n) = R_{98}(+6n)$ and a 2,2 rhombic tiling chain 10.8.6.9.10(+6n), as seen in Figure 24B of Proposition 7.3. □

8 Concluding remarks

Summary of the different assymptotic dynamics. We have rigorously confirmed the classification of Figure 3. Namely, we have shown that the disk stacking map $\mathcal{S}$ when iterated with initial conditions within the petals inside the inner hexagon of C_3 converge in *infinite time* to 3,2 of 2,3 rhombic tilings that are lattices with a line slip. The axes of the petals are made of these rhombic tilings, and are period 3 orbits for $\mathcal{S}$. The orbits of chains in the inner hexagon, but outside the petals converge in *finite time* to 2,2 rhombic tilings. The orbit of chains outside the inner hexagon, in the rays of the star of David, are Bernhardt tilings, which can be interpreted as 2,2 rhombic tilings with some extra triple tangencies. Chains in the regions outside the inner hex and the star of David's ray are 1,2 or 2,1 rhombic tilings, with the particular case, on the axes of C_3 joining the center to the vertices, where the chains yield rhombic lattices that are fixed points of $\mathcal{S}$. These results put together finish the proof of Theorem 1: all chains from C_3 have their orbits converging to rhombic tilings.

From the rhombic lattices to the rhombic tilings paradigm in phyllotaxis. Rhombic lattices are the descriptive model central to much of the theoretical work on phyllotaxis, starting with the seminal work by the Bravais in 1837 ([16], [33], [11], [17], [27], [23]). van Iterson used rhombic lattices as the back bone of the route to the golden angle divergence through Fibonacci transitions. This route is splendidly

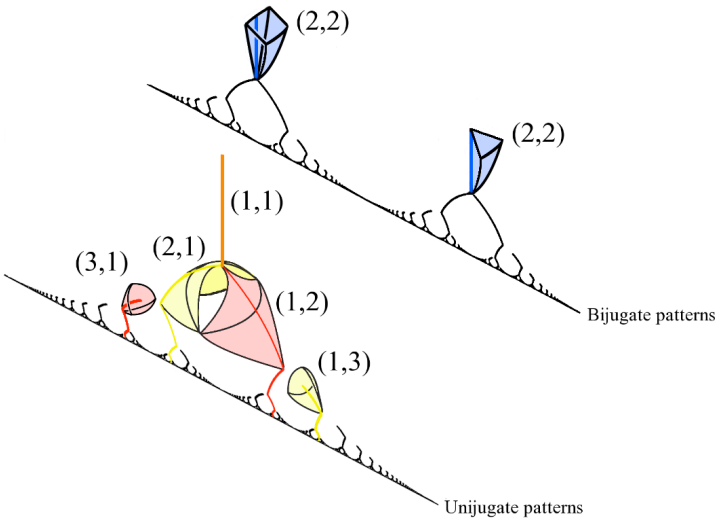

Figure 29: **Partial rendition of the attractor (courtesy Scott Hotton).** The black lines correspond to the van Iterson diagram, representing rhombic lattices. The vertical axis corresponds to the radius of the disks in a chain. Starting with a 1,1 chain (on the orange vertical line) and decreasing the radius, a chain goes down, hugging the attractor, branching out to the successive Fibonacci branches. The surfaces and solids around the diagram are a rendition of the chains of appropriate lengths. Rhombic tilings are subsets of these sets of chains.

illustrated by the van Iterson diagram, which is the locus of rhombic lattices in the parameter space of their generators $z = \alpha + iy$ (where $\alpha \in \mathbb{S}^1$ is the divergence angle, $y \in \mathbb{R}^+$ is the plastochrone), unrolled in the upper half plane. According to van Iterson, who was also using the disk stacking model, as the disk diameter b decreases, the structure would stabilize from (square) lattice with Fibonacci parastichy numbers to one with the next pair of Fibonacci numbers. This kind of approach, but with different models, was taken on, numerically by [29, 30], analytically by [18, 23] where a set of lattices close (or equal in [23]) to rhombic lattices, are indeed attractors, and meander down to the golden angle. Unfortunately, in the disk stacking model, rhombic lattices are not attractors. This can easily be seen from the results of this paper: take a fixed point lattice in C_3, *e.g.* one with $\beta_2 = \beta_3$ and $\tau < 2\pi/3$. It lives on the blue portion of C_3, on the axes of the hexagon. But it is surrounded by 1,2 rhombic tilings that are periodic orbits. So the least perturbation of the lattice making β_3 slightly different from β_2, yields a 1,2 rhombic tilings, whose orbit, while staying close to that of the lattice, never converges back to it: the lattice is *neutrally stable* but not *asymptotically* so. However, if Conjecture 1 is generally true, the set of rhombic tilings *is* a global attractor and therefore nearby orbits with sufficiently slowly varying b will remain in the vicinity of that attractor. One then needs to argue that the different branches of m,n rhombic tilings fit together in a way that, starting with Fibonacci pair m,n, one is channeled by the attracting set of rhombic tilings through the Fibonacci sequence. Although this not impossible to imagine, the technicalities involved in using this as the structure of a rigorous proof raises enormous technical difficulties: the same way that the set of 1,2 rhombic tilings (with varying b) is 2-dimensional, the set of m,n rhombic tilings is (m+n-1)-dimensional. Understanding the topology of these sets, and how they fit together can be a daunting task. Indeed, classifying the topology of cylindrical disk chains can be daunting, even for shorter chains. As an intriguing example, the set 4-chains of fixed diameter b, for $b \in [1/4, 1/2]$ has the topology of a projective plane ([22]).

A more local approach, using fronts and their transitions as b varies, seems to capture the Fibonacci transition process in a much more concrete way [12] that seems more promising for a rigorous proof of Fibonacci transitions in the disk stacking process with slowly varying b.[9]

[9]This approach is not too dissimilar to van Iterson's use of fragments of transitioning configurations and his brilliant introduction of a renormalization argument, many decades before any such thing was formally introduced in Nobel prize level

Concluding words We wish this paper demonstrates that the field of phyllotaxis, or plants patterns, is still rich of potential mathematical discoveries. In this particular case we have shown that even though geometrically packed discs on a cylinder seem to form rigid configurations, there is a richness of dynamics in the stacking process to allow the system to converge toward a periodic structure in either finite and infinite time. This shows the inherent stability of such patterns.

We hope to have established enough of the elementary tools and vocabulary to help other researchers understand disk pilings in a different, more dynamical way, that could be useful in other contexts than phyllotaxis.

A Classification of 3-notches: proof of Lemma 4.2.

We remind the reader that this lemma states the conditions that partition the shape space of 3-chains in terms of their possible offsprings. We now give the proof of the lemma, repeated each of the statement as we proceed. The reader is urged to visualize the situations described by using this online, interactive version of Figure 4.2, https://ggbm.at/prevpdfk (a Geogebra applet).

Proof. As usual, we denote by b the length of the edges of the chain of disks.

(i) $\tau \in [\pi/3, 5\pi/3],\ \gamma \in [\pi/3, 5\pi/3],\ \tau + \gamma \geq \pi$

Remember that, in a chain of disks, no two points overlap. The condition $\tau \in [\pi/3, 5\pi/3]$ (*resp.* $\gamma \in [\pi/3, 5\pi/3]$) is a direct consequence of the non-overlap of A and C (*resp.* B and D). Likewise, $\tau + \gamma \geq \pi$ is equivalent to the non-overlap of A and D: a lesser sum of angles would mean that the distance between A and D would be less than b. Indeed, the rays obtained by continuing vectors $\overrightarrow{BA}$ and $\overrightarrow{CD}$ must intersect at some point I, where $A \in BI, D \in IB$. Now use the law of cosine for the triangles $\triangle IBC$ and $\triangle IAD$ and their common angle at I to conclude that $\tau + \gamma < \pi \Rightarrow \overline{AD} < \overline{BC} = b$.

(ii) $\tau + \gamma = 4\pi/3 \Leftrightarrow R_1 = T_2 \Leftrightarrow R_2 = T_0 \Leftrightarrow P$ and P' exist and $\{T_0, T_2\} = \{P, P'\}$

(boundary between the yellow and blue regions in Figure 4.2). If $R_1 = T_2$, $\angle R_1CB = \gamma - \pi/3$. This angle is also adjacent to $\angle CBA = \tau$ in the rhombus $ABCR_1$ and thus $\pi - \tau = \gamma - \pi/3$ or, equivalently, $\tau + \gamma = 4\pi/3$. Conversely, if $\tau + \gamma = 4\pi/3$ then $\angle R_1CB = \pi - \tau = \gamma - \pi/3$, which means $\angle DCR_1 = \pi/3$ and $R_1 = T_2$. The same reasoning shows $R_2 = T_0 \Leftrightarrow \tau + \gamma = 4\pi/3$. By transitivity, $R_2 = T_0 \Leftrightarrow R_1 = T_2$.

For the last equivalence note that, since $R_1 \in C_A \cap C_C$ and $T_2 \in C_C \cap C_D$, $R_1 = T_2$ implies that $T_2 \in C_A \cap C_D = \{P, P'\}$. In particular P, P' exist in this case. At the same time, we must have $R_2 = T_0$ which implies $T_0 \in C_D \cap C_A = \{P, P'\}$ so the we must have $\{T_0, T_2\} = \{P, P'\}$ (as sets) whenever one of these equalities occur. Conversely, if $P = T_0$, then $\overline{PB} = \overline{T_0B} = b$ and the quadrilateral $DPBC$ is equilateral, hence a rhombus. This implies $P = R_2$ and hence $T_0 = R_2$. The same proof shows that when $P = T_2$, then $T_2 = R_1$.

(iii) $\tau + \gamma < 4\pi/3 \Leftrightarrow R_1$ overlaps with $D \Leftrightarrow T_2$ overlaps with $A \Leftrightarrow R_2$ overlaps with $A \Leftrightarrow T_0$ overlaps with D. (Yellow region, Figure 4.2P).

Note that $\overrightarrow{BR_2} = \overrightarrow{CD}$ (as opposite sides of rhombus $BCDR_2$) and $\angle(\overrightarrow{BA}, \overrightarrow{BT_0}) = \pi/3$ ($\triangle ABT_0$ is equilateral). Note also that

$$\tau + \gamma - \pi = \angle(\overrightarrow{BA}, \overrightarrow{CD}),$$

as can be checked by using the relationship between bearing and hinge angles (Equation 1). Using the fact that $\overrightarrow{CD} = \overrightarrow{BR_2}$,

$$\angle R_2BT_0 = \angle R_2BA - \angle T_0BA = \angle(\overrightarrow{BA}, \overrightarrow{CD}) - \angle T_0BA = \tau + \gamma - 4\pi/3,$$

and $\tau + \gamma < 4\pi/3 \Leftrightarrow \angle R_2BT_0 < 0$. But this is equivalent to R_2 being in the arc $\overset{\frown}{T_0A}$ of C_B, which is inside D_A, which is itself equivalent to R_2 overlapping with A. Likewise $\angle R_2BT_0 < 0$ is equivalent to $T_0 \in \overset{\frown}{R_2D} \subset D_B$, that is, T_0 overlaps with D. The proofs of the next two equivalences are identical.

physics and math!

(iv) $\tau + \gamma \leq 4\pi/3 \Leftrightarrow$ *P exists and does not overlap with any point in the chain* (Again: yellow region, Figure 4.2P).
The reader should brace themselves: this is by far the most involved case. As seen in (ii) and (iii) above, $\gamma + \tau \leq \frac{4\pi}{3} \Leftrightarrow T_0 = R_2$ or T_0 overlaps with D. In either case, since $T_0 \in C_A, R_2 \in C_D$ this implies $C_A \cap C_D \neq \emptyset$ and P, P' exist. P overlaps with B exactly when $\angle BAP < \pi/3$, and P overlaps with C exactly when $\angle PDC < \pi/3$. So we want to show the opposite inequalities hold when $\gamma + \tau \leq \frac{4\pi}{3}$. Note that, when P and P' exist, the measures of the angles $\angle BAP$ and $\angle PDC$ are continuous functions of the variables τ and γ. This can be seen by using simple trigonometry. Accordingly, the function

$$m(\tau, \gamma) = \min(\angle BAP(\tau, \gamma), \angle PDC(\tau, \gamma)) - \pi/3$$

is also a continuous function of (τ, γ), which is strictly negative exactly when P overlaps one of B or C, positive otherwise. We claim that m is 0 on the line (see Figure 4.2)

$$\mathcal{L} = \{(\tau, \gamma) \mid \tau + \gamma = 4\pi/3\},$$

and m is strictly positive below, and strictly negative above, which will prove our claim. By (ii), we know that $\mathcal{L}$ is the locus of chains for which $P = T_0$ ($\Leftrightarrow \angle BAP = \pi/3$) or $P = T_2$ ($\Leftrightarrow \angle PDC = \pi/3$). To prove that $m = 0$ on $\mathcal{L}$, we show that, on $\mathcal{L}$, $\angle BAP > \pi/3$ whenever $\angle PDC = \pi/3$, and vice versa, so $\min(\angle BAP(\tau, \gamma), \angle PDC(\tau, \gamma)) = \pi/3$, and $m = 0$ there.

Take $(\tau, \gamma) \in \mathcal{L}$ and assume without loss of generality that $\tau \leq \gamma$. Since $\tau + \gamma = 4\pi/3$, we must have $\tau \leq 2\pi/3$ and thus

$$\angle CBT_0 = \angle CBA - \angle T_0BA = \tau - \pi/3 \leq \pi/3.$$

Since $T_0 = R_2$ on $\mathcal{L}$, $\angle CBT_0 = \angle T_0DC$ as these angles are opposite in the rhombus $BCDT_0$. So $\angle T_0DC \leq \pi/3 = \angle T_2DC$ and, since $\{P, P'\} = \{T_0, T_2\}$ on $\mathcal{L}$, we must have $T_0 = P'$ and $T_2 = P$ (when equality holds these three points coincide). The same reasoning shows that $T_0 = P$ and $T_2 = P'$ when $\tau \geq \gamma$. Now assume $\angle PDC = \pi/3$. This implies $P = T_2 = R_1$ and thus, as we just proved, $\tau \leq 2\pi/3 \leq \gamma$. We have $\angle BAP = \angle PCB$ as they are opposite angles in the rhombus $ABCP = ABCR_1$ and thus, on $\mathcal{L}$,

$$\angle BAP = \angle PCB = \angle DCB - \angle DCP = \gamma - \pi/3 \geq 2\pi/3 - \pi/3 = \pi/3.$$

So $\angle PDC = \pi/3 \Rightarrow \angle BAP \geq \pi/3$. The same proof would show $\angle BAP = \pi/3 \Rightarrow \angle PDC \geq \pi/3$. This finishes showing that $m(\tau, \gamma) = 0$ on $\mathcal{L}$. Conversely, if $m(\tau, \gamma) = 0$, then either $\angle BAP = \pi/3$ or $\angle PDC = \pi/3$. But $\angle BAP = \pi/3$ implies that $\triangle BAP$ is equilateral, *i.e.* $P = T_0$, and consequently $P' = T_2$. Using (ii), we get that $\tau + \gamma = 4\pi/3$, and we're on $\mathcal{L}$.

We now show that m is strictly greater than 0 below $\mathcal{L}$ and, where it is defined, it is strictly less than 0 above $\mathcal{L}$. The function m is defined wherever P is, which is whenever $\overline{AD} \leq 2b$. Simple trigonometry shows that

$$\begin{aligned}\overline{AD}^2 &= b^2\left[(1 - \cos(\tau) - \cos(\gamma))^2 + (\sin(\tau) - \sin(\gamma))^2\right] \\ &= b^2(3 - 2\cos(\tau) - 2\cos(\gamma) + 2\cos(\tau + \gamma)),\end{aligned}$$

and hence, $\overline{AD} \leq 2b \Leftrightarrow \overline{AD}^2 \leq 4b^2 \Leftrightarrow -1 - 2\cos(\tau) - 2\cos(\gamma) + 2\cos(\tau + \gamma) \leq 0$. The boundary of the region of existence of P is thus the 0-isoline of the function

$$p(\tau, \gamma) = -1 - 2\cos(\tau) - 2\cos(\gamma) + 2\cos(\tau + \gamma).$$

Using the computer, one observes that the curve $p(\tau, \gamma) = 0$ is is convex above $\mathcal{L}$, and that it is tangent to the lines $\tau = \pi/3, \gamma = \pi/3$ and $\mathcal{L}$ (The white curve in Figure 16.) These properties can also be checked using Calculus). Together with the lines given by the general no-overlap constraints on chains of disks ((i)), the curve $p = 0$ bounds two connected, arrow-shaped regions above $\mathcal{L}$ and a (connected) trapezoidal

(yellow) region below where P is defined. To finish proving that m is positive only below $\mathcal{L}$, we use continuity and check that m is negative at one point in each of the arrow-shaped regions above $\mathcal{L}$ and positive at one point in the trapezoidal region below.

Pick the point $(\tau, \gamma) = (\pi/2, \pi/2)$ below $\mathcal{L}$. Then the quadrilateral $ABCD$ is a square and the triangle ADP is equilateral. Consequently $\angle BAP = \angle PDC = \pi/2 + \pi/3$ and $m(\pi/2, \pi/2) = \pi/2 > 0$. Thus indeed $m > 0$ below $\mathcal{L}$. Now pick a point (τ, γ) with $\gamma + \tau > 4\pi/3$, such that $\overline{AD} = 2b$. This point is on the curve $p = 0$, and can thus be on the upper boundary of either arrow-shaped region above $\mathcal{L}$, serving as test case for either region. In this case the pentagon $ABCDP$ is indistinguishable from the quadrilateral $ABCD$ as $P = P'$ is the midpoint of AD. Since the angles of this quadrilateral sum up to 2π, $\angle BAP + \angle PDC + \tau + \gamma = 2\pi$ and, because of ((i)) this implies $\angle BAP + \angle PDC < 2\pi/3$. Thus $m(\tau, \gamma) < 0$ in this case, and by continuity for all the points above $\mathcal{L}$ where it is defined. This finishes to prove that P is defined and does not overlap other points of the chain in exactly the (yellow) trapezoidal region below $\mathcal{L}$. Note that, because of (iii), this implies that P is the only possible offspring in that region.

(v) $\tau + \gamma > 4\pi/3$ *and* $\tau < 2\pi/3 \Leftrightarrow T_0, T_1, R_2$ *and* P *overlap with some point of the chain, and* T_2, R_1 *do not.* (The proof of the statement when $\gamma < \frac{2\pi}{3}$ is identical. This corresponds to the blue regions in the figure).

Assume $\gamma + \tau > \frac{4\pi}{3}, \tau < \frac{2\pi}{3}$. By (iv), we know that P, if it exists, overlaps with either B or C. On the other hand $\tau < \frac{2\pi}{3} \Rightarrow \angle CBT_0 = \tau - \angle T_0BA = \tau - \frac{\pi}{3} < \frac{\pi}{3}$ and thus T_0 overlaps with C. Likewise T_1 overlaps with A. In the rhombus $ABCR_1$ the angle $\angle CBA = \tau < \frac{2\pi}{3}$, and thus the complementary angle $\angle BAR_1 > \pi/3$ and R_1 does not overlap with B. The same reasoning shows that, since $\gamma > \frac{2\pi}{3}, R_2$ overlaps with C when $\gamma < \pi$. When $\gamma \geq \pi$, $R_2 = C$, the ultimate overlap. From (iii) we also know that R_1 and T_2 cannot overlap with D and A respectively. Finally, T_2 can't overlap with B since $\gamma > \frac{2\pi}{3}$.

(vi) $\tau + \gamma > 4\pi/3$ *and* $\tau > 2\pi/3, \gamma > 2\pi/3 \Rightarrow P$ *does not exist and* R_1 *and* R_2 *overlap with some point of the chain, whereas* T_0, T_1, T_2 *do not.*(Red region)
Assume $\tau + \gamma > 4\pi/3, \tau > 2\pi/3$, and $\gamma > 2\pi/3$. It can be visually checked (and proven by calculus) that this region is above the elliptically shaped curve $p = 0$, and thus out of the domain of existence of P.[10] The first inequality insures that T_0 does not overlap with D, nor T_2 with A. The inequality $\tau > 2\pi/3$ shows that T_0 does not overlap with C, and thus does not overlap with any notch point. Likewise $\gamma > 2\pi/3$ implies that T_2 does not overlap with any point in the chain. As we have seen in the previous case, $\tau > 2\pi/3$ implies that R_1 overlaps with B (and coincide with it if $\tau \geq \pi$). Likewise $\gamma > \frac{2\pi}{3}$ implies R_2 overlaps with C (and coincides with it if $\gamma \geq \pi$). Thus these angle conditions leave only T_0, T_1, T_2 with no overlap with points in the chain.

(vii) $\tau + \gamma > 4\pi/3$ *and* $\tau = 2\pi/3 \Rightarrow R_1 = T_0 = T_1$ *and this point does not overlap with any vertex of the chain and neither does* T_2*, but* R_2 *and* P *do. And a similar statement when* $\gamma = 2\pi/3$.
Assume $\tau + \gamma > 4\pi/3$ and $\tau = 2\pi/3$ (vertical boundary between the red and blue region). The first inequality implies that P, if it existed (which it does not on this set), it would overlap with either B or C. the equality $\tau = 2\pi/3$ is equivalent to $R_1 = T_0 = T_1$, as the rhombus $ABCR_1$ has angles $\pi/3$ and $2\pi/3$. In particular this point does not overlap with A, B or C. Since $\gamma > 2\pi/3$, $\angle DCT_1 = \gamma - \pi/3 > \pi/3$ and T_1 does not overlap with D, and thus $T_1 = R_1 = T_0$ does not overlap with any vertex of the chain. Since $\gamma > 2\pi/3$, R_2 overlaps with C (or coincides with it when $\gamma \geq \pi$). The proof of the other statement is obtained by symmetry.

□

B Parameterization of C_3

This appendix completes Section 5. We parameterize C_3 using the inverse of the projection on its tangent plane $\mathcal{T}_0$ at (0,0,0). We will show that this projection is indeed 1-1. $\mathcal{T}_0$ is perpendicular to the gradient

[10] The reader uncomfortable with this argument can note that $\tau + \gamma > 4\pi/3$ implies that, if it existed, P would overlap in that region.

$n := (1,1,1)$ of the function $\sin(\beta_1)+\sin(\beta_2)+\sin(\beta_3)$ at (0,0,0), and thus has equation:

$$\mathcal{T}_0 = \{(\beta_1,\beta_2,\beta_3) \mid \beta_1+\beta_2+\beta_3 = 0\}.$$

We choose the basis for $\mathcal{T}_0$ given by the two vectors $m_1 = (-1,1,0), m_2 = (0,-1,1)$. We can extend this pair to the basis $\{m_1, m_2, n\}$ of $\mathbb{R}^3$, adding the normal vector n. If u,v,w are the coordinates in this basis, the change of coordinates is given by $(\beta_1,\beta_2,\beta_3) = um_1 + vm_2 + wn$, that is:

$$\begin{aligned} \beta_1 &= -u + w \\ \beta_2 &= u - v + w \\ \beta_3 &= v + w \end{aligned} \tag{20}$$

Hence, a parameterization of C_3 is given by finding the function $w(u,v)$ which solves the implicit equation:

$$\sin(w-u)+\sin(u-v+w)+\sin(v+w) = 0, \tag{21}$$

and replacing w by $w(u,v)$ in Equation 20. Note that in the basis $\{m_1,m_2,n\}$, the orthogonal projection on $\mathcal{T}_0$ is given by $um_1+vm_2+wn \mapsto um_1+vm_2$. The map $(u,v)\mapsto(u,v,w(u,v))$ obtained is then by construction an inverse of the orthogonal projection of C_3 onto $\mathcal{T}_0$.

Using trigonometric identities, Equation 21 can be factored as:

$$\cos(w)(\sin(v)-\sin(u)+\sin(u-v))+\sin(w)(\cos(u)+\cos(u-v)+\cos(v)) = 0,$$

from which we obtain (when defined!):

$$w(u,v) = tan^{-1}\left(\frac{\sin(u)-\sin(v)-\sin(u-v)}{\cos(u)+\cos(u-v)+\cos(v)}\right) \tag{22}$$

We now show that the domain of $w(u,v)$ indeed contains the projection of C_3 on $\mathcal{T}_0$. This will finish proving that, in the appropriate domain, the inverse of the projection $(u,v)\mapsto(u,v,w(u,v))$ is a parameterization of C_3 .

To determine the domain of $w(u,v)$, we look for the point in $\mathcal{T}_0$ closest to the origin for which w is not defined, that is, which satisfies $\cos(u)+\cos(u-v)+\cos(v) = 0$, the denominator in its definition (see Equation 22). To this effect, we numerically minimize the Euclidean distance (given, in terms of in terms of (u,v) by $\|um_1+vm_2\| = \sqrt{u^2+(u-v)^2+v^2}$ with the constraint $\cos(u)+cos(u-v)+cos(v) = 0$ and obtain (with Wolfram Alpha, e.g.) an approximate value of 2.92974 at $(u,v) = (\pm 2.39212, 1.19586)$. In other words, the domain of the function $w(u,v)$ contains a Euclidean disk of radius 2.92974 in the plane $\mathcal{T}_0$.

We now show that the hexagon H_3 is within that disk, and by extension, within the domain of w, by computing the distance between the vertices of H_3 and the origin. To find the coordinates of the points corresponding to the vertices, remember that the hexagon is the region of $\mathcal{T}_0$ bounded by the 6 planes given by:

$$\beta_k - \beta_j = 2\pi/3, \;\; k,j \in \{1,2,3\}, k \neq j.$$

Each of these planes is perpendicular to $\mathcal{T}_0$. The vertices are thus given by the solutions of the systems of six linear equations:

$$\begin{aligned} \beta_1+\beta_2+\beta_3 &= 0 \\ \beta_k-\beta_j &= \pm 2\pi/3 \\ \beta_l-\beta_j &= \pm 2\pi/3 \end{aligned}$$

for k,l,j distinct elements of $\{1,2,3\}$, which have solutions

$$\pm\left(-\frac{4\pi}{9},\frac{2\pi}{9},\frac{2\pi}{9}\right), \pm\left(-\frac{2\pi}{9},-\frac{2\pi}{9},\frac{4\pi}{9}\right), \pm\left(\frac{2\pi}{9},-\frac{4\pi}{9},\frac{2\pi}{9}\right) \tag{23}$$

These points are all at distance $(\frac{2}{3})^{(\frac{3}{2})}\pi \approx 1.71007$ of the origin, which is less than 2.92974. Thus the H_3 does not contain any point where w is undefined, and the map

$$(u, v) \mapsto m_1 u + m_2 v + w(u, v)n$$

is well defined on the hexagon and parametrizes C_3. As mentioned above, this map is the inverse of the projection from C_3 to $\mathcal{T}_0$.

C Proof of Proposition 6.2

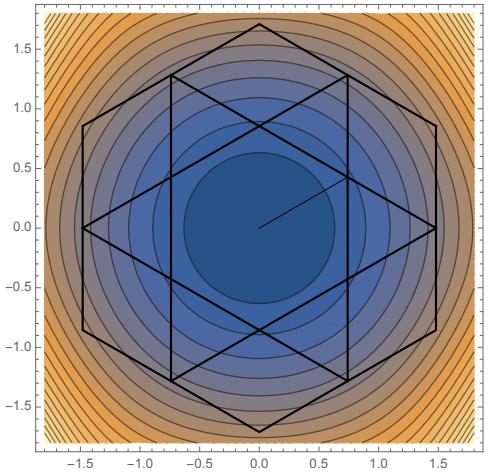

Figure 30: **Contour plot of the distance function on C_3.** The Euclidian distance on C_3 was pulled back under its parametrization, to $\mathcal{T}_0$. The regions bounded by the contours are star shaped around the origin, as evidenced by the figure (each element can be connected to some center point by a line segment), which implies that distance grows along any ray from the origin. This in turns implies that the vertices of the (also star shaped) triangles and hexagon achieve the maximum distance from the origin for their respective regions.

Proof. The points corresponding to the vertices of the hexagon can be computed numerically using Equations 20 and 22. But they also can be found exactly by observing that one of the angles β_k is increasing (in absolute value) along the axes through the vertices: they are the projections of the 3D axes to $\mathcal{T}_0$. The vertices must then be at the maximum (or minimum) possible value of that angle in C_3, namely $\pm\pi/2$, Looking at the vertex in the kite, we see that it corresponds to $\beta_1 = -\pi/2$ since the vertex is on the projection of the negative β_1 axis. This vertex also satisfies $\beta_2 - \beta_1 = 2\pi/3 = \beta_3 - \beta_1$ from which we obtain the coordinates $(-\pi/2, \pi/6, \pi/6)$ of the vertex. One can indeed check that this satisfies the two equations above, as well as $\sum_{k=1}^{3} \sin(\beta_k) = 0$. By symmetry, the vertices of C_3 have coordinates

$$\pm(-\pi/2, \pi/6, \pi/6), \pm(\pi/6, -\pi/2, \pi/6), \pm(\pi/6, \pi/6, \pi/2).$$

All these points are at distance $\sqrt{11}\pi/6 \approx 1.73658$ of the origin. The corresponding value of b, obtained from $b\sum_{k=1}^{3} \cos(\beta_k) = 1$ is $b = 1/(2\cos(\pi/6)) = 1/\sqrt{3}$.

As seen on Figure 21, the vertex of the lighter triangle of the star of David in the positive quadrant is given as the intersection of the three planes of equations $\beta_3 = 0, \beta_3 - \beta_1 = 2\pi/3$ and $\beta_3 - \beta_2 = \pi/3$. This easily solved system of equations yields $(\beta_1, \beta_2, \beta_3) = (-\pi/3, 0, \pi/3)$. By symmetry the 2 other points are $(\pi/3, -\pi/3, 0), (0, \pi/3, -\pi/3)$. The vertices of the darker triangle are obtained by reflecting about the $\beta_3 = \beta_2$ plane, *i.e.* by transposing the last two coordinates, which yields $(-\pi/3, \pi/3, 0), (\pi/3, 0, -\pi/3), (0, -\pi/3, \pi/3)$ as advertised. The angles at each of these six points satisfy $\sum_{k=1}^{3} \sin(\beta_k) = 0$ so they belong to C_3. These points all are at distance $\sqrt{2}\pi/3 \approx 1.48096$ from the origin. The corresponding disk diameter is $b = 1/(\cos(0) + 2\cos(\pi/3)) = 1/2$.

As for the vertices of the inner hexagon, intersection of the two triangles of the star of David, its representative in the kite is at the intersection of the planes $\beta_3 - \beta_1 = \pi/3, \beta_2 - \beta_1 = \pi/3$. Since $\beta_2 = \beta_3$, the chain has the a triangular shape, with sides of length $1, b$ and $2b$. The notch angle of this chain is $\pi + \beta_1 - \beta_2 = 2\pi/3$ and the Law of Cosines gives $1 = b^2(5 - 4\cos(2\pi/3))$ which yields $b = 1/\sqrt{7}$. The Law of Cosine can then be applied to compute β_1, which (in absolute value) is an inner angle of the same triangle: $4b^2 = b^2 + 1 - 2b\cos(\beta_1)$ which gives $\beta_1 = -\arccos\left((1-3b^2)/2b\right) = -\arccos(2/\sqrt{7}) \approx -0.713724$. From this we get $\beta_2 = \beta_3 = -\arccos(2/\sqrt{7}) + \pi/3 \approx 0.33347$. So the inner hexagon vertices can be numerically given approximately as $\pm(-0.7137, 0.333547, 0.33347)$ and the permutations $\pm(0.33347, -0.71372, 0.33347), \pm(0.33347, 0.33347, -0.71372)$. The distance from the origin for all these points is $\sqrt{(\pi/3 - \arccos(2/\sqrt{7}))^2 + \arccos(2/\sqrt{7})^2} \approx 0.85546$

The visual proof that the vertices of the triangles and hexagons achieve the maximum distance in those regions is contained in Figure 30. To show that the value of b is maximized at the vertices of these respective regions, it is enough to show that b increases along rays from the origin in $\mathcal{T}_0$. As the value b is computed from Equation 4, $b\sum_{k=1}^{3}\cos(\beta_k) = 1$, we show that the sum of cosine decreases along rays. The directional derivative $-\beta_1\sin(\beta_1) - \beta_1\sin(\beta_1) - \beta_1\sin(\beta_1)$ of this sum along the radius is always negative since β_k and $\sin(\beta_k)$ have same sign for $\beta_k \in (-\pi/2, \pi/2)$. Thus $\sum_{k=1}^{3}\cos(\beta_k)$ decreases as the point $(\beta_1, \beta_2, \beta_3)$ moves away from the origin, and b must increase. Since we have proven that the points of C_3 corresponding to the vertices of the triangles and hexagons are the farthest away from the origin in their respective region, they must achieve the maxima of b for these regions. Equation 4, $b\sum_{k=1}^{3}\cos(\beta_k) = 1$, □

D Computation of the map $(\tau', \gamma') = \phi(\tau, \gamma)$

Proposition D.1. *The map $\phi(\tau, \gamma)$ defined in Proposition 7.5 is given by:*

$$\begin{aligned} \tau' &= 2\tan^{-1}\left(\frac{v + \sqrt{u^2 + v^2 - w^2}}{u + w}\right) + \pi/3, \\ \gamma' &= \cos^{-1}(c), \end{aligned} \tag{24}$$

where the functions c, u, v and w of (τ, γ) are given by:

$$\begin{aligned} c &= \cos(\tau) - \cos(\gamma - \pi/3) + \cos(\tau + \gamma - \pi/3) - 1/2 \\ u &= 2 - 2c, \quad v = 2\sqrt{1 - c^2}, \quad w = 1 + 2\cos(\tau) - 2c. \end{aligned}$$

We refer to Figure 25. To compute $\tau'(\tau, \gamma), \gamma'(\tau, \gamma)$, we need the following generalization of the law of cosines to quadrilaterals:

Lemma D.2. *Given a 3-chain ABCD with hinge angles α, and β, and edges of equal length b we have:*

$$\overline{AD}^2 = b^2(3 - 2\cos(\alpha) - 2\cos(\beta) + 2\cos(\alpha + \beta)) \tag{25}$$

Proof. Assuming $b = 1$ and rotating the chain so that $B = (0, 0), C = (1, 0)$, we obtain $A = (\cos(\alpha), \sin(\alpha)), D = (1 + \cos(\pi - \beta), \sin(\pi - \beta)) = (1 - \cos(\beta), \sin(\beta))$ and thus

$$AD^2 = (1 - \cos(\beta) - \cos(\beta))^2 + (\sin(\beta) - \sin(\alpha))^2 = 3 - 2\cos(\alpha) - 2\cos(\beta) + 2\cos(\alpha + \beta),$$

where the last equation is given by trigonometric identities. Clearly this formula rescales with the square of the edge length. □

Assume now that $ABCJDPA$ is a chain of disks and the angles $\tau, \gamma, \tau', \gamma'$ are as in Figure 25b. Evaluating AD^2 by using the law of cosines on the triangle $\triangle APD$, as well as the previous lemma applied to the chain ABCD, we obtain:

$$b^2(2-2\cos(\gamma')) = \overline{AD}^2 = b^2(3-2\cos(\tau)-2\cos(\gamma-\pi/3)+2\cos(\tau+\gamma-\pi/3))$$

from which we extract

$$\gamma' = \cos^{-1}\Big(\cos(\tau)-\cos(\gamma-\pi/3)+\cos(\tau+\gamma-\pi/3)-1/2\Big).$$

We repeat the same process, using triangle $\triangle ABC$ and the 3-chain APDC this time, introducing the angle $\lambda = \angle CDP = \tau' - \pi/3$ and obtain:

$$\begin{aligned} AC^2 &= b^2(2-2\cos(\tau)) = b^2(3-2\cos(\gamma')-2\cos(\lambda)+2\cos(\gamma'+\lambda)) \\ &= b^2(3-2\cos(\gamma')-2\cos(\lambda)+2\cos(\lambda)\cos(\gamma')-2\sin(\lambda)\sin(\gamma')). \end{aligned}$$

This is of the form

$$u\cos(\lambda)+v\sin(\lambda) = w, \tag{26}$$

where

$$u = 2-2\cos(\gamma'),\ v = 2\sqrt{1-\cos^2(\gamma')},\ w = 1+2\cos(\tau)-2\cos(\gamma')$$

We use the formulas involving the tangent of the $1/2$ angle: $\cos(x) = \frac{1-\tan^2(x/2)}{1+\tan^2(x/2)}$, $\sin(x) = \frac{2\tan^2(x/2)}{1+\tan^2(x/2)}$ which transforms Equation 26 into a quadratic equation in $t = \tan(\lambda/2)$:

$$u(1-t^2)+2vt = w(1+t^2).$$

We solve for t, and plug the solution in $\tau' = \lambda + \pi/3 = 2\tan^{-1}(t)+\pi/3$, yielding:

$$\tau' = 2\tan^{-1}\left(\frac{v+\sqrt{u^2+v^2-w^2}}{u+w}\right)+\pi/3,$$

the other solution making no sense in our setting.

References

[1] Mughal A. and Weaire D. Phyllotaxis, disk packing and fibonacci numbers. *arXiv preprint arXiv:1608.05824*, 2016.

[2] Turing A. The chemical basis of morphogenesis. *Philosophical Transactions of the Royal Society of London B: Biological Sciences*, 237(641):37–72, 1952.

[3] Irving Adler. A model of contact pressure in phyllotaxis. *Journal of theoretical Biology*, 45(1):1–79, 1974.

[4] Nisoli C., Gabor N., Lammert P., Maynard J.D, and Crespi V. Static and dynamical phyllotaxis in a magnetic cactus. *Phys. Rev. Lett.*, 102, 2009.

[5] Beller D. and Nelson D. Plastic deformation of tubular crystals by dislocation glide. *Phys. Rev. E*, 94, 2016.

[6] Reinhardt D., Pesce E., Stieger P., Mandel T., Baltensperger K., Bennett M., Traas J., Friml J., and Kuhlemeier C. Regulation of phyllotaxis by polar auxin transport. *Nature*, 426(6964):255–260, 2003.

[7] de Reuille P. B., Bohn-Courseau I., Ljung K., Morin H., Carraro N., Godin C., and Traas J. Computer simulations reveal properties of the cell-cell signaling network at the shoot apex in arabidopsis. *Proc. Natl. Acad. Sci. U.S.A.*,, 103 (5):1627–1632., 2006.

[8] Freeman E. Cylinder lattice applet (geogebra site). https://ggbm.at/NeHVks33.

[9] R. Erickson. Tubular packing of spheres in biological fine structure. *Science*, 181:705–716, 1973.

[10] Bergeron F. and Reutenauer C. Golden ratio and phyllotaxis, a clear mathematical link. *J Math Biol.*, 2018.

[11] Van Iterson G. Mathematische und microscopisch-anatamische studien uber blattstellungen, nebst betraschungen uber der schalenbau der miliolinen gustav-fischer-verlag. *G. Fischer: Jena*, 1907. available online through google books.

[12] Dumais J. Golé C. and Douady S. Fibonacci or Quasi-Symmetric Phyllotaxis, Part I : why? *Acta societatis botanicorum Poloniae*, 85(4), 2016.

[13] Airy H. On leaf-arrangement. *Proceedings of the Royal Society of London*, 21, 1872.

[14] Jönsson H., Heisler M. G, Shapiro B., Meyerowitz E., and Mjolsness E. An auxin-driven polarized transport model for phyllotaxis. *Proceedings of the National Academy of Sciences*, 103(5):1633–1638, 2006.

[15] Meinhardt H., Koch A., and Bernasconi G. Models of pattern formation applied to plant development. In *Symmetry in plants*, pages 723–758. Singapore: World Scientific, 1998.

[16] Bravais L. and Bravais A. Essai sur la disposition des feuilles curvisériées. *Ann. Sci. Nat.*, 7:42–110, 1837.

[17] Leonid S Levitov. Phyllotaxis of flux lattices in layered superconductors. *Phys. Rev. Lett.*, 66(2):224–227, 1991.

[18] Kunz M. *Thèse*. PhD thesis, Université de Lausanne, Switzerland, 1997.

[19] Pennybacker M., Shipman P., and Newell A. Phyllotaxis: Some progress, but a story far from over. *Physica D: Nonlinear Phenomena*, 306:48–81, 2015.

[20] Rueda-Contreras MD. and Aragón JL. Alan turing's chemical theory of phyllotaxis. *Rev. Mex. Fis. E*, 60(1):1–12, 2014.

[21] A. Mughal, H. K. Chan, and D. Weaire. Phyllotactic description of hard sphere packing in cylindrical channels. *Phys. Rev. Lett.*, 106:115704, Mar 2011.

[22] Atela P. and Golé C. Rhombic tilings and primordia fronts of phyllotaxis (prepgolerint), 2007. http://arxiv.org/abs/1701.01361.

[23] Atela P., Golé C., and Hotton S. A dynamical system for plant pattern formation: Rigorous analysis. *J. Nonlinear Sci.*, 12:641–676, 2002.

[24] Harris P.J.F. *Carbon Nanotube Science: Synthesis, Properties and Applications*. Cambridge University Press, 2009.

[25] Smith R., Guyomarc'h S., Mandel T., D. Reinhardt, Kuhlemeier C., and Prusinkiewicz P. A plausible model of phyllotaxis. *Proceedings of the National Academy of Sciences*, 103(5):1301–1306, 2006.

[26] Y. Refahi, G. Brunoud, E. Farcot, A. Jean-Marie, M. Pulkkinen, T. Vernoux, and C. Godin. A stochastic multicellular model identifies biological watermarks from disorders in self-organized patterns of phyllotaxis. *eLife*, 5, 2016.

[27] Douady S. The selection of phyllotactic patterns. In Jean R. and Barabé D., editors, *Symmetry in Plants*, pages 281–312. World Scientific, Singapore, 1998. doi:10.1142/9789814261074-0014.

[28] Douady S. and Golé C. Fibonacci or Quasi-Symmetric Phyllotaxis, Part II : Botanical Observations. *Acta societatis botanicorum Poloniae*, 85(4), 2016.

[29] Douady S. and Couder Y. Phyllotaxis as a dynamical self organizing process, part 1. *J. Theor. Biol.*, 178:255–274, 1996.

[30] Douady S. and Couder Y. Phyllotaxis as a dynamical self organizing process, part 2. *J. Theor. Biol.*, 178:275–294, 1996.

[31] Douady S. and Couder Y. Phyllotaxis as a dynamical self organizing process, part 3. *J. Theor. Biol.*, 178:295–312, 1996.

[32] Hotton S., Johnson V., Wilbarger J., Zwieniecki K., Atela P., Golé C., and Dumais J. The possible and the actual in phyllotaxis: Bridging the gap between empirical observations and iterative models. *Journal of Plant Growth Regulation*, 25(4):313–323, 2006.

[33] Schwendener S. *Mechanische Theorie der Blattstellungen*. W. Engelmann, Leipzig, 1878.

[34] Hofmeister W. Allgemeine morphologie der gewashe. In *Handbuch der Physiologischen Botanik*, pages 405–664. Engelmann, 1868.

[35] Wikipedia. Circle packing, 2018.

[36] Wikipedia. Polygonal chains, 2018.

[37] Douady S. & Couder Y. Phyllotaxis as a physical self-organized growth process. *Phys. Rev. Lett.*, 68:2098–2101, 1992.

[38] Guédon Y., Refahi Y., Besnard F., Godin C., and T. Vernoux. Pattern identification and characterization reveal permutations of organs as a key genetically controlled property of post-meristematic phyllotaxis. *J Theor. Biol.*, 338:94–110, 2013.